Structural and magnetic properties of YIG thin films and interfacial origin of magnetisation suppression

Arpita Mitra

University of Leeds

School of Physics and Astronomy

Submitted in accordance with the requirements for the degree of

Doctor of Philosophy

August 2017

This thesis is dedicated to my parents and my sister.

Intellectual Property Statement

The candidate confirms that the work submitted is her own and that appropriate credit has been given where reference has been made to the work of others.

This research work has contributed to following three publications:

1. Interfacial Origin of the Magnetization Suppression of Thin film Yttrium Iron Garnet. **A. Mitra**, O. Cespedes, Q. Ramasse, M. Ali, S.Marmion, M. Ward, R. M. D. Brydson, C. Kinane, J. F. K. Cooper, S. Langridge and B. J. Hickey. Scientific Reports 7, Article number: 11774 (2017).

2. Thickness dependence study of current-driven ferromagnetic resonance in $Y_3Fe_5O_{12}$/heavy metal bilayers. Z. Fang, **A. Mitra**, A. L. Westerman, M. Ali, C. Ciccarelli, O. Cespedes, B. J. Hickey and A. J. Ferguson. Appl. Phys. Lett. 110, 092403 (2017).

3. Magnetic properties of spin waves in thin Yttrium iron garnet films. A. Talalaevskij, M. Decker, J. Stigloher, **A. Mitra**, H. S Korner, O. Cespedes, C.H. Back and B. J. Hickey. Phys. Rev. B 95, 064409 (2017).

1. Work attributable to the candidate: Grew the samples and performed the XRR, XRD, AFM, VSM, SQUID magnetometry and PNR experiments, and data analysis leading to Table 1 and figures 1, 2, 4 and 5. Work attributable to others: O.C. devised the PNR experiment and techniques used for squid magnetometry, Q.R. performed the analytical STEM experiments and data analysis. M.A. contributed to the finding of additional layer between YIG and GGG through x-ray reflectivity, S.M. grew samples and with M.W. did the initial TEM sample preparation, R.B, B.H. and S.M. wrote the case for SuperSTEM beamtime. Candidate did the PNR with the aid of M.A., C.K. and S.L. J.C. and S.L. directed the PNR data analysis. B.H. designed the original study and did the fitting of M(T) data. All authors contributed in writing the manuscript.

2. Work attributable to the candidate: Candidate grew all the first batch of samples of YIG/Pt and YIG/Ta; performed structural and magnetic characterisations. Candidate performed CI-FMR experiments with Z. Fang and contributed to data analysis. Candidate contributed to magnetic characterisation to the second batch of samples.

3. Work attributable to the candidate: Sample growth and structural and magnetic characterisations.

Acknowledgements

Firstly, I would like to thank my supervisors, Prof B J Hickey and Dr Oscar Cespedes for their support and guidance. I am especially thankful to Dr Oscar Cespedes for his continuous advice and motivation. I am grateful to EU FP7 for awarding me Marie Curie fellowship to pursue my doctoral research work.

I would like to thank Prof Christian Back for giving me the opportunity to perform FMR experiments in collaboration with Markus Hartienger in University of Regensburg. I must thank Prof Eduardo Alves for giving me training in RBS technique and for his help during my experiment in his lab. I would like to thank Dr Satoshi Sugimoto, Craig Knox and Georgios Stefanou for their help in cutting my substrates. I would like to express my appreciation to the cryogenic technicians of our group: John Turton, the late Philip Cale, Brian and Luck Bone. I am grateful to all the members of the Condensed Matter Group for their help and cooperation during my PhD.

Finally, I am eternally thankful to my parents and my sister Sunanda, for their love, support and encouragement at every stages which has made this work possible.

Abstract

This work covers the complete study of the properties of high quality nm-thick sputtered Yttrium iron garnet ($Y_3Fe_5O_{12}$) films, with the discovery of interfacial diffusion and its effect on the magnetisation suppression. Here we report the structural and magnetic properties of YIG nano films deposited on Gadolinium gallium garnet (GGG) substrate by RF magnetron sputtering. The structural characterisation and morphology of the films were analysed using X-ray reflectivity (XRR), X-ray diffraction (XRD) and atomic force microscopy (AFM). The magnetic properties were investigated using VSM and SQUID magnetometer. The films in the 10 - 60 nm thickness range have surface roughness of 1-3 Å, and (111) crystalline orientation. The saturation magnetisation, coercive field and the Curie temperature observed in our YIG films are 144 $\pm$ 6 emu/cc, 0.30 $\pm$ 0.05 Oe and 559 K, respectively. The thickness dependence of the saturation magnetic moment shows the existence of a 6 nm dead layer. The temperature dependence of the magnetization M(T) in YIG reveals a reduction in magnetization at low temperature, below $\sim$ 100 K. Through an extensive analysis using STEM, we discovered an interdiffusion zone of 4 - 6 nm at the YIG/GGG interface where Gd from the GGG and Y from the YIG diffuse. Analysis of XRR data also confirms the presence of Gd-rich diffused layer of 5 - 6 nm thick at the interface. This Gd-rich YIG layer having compensation temperature at 100 K corresponds to 40% Gd-diffusion, that aligns antiparallel to the net moment of YIG, resulting in the magnetisation suppression in YIG at low temperature. Our polarised neutron reflectivity results also revealed the magnetization downturn in 80 nm YIG film. FMR results showed narrow FMR linewidth and a small Gilbert damping, for e.g. (2.6 $\pm$ 0.3) x 10^{-4} in 38 nm thick YIG. The temperature dependence of the Gilbert damping factor in YIG and YIG/Pt showed a linewidth broadening and increased damping below 50 K. Our current induced FMR results demonstrate the dominating role of Oersted

field torque in driving the magnetization dynamics in YIG/Pt bilayer films. Our investigation on the effect of C_{60} molecules on the damping of YIG in YIG/C_{60} hybrid structures shows an increase in damping in thin YIG films, but it decreases between 80 - 160 nm. Our findings widen the applications of sputtered nm-thick epitaxial YIG films and YIG-based multilayers in magnonics, spin caloritronics and insulator-based spintronics devices.

CONTENTS

Abbreviations

YIG	Yttrium Iron Garnet	GGG	Gadolinium Gallium Garnet
YAG	Yttrium Aluminium Garnet	NM	Normal Metal
AC	Alternating Current	CI-FMR	Current Induced Ferromagnetic Resonance
AFM	Atomic Force Microscopy	STT	Spin Transfer Torque
DC	Direct Current	FET	Field Effect Transistor
FWHM	Full Width Half Maximum	UHV	Ultra High Vacuum
SHE	Spin Hall Effect	ISHE	Inverse Spin Hall Effect
FM	Ferromagnet	RF	Radio Frequency
PNR	Polarised Neutron Reflectivity	STEM	Scanning Transmission Electron Microscopy
XRR	X-ray Reflectivity	XRD	X-ray Diffraction
RF	Radio Frequency	SLD	Scattering Length Density
VSM	Vibrating Sample Magnetometer	SQUID	Superconducting Quantum Interference Device
CPW	Coplanar Waveguide	HM	Heavy Metal
VNA	Vector Network Analyser	FMR	Ferromagnetic Resonance
SA	Spin Asymmetry	RMS	Root-mean-square
DUT	Device Under Test	RBS	Rutherford Backscattering
EELS	Electron Energy Loss Spectroscopy	HAADF	High Angle Annular Dark Field

CHAPTER 1

Introduction

Spintronics, or spin-electronics, aims for the generation and manipulation of spin currents for spintronics applications. The main goal of spintronics is to study the interaction between electron spin and solid state environments, and to incorporate this knowledge for developing next generation memory devices. It has led to incredible advances in data storage, non-volatility, low power dissipation, increased data processing rate and high performance. This experimental research work will contribute to the contemporary research interest in the field of spintronics.

In a pioneering work, Mott provided a foundation for the understanding of spin polarised transport and sought an explanation of the unusual behaviour of the electrical resistance in ferromagnetic metals, which forms the basis of magnetoresistive effects [1, 2]. A new physical phenomenon called giant magnetoresistance (GMR) was discovered in the late 1980s, by Albert Fert [3] and Peter Grunberg [4] in epitaxial Fe|Cr multilayers, and later this effect was realised in other multilayer structures, that can be used for non-volatile memory applications [5, 6]. In 1994, the first magnetic sensor using GMR was released [7] and later IBM produced the first GMR read heads in magnetic hard disks [8]. In 21st century, GMR was replaced by tunnel magnetoresistance (TMR) [9, 10] and then, Magnetic tunnel junctions (MTJ) formed the base element of many magnetic random-access memory (MRAM) devices. To get high TMR (200%), epitaxial MTJs consist of crystalline MgO tunnel barrier. In 1996, Slonczewski and Berger independently proposed an effect called spin transfer torque, in which a spin-polarized current can transfer angular momentum to a ferromagnet and manipulate its magnetization direction, without any applied magnetic field [11, 12]. Development of non-volatile MRAM for magnetic hard risks made a revolution in spintronics [13, 14]. Other promising developments for further scaling of MRAM are the spin transfer torque based magnetization switching [11, 12, 15] and the magnetic domain wall racetrack memory [16]. In 1990, Datta and Das [17] proposed an electron spin based field effect transistor (spin-FET) where the electric field at the gate electrode controls the precession of spins. In this Datta-Das SFET, the source and drain are the ferromagnets which act as the injector and detector of electron spins. The spin-FET

has been realized experimentally [18, 19]; but its operation at ambient conditions has yet to be demonstrated. This field offers promising advantages such as, it can be used for fast programmable logic devices and can eliminate the time delay for the data processing. It has the potential to replace electron charge based conventional electronics devices in future.

Despite the numerous advantages with conventional spintronics, it relies on the transfer of electrons for the information transfer and processing. The recent emerging field of magnon spintronics provides us another route, as it is based on the information transfer and processing by spin waves [20–24]. Magnons are the quanta of spin waves, defined as the collective excitations of magnetic moments in magnetically ordered materials. Magnons can propagate over centimeters distances [21]. As spin current carries information in the form of spin angular momentum, this results in information transport without the flow of charge current, and thus free from Joule heating dissipation. The classical method of magnon excitation is microwave technique which has still retained its importance for controlling the frequency, wavelength and phase of the injected magnons. Other methods of excitation are: femtosecond laser techniques where an ultra-short laser pulse can excite the magnetic system [25]; parametric amplification of spin waves from thermal fluctuations [26] and spin-transfer-torque (STT)-based magnon injection [27–29]. The use of magnons gives us the scope to develop unique wave-based computing technologies. Further, magnon properties can be engineered on a wide scale by proper selection of magnetic material and the geometry of magnetic structures. It allows us to utilize magnetic insulator for making low energy consumption devices. For the realization of insulator-based devices, it is necessary to create efficient converters which can transform pure spin currents into charge currents and vice versa. In ferromagnetic insulator/metal bilayers, the spin current transfer can be realized due to exchange interaction between insulator electrons and conduction electrons spins at the interface. The spin pumping effect describes the generation and transfer of spin-polarized current from the ferromagnetic layer to the attached normal metal layer [30, 31]. This spin current can be converted into a charge current in the

normal metal by the inverse spin Hall effect (ISHE) [32, 33]. In these heterostructures, a direct current in the paramagnetic layer can be converted into spin current by the spin Hall effect (SHE) [32, 34], which in turn can excite the magnetization dynamics in the ferromagnetic layer by the spin transfer torque (STT) and hence generates spin waves. In 2010, Kajiwara *et al.* first demonstrated this full cycle of conversion process, i.e, from a charge current in the normal metal into a pure spin current and back to a charge current, in the magnetic insulator/normal metal (YIG/Pt) bilayer structure [35]. In 2010, Slonczewski proposed an idea of generating spin transfer torque by thermal transport of magnons [36]. Since then, there was a rapidly increasing interests in the investigation of various aspects of magnetization dynamics in YIG/Pt bilayer structures by spin pumping and spin transfer torque.

In recent years, the discovery of the spin Seebeck effect (SSE) establishes another field of research known as Spin caloritronics, which focus on the investigation of the interplay between heat and spin currents. In 2008, the SSE was first discovered by Uchida $et\ al.$ in a ferromagnetic metal $Ni_{81}Fe_{19}$ film [37] by means of the spin-detection technique inverse spin Hall Effect (ISHE) in a Pt film. The spin Seebeck effect is the generation of spin voltage due to the movement of electron spins as a result of temperature gradient in magnetic materials. This lead to the first interpretation that the SSE is caused by the movement of conduction electrons based on the chemical potential of differently orientated spins. Later in 2010, the same group observed SSE in magnetic insulators such as $Y_3Fe_5O_{12}$ and $LaY_2Fe_5O_{12}$ (La: YIG) [38]. This field is of great interest for its applications in thermoelectric generation which can lead to energy saving technologies in future.

Recent research in spintronics has focused on ferrimagnetic insulators Yttrium iron garnet (YIG) to develop efficient insulator-based magnetic devices using pure spin currents. The attractive properties of YIG are ultra low damping ($\alpha \approx 3$ x 10^{-5}) [39], high Curie temperature, high chemical stability [40], electrically insulating behaviour [41] (band gap = 2.85 eV) and easy synthesis of single crystalline material. As YIG is an insulator, it is free from parasitic heating effects due to conduction electrons. In the

past for several decades, YIG is one of the most thoroughly studied magnetic materials due to its wide applications in microwave devices such as microwave filters, delay lines and magneto-optical devices such as optical insulators, displays and deflectors. In recent years, YIG has played a central role in the emerging fields of spin pumping, spin transfer torque, spin hall magnetoresistance and thermally driven spin caloritronics [42–49]. In reference [50], the operation of a spin torque transistor consisting of two lateral thin-film spin valves coupled by a magnetic insulator (YIG) via the spin transfer torque have been studied theoretically.

The recent development of magnonics and oxide spintronics creates a demand for *nanometre* thick YIG films with high crystalline quality that continue to exhibit extremely low Gilbert damping. Traditionally, YIG has been grown by several techniques with Liquid Phase Epitaxy (LPE) [51–53] being the most successful at obtaining the highest quality, but in rather thick films ($\sim$ microns). There are several reports on the deposition of nm-thick YIG films by pulsed laser deposition (PLD) [54–59] and its advanced version of laser molecular beam epitaxy [60, 61]. However, the best results for PLD samples seems to be from Hauser *et al.* where the damping as low as 7 x 10^{-5} for a 20 nm film has been reported [62]. RF sputtering followed by either in situ annealing [49, 63] or post-growth annealing [64–66] has attracted considerable interest. On the other hand, off-axis sputtering [47, 65] has been reported to produce highly crystalline material with reasonable magnetic properties measured at room temperature.

Within the framework of this thesis work, we carried out the detailed investigation of the structural, magnetic and FMR properties of nanometer thick RF sputtered YIG films for a better understanding of its characteristics and future optimisation. We particularly discovered the effect of interfacial diffusion on the *magnetization suppression* in ultra low damping YIG films.

In Chapter 2 we present the relevant theoretical background to understand the experimental work and the results presented. At first we describe the crystal structure of the YIG with the arrangement of atoms in the unit cell and its ferrimagnetic order. The fundamental equation of the magnetization dynamics and the derivation of Landau-

Lifshitz-Gilbert equation are discussed. Subsequently, we present the basic principles of the spin pumping phenomenon and current induced torque in ferromagnetic/non-magnetic heterostructures. Finally, the mechanism of the spin Hall effect and the inverse spin Hall effect is discussed.

Chapter 3 is devoted to the experimental techniques and the experimental set up used within the framework of this work, which includes sample deposition, structural and magnetic characterisation and the ferromagnetic resonance techniques. In the first part of this chapter, the deposition of YIG samples by RF magnetron sputtering is discussed, followed by annealing conditions to obtain a (111) single crystal YIG with surface roughness of 1-3 Å. The process of deposition of Pt by DC sputtering and thermal sublimation of C_{60} are presented. X-ray reflectivity and x-ray diffraction are used to investigate the structural properties and crystallinity of YIG samples. Morphology of the films are analysed using atomic force microsopy (AFM). We performed atomic scale investigation of YIG/GGG interface using scanning transmission electron microscopy (STEM). We used Rutherford backscattering (RBS) technique to study the compositional analysis of YIG films. The magnetic properties are studied using vibrating sample magnetometer (VSM) and superconducting quantum interference device (SQUID) VSM. Synchrotron radiation techniques, polarised neutron reflectivity (PNR) contributed significantly to extract the magnetic information at the sample substrate interface. At the end, we discussed the FMR technique through which we investigated the ferromagnetic resonance properties of YIG and its bilayer structures.

In the result sections, we present a systematic study of high quality nm-thick YIG films grown by on-axis sputtering using structural and magnetic characterisation. We investigated the interfacial origin of magnetisation reduction in YIG films. These results are outlined in two chapters: chapter 4 presents the structural properties of YIG, which reveals an interdiffusion at the YIG/GGG interface, and chapter 5 is focused on the magnetic properties, that includes deep insight of magnetic information at the interface which has been lacking despite of its extensive use. An unexpected decrease in magnetization in thin YIG films below $\sim$ 100 K was first discovered from our SQUID

magnetometry results.

The potential of our RF sputtered YIG films for spin pumping and STT has been investigated using FMR technique and is presented in chapter 6. Our nm-thick YIG films exhibit a very low Gilbert damping. The damping parameter α reveals thickness dependence ($\alpha \propto 1$/Thickness). The temperature dependence of Gilbert damping parameter has been detected in YIG and YIG/Pt bilayer structures. Current induced FMR measurement in collaboration with University of Cambridge, confirms the dominating role of Oersted field torque in driving the magnetization dynamics in YIG/Pt bilayers. Finally, we investigated the influence of C_{60} molecules on the magnetization dynamics of YIG/C_{60} hybrid structures. This work shows promising research area for future investigation.

In Chapter 7 the experimental results of this research work are summarized and a perspective on future investigations and applications is given.

CHAPTER 2

Theoretical background

2.1 Introduction

This chapter is devoted to the theoretical background of the magnetization dynamics and interface effects that are the foundation of this thesis. In the first part of this chapter, the crystal structure and magnetic properties of Yittrium iron garnet are described. Then the fundamental principles of the magnetization dynamics and the Landau-Lifshitz-Gilbert equation governing the precessional motion of the magnetization in the presence of a magnetic field are introduced. The basic principles of the ferromagnetic resonance, spin-pumping effect and current induced spin transfer torque is discussed in the following section. Last section of this chapter is dedicated to the detection technique of spin currents, spin Hall effect and inverse spin Hall effects.

2.2 Crystal structure and magnetic properties of YIG

Yttrium iron garnet YIG ($Y_3Fe_5O_{12}$) is a ferrimagnetic insulator, discovered by Bertaut and Forrat in 1956 [67, 68] and was referred to as the fruitfly of magnetism by Kittel about 50 years ago [69]. Yttrium iron garnet has a complex crystal structure with nearly cubic symmetry and definite composition. The density of YIG is 5.17 g/cm^3 [70]. It has an extremely small magnetization damping, $\alpha \approx 3 \times 10^{-5}$ [71]. It has a large band gap of 2.85 eV [70] and high Curie temperature of about 560 K.

The unit cell of YIG has a lattice constant of 12.376 $\pm$ 0.004 Å. The most probable space group for yttrium iron garnet is $O_h{}^{10}$-$Ia3d$ [68]. The unit cell of YIG has cubic structure containing eight chemical formula units of $Y_3Fe_5O_{12}$ with 160 ions in total (Figure 2.1). In each formula unit of YIG, there are three dodecahedral (*c* site), two octahedral (*a* site) and three tetrahedral sites (*d* site) containing 24 Y^{3+}, 40 Fe^{3+} ions and 96 O^{2-} ions. The Y^{3+} ions occupy the dodecahedral sites (*c* sites), each site being surrounded by eight O^{2-} ions that form an eight-cornered twelve-sided polyhedron. 24 Fe^{3+} occupy tetrahedral sites (*d* sites) and are surrounded by four O^{2-} ions forming tetrahedral symmetry. The 16 Fe^{3+} occupy the octahedral sites (*a* sites) and are

surrounded by six O^{2-} ions forming octahedral symmetry. The O^{2-} ions sit on *h* sites, each being at a point where the corners of one octahedron, one tetrahedron, and two polyhedrons meet. Thus, each O^{2-} ion is surrounded by one *d* site Fe^{3+} ion, one *a* site Fe^{3+} ion and two *c* site Y^{3+} ions.

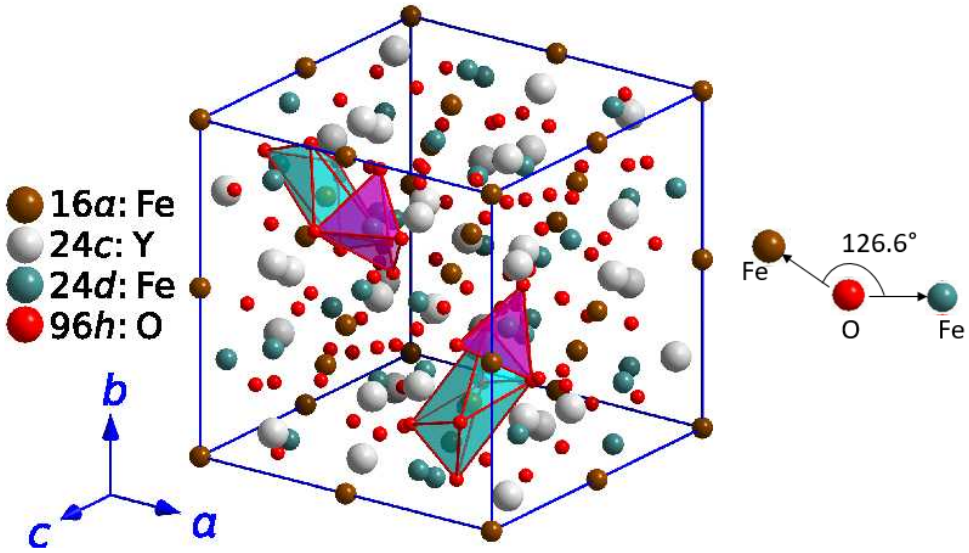

Figure 2.1: *Crystal structure of Yttrium iron garnet ($Y_3Fe_5O_{12}$) [72]. The unit cell of YIG has cubic structure containing eight chemical formula units of $Y_3Fe_5O_{12}$ with 160 ions in total. The Y^{3+} ions occupy dodecahedral sites (c sites), Fe^{3+} occupy tetrahedral sites (d sites) and 16 Fe^{3+} occupy the octahedral sites (a sites). The magnetisation in YIG originates from the super-exchange interactions between 16 Fe^{3+} ions on a sites and 24 Fe^{3+} ions on d sites.*

The Y^{3+} ions have a closed shell electronic configuration ($[Kr]4d^05s^0$) and hence are diamagnetic. The magnetisation in YIG originates from the super-exchange interactions between 16 Fe^{3+} ions on *a* sites and 24 Fe^{3+} ions on *d* sites. The distances from the octahedral and tetrahedral sites to the common oxygen ion are 2 Å and 1.88 Å respectively, and the *a* - O^{2-}- *d* angle is 126.6°. Due to this ionic arrangement the super-exchange interactions is large. This interaction results in antiparallel alignment between the magnetic moments of the *a* site Fe^{3+}ions and those of the *d* site Fe^{3+} ions. The spontaneous magnetization of YIG arises only from Fe^{3+}ions having moment of

five Bohr magneton ($5\mu_B$) each. Since there are three Fe^{3+} ions on *d* sites for every two Fe^{3+} ions on *a* sites, the magnetic moment expected at T = 0 K per formula unit is 5 x 3 (*d* site)$-$5 x 2 (*a* site) = $5\mu_B$ per formula unit. This is an excellent agreement with the value of 4.96 μ_B found experimentally [73]. Yttrium iron garnet has cubic magneto-crystalline anisotropy with an easy axis along (111) direction. The first and second-order cubic anisotropy constants at room temperature are K_1= -6000 erg/cc and K_2= -260 erg/cc, respectively [70]. The room-temperature saturation magnetization M_s= 140 emu/cc (298 K) and the value of M_s at T = 0 K is 196 emu/cc [70]. A (111) YIG film has an out-of-plane effective anisotropy field ($2K_1/M_s$) of about 85 Oe and a threefold in-plane effective anisotropy field of less than 85 Oe. These fields are smaller in magnitude than the external magnetic fields used in typical experiments.

In YIG, the only magnetic ions are the ferric ions, and these are in an L = 0 state with spherical charge distribution. So their interaction with lattice deformation and phonons is weak. Due to this, YIG is characterised by very narrow linewidths in ferromagnetic resonance (FMR) experiments. The FMR linewidth originated from intrinsic damping in YIG crystals is about 0.2 Oe at 10 GHz [71]. This linewidth corresponds to an intrinsic Gilbert damping constant α of about 3×10^{-5}, which is about two orders of magnitude smaller than that in ferromagnetic metals [74]. It has the narrowest known FMR linewidth which results in larger magnon lifetime of a few hundred of nanoseconds as compared to the magnon lifetime in permalloy which is of the order of nanoseconds. Due to low damping in YIG, spin currents can propogate over centimetre distances [21]. This makes YIG the material of choice for studies of spin waves as well as magnetic insulator-based spintronics.

Yttrium iron garnet thin films are usually grown on (111) gadolinium gallium garnet (GGG) substrates. GGG has a cubic crystalline structure with 8 formula units per unit cell with lattice constant of 12.383 Å. Also their thermal expansion coefficient is very similar 1.04×10^{-5}/°C. This allows the epitaxial growth of nm-thick YIG films on GGG substrate.

2.3 Magnetization dynamics

2.3.1 Landau-Lifshitz-Gilbert (LLG) equation

The fundamental principle of magnetization dynamics is the precessional motion of magnetic moments under the influence of an effective magnetic field. This precessional motion is described phenomenologically by a torque equation called Landau-Lifshitz equation (LL equation) which was first proposed in 1935 by Lev Landau and Evgeny Lifshitz [75]. This equation was formulated by introducing a dissipation term to take into account the damping in the system. Later on Gilbert modified it by introducing a magnetic damping term [76].

The magnetic moment $\boldsymbol{\mu}$ is associated with total angular momentum $\mathbf{J}$ as

$$\boldsymbol{\mu} = \gamma \mathbf{J} \tag{2.1}$$

where $\gamma = g\mu_B/\hbar$ is the gyromagnetic ratio, g is the g-factor of the electron which is roughly equal to 2.002319, μ_B is the Bohr magneton and $\hbar = h/(2\pi)$ is the Planck constant.

A magnetic moment placed in an effective magnetic field $\mathbf{B}_{eff}$ experiences a torque:

$$\boldsymbol{\tau} = \boldsymbol{\mu} \times \mathbf{B}_{eff} \tag{2.2}$$

As $\boldsymbol{\tau} = \frac{d\mathbf{J}}{dt}$, so the equation of motion for $\mathbf{J}$ can be written as

$$\frac{d\mathbf{J}}{dt} = \boldsymbol{\mu} \times \mathbf{B}_{eff} \tag{2.3}$$

where $\mathbf{B}_{eff} = \mu_0 \mathbf{H}_{eff}$. Here, the effective magnetic field $\mathbf{H}_{eff}$ is the sum of external and internal magnetic fields as shown in equation 2.4. It includes the externally applied static field $\mathbf{H}_0$, the dynamic component of externally applied magnetic field $\mathbf{H}_M$(t), the field generated due to the exchange interactions $\mathbf{H}_{ex}$, the demagnetizing field $\mathbf{H}_d$ and the fields due to the shape and crystalline anisotropies $\mathbf{H}_{ani}$.

$$\mathbf{H}_{eff} = \mathbf{H}_0 + \mathbf{H}_M(t) + \mathbf{H}_{ex} + \mathbf{H}_d + \mathbf{H}_{ani} + ... \tag{2.4}$$

Now the atomic magnetic moment can be replaced by the macroscopic magnetization M in the continuum limit. The effective field exerts a torque on the magnetisation, corresponding to rate change of angular momentum due to which the magnetization starts to precess at Larmor frequency, $\omega = \gamma\mu_0 H_{eff}$. This precession of magnetization is described by the equation of motion called Landau-Lifshitz equation (LL equation):

$$\frac{d\mathbf{M}}{dt} = -\gamma\mu_0 \mathbf{M} \times \mathbf{H}_{eff} \tag{2.5}$$

According to equation 2.5, the system is non-dissipative and the magnetization would precess around the static field indefinitely without reaching the equilibrium position with lower energy configuration with **M** parallel to **H**, and this contradicts reality. So, in 1935 Landau and Lifshitz formulated the equation of motion by introducing damping term [75]:

$$\frac{d\mathbf{M}}{dt} = -\gamma\mu_0 \mathbf{M} \times \mathbf{H}_{eff} - \frac{\lambda}{M_s}\left[\mathbf{M} \times (\mathbf{M} \times \mu_0 \mathbf{H}_{eff})\right] \tag{2.6}$$

where λ is the damping constant. $\lambda = 1/\tau$ corresponds to the inverse relaxation time τ.

But this approach causes fast precession in case of large damping. In 1955, Gilbert [76] phenomenologically introduced a viscous damping term to circumvent this problem leading to the formulation of Landau-Lifshitz-Gilbert (LLG) equation:

$$\frac{d\mathbf{M}}{dt} = \underbrace{-\gamma\mu_0 \mathbf{M} \times \mathbf{H}_{eff}}_{\text{precessional term}} + \underbrace{\frac{\alpha}{M_s}\left(\mathbf{M} \times \frac{d\mathbf{M}}{dt}\right)}_{\text{damping term}} \tag{2.7}$$

where α is the dimensionless Gilbert damping parameter. This Gilbert damping parameter is viscous in nature, so with increase in the rotation of magnetisation $\frac{d\mathbf{M}}{dt}$, the damping of the system increases. Equation (2.7) consists of two terms: precessional and damping term. The magnetisation precesses along the applied field due to the torque proportional to (**M** x $\mathbf{H}_{eff}$) and the damping term is responsible for the relaxation of magnetisation towards the equilibrium state. Due to this damping term, the magnetisation follows a helical trajectory as shown in figure 2.2. It shows a realistic and damped precessional motion of the magnetisation around the effective magnetic

field. So we can say that the damping torque provides a dissipative mechanism through which energy and the spin angular momentum (magnon system) is transferred to the phonons in the lattice via spin-orbit interaction [77].

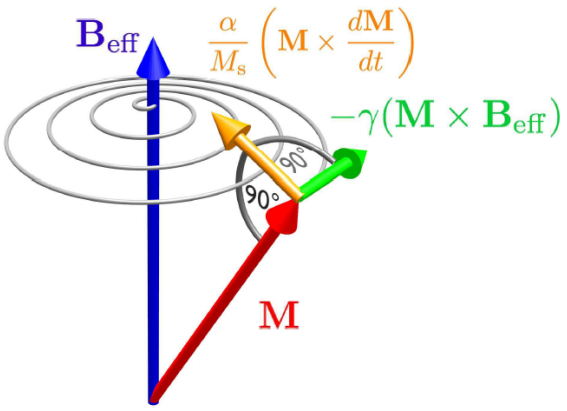

Figure 2.2: *Schematic illustration of the Landau-Lifshitz-Gilbert equation. The magnetisation* ***M*** *precesses along the applied field due to the torque (****M*** *x* $\boldsymbol{B}_{eff}$*). The Gilbert damping is responsible for the relaxation of magnetisation towards the equilibrium state, due to which the magnetisation follows a helical trajectory around* $\boldsymbol{B}_{eff}$ *[78].*

The origin of damping in magnetic materials is still not completely understood. In general, the damping can be understood through relaxation mechanisms which are divided into intrinsic and extrinsic categories. Direct coupling of magnons to the phonons in the lattice via spin orbit interaction are intrinsic contributions to the damping whereas scattering processes from electrons leading to magnon-magnon scattering are extrinsic processes.

2.3.2 Ferromagnetic resonance

Microwave absorption by ferromagnetic films at a resonance frequency different from the Larmor frequency of the electron spin was first observed by Griffiths in 1946 [79]. Later on, this phenomenon was theoretically explained as ferromagnetic resonance in magnetic material by Kittel [80, 81]. At ferromagnetic resonance, the magnetic

moments precess coherently with the same frequency and phase. The magnetisation dynamics of uniform precessional motion is described by the Landau-Lifshitz-Gilbert equation. The frequency of this uniform precession motion is called ferromagnetic resonance (FMR) frequency. The FMR mode describes the spin waves of infinite length. So, all the magnetic moments are parallel to each other and precess in phase in resonance condition. In this approach, the LLG equation is solved for small dynamic magnetic fields so as to calculate the resonance frequency. Now we will discuss the magnetic response of a ferrimagnet to small time-varying magnetic fields and obtain a small-signal susceptibility associated with magnetic resonance. This part is discussed based on the reference [70].

2.3.2.1 Susceptibility without damping

In this approach, let us assume that a small time dependent perturbation is added to a static equilibrium configuration. The equation of motion described by LL equation (2.5) can be linearised for small perturbations and the damping can be neglected. The fields can be divided into static and time-varying part as:

$$\mathbf{M} = \mathbf{M}_0 + \mathbf{m}(t) \tag{2.8}$$

$$\mathbf{H} = \mathbf{H}_0 + \mathbf{h}(t) \tag{2.9}$$

Here, we have assumed the magnetic field and magnetization have a harmonic time-dependence and the amplitudes of the dynamic components are small compared to the static components:

$$\mathbf{m}(t) = \mathbf{m}e^{-iwt}, |\mathbf{m}| \ll |\mathbf{M}_0| \tag{2.10}$$

$$\mathbf{h}(t) = \mathbf{h}e^{-iwt}, |\mathbf{h}| \ll |\mathbf{H}_0| \tag{2.11}$$

Again let us assume that both the static magnetic field and magnetization lie along the $\hat{\mathbf{z}}$ direction which corresponds to saturated single-domain configuration without anisotropy.

$$\mathbf{H}_0 = H_0\hat{\mathbf{z}} \tag{2.12}$$

$$\mathbf{M}_0 = M_0\hat{\mathbf{z}} \tag{2.13}$$

For small deviations from equilibrium, the $\hat{\mathbf{z}}$ component of the magnetization remains unchanged, $M_0 \approx M_s$. Substituting equations (2.10) and (2.11) in equation (2.5) gives the equation of motion as:

$$\frac{d\mathbf{m}}{dt} = \gamma\mu_0[\mathbf{M}_0 \times \mathbf{H}_0 + \mathbf{M}_0 \times \mathbf{h} + \mathbf{m} \times \mathbf{H}_0 + \mathbf{m} \times \mathbf{h}] \tag{2.14}$$

Since $\mathbf{M}_0$ is parallel to $\mathbf{H}_0$, the first term on RHS of equation (2.14) is zero. Also **m** and **h** are assumed to be small in magnitude, so the last term can be neglected. Finally, **h** and **m** have components only in the x- and y-directions. So using equations (2.10) and (2.11), the linearised equation of motion can be written as

$$-i\omega\mathbf{m} = \hat{\mathbf{z}} \times (-\omega_M\mathbf{h} + \omega_0\mathbf{m}) \tag{2.15}$$

where ω_M and ω_0 are defined as

$$\omega_M = -\gamma\mu_0 M_s, \quad \omega_0 = -\gamma\mu_0 H_0 \tag{2.16}$$

Re-writing the linearised equation (2.15) in matrix form for **h**

$$\begin{pmatrix} h_x \\ h_y \\ 0 \end{pmatrix} = \frac{1}{\omega_M} \begin{pmatrix} \omega_0 & i\omega & 0 \\ -i\omega & \omega_0 & 0 \\ 0 & 0 & 0 \end{pmatrix} \begin{pmatrix} m_x \\ m_y \\ 0 \end{pmatrix}$$

Transforming this equation into the form

$$\mathbf{m} = \overline{\boldsymbol{\chi}}.\mathbf{h} \tag{2.17}$$

where $\overline{\boldsymbol{\chi}}$ is defined as the Polder susceptibility tensor given by

$$\overline{\boldsymbol{\chi}} = \begin{pmatrix} \chi & -i\kappa & 0 \\ i\kappa & \chi & 0 \\ 0 & 0 & 0 \end{pmatrix} \tag{2.18}$$

with

$$\chi = \frac{\omega_0 \omega_M}{\omega_0^2 - \omega^2} \tag{2.19}$$

$$\kappa = \frac{\omega \omega_M}{\omega_0^2 - \omega^2} \tag{2.20}$$

Here, ω_0 is referred to as the ferromagnetic resonance frequency. It is observed that as $\omega \rightarrow \omega_0$, the elements χ and κ of $\overline{\boldsymbol{\chi}}$ become infinite. This is the case of an idealised lossless system. To avoid this singularity, the damping term is introduced and susceptibility with damping at resonance is derived [70].

2.3.2.2 Susceptibility with damping

The effect of damping can be introduced into the susceptibility equation by substituting

$$\omega_0 \rightarrow (\omega_0 - i\alpha\omega) \tag{2.21}$$

in the Polder susceptibility tensor. Then the linearised equation (2.15) can be written as

$$i\omega \mathbf{m} = \hat{\mathbf{z}} \times [\omega_M \mathbf{h} - (\omega_0 - i\alpha\omega)\mathbf{m}] \tag{2.22}$$

And the resonant susceptibility with loss is given by

$$\chi_+ = \frac{1}{Z - i\Omega\alpha - \Omega} = \chi_+^{'} + i\chi_+^{''} \tag{2.23}$$

where Z and the dimensionless frequency Ω are defined as

$$Z = \frac{H_0}{M_s}, \quad \Omega = \frac{\omega}{\omega_M} \tag{2.24}$$

From equation (2.23) $\chi_+^{'}$ and $\chi_+^{''}$ are given by [70]:

$$\chi_+^{'} = Re(\chi_+) = \frac{Z - \Omega}{(Z - \Omega)^2 + \Omega^2\alpha^2} \tag{2.25}$$

$$\chi_+^{''} = Im(\chi_+) = \frac{\Omega\alpha}{(Z - \Omega)^2 + \Omega^2\alpha^2} \tag{2.26}$$

So, the magnetic response consists of a Lorentzian profile ($\chi_+^{''}$) and a first derivative of Lorentzian ($\chi_+^{'}$). The imaginary part $\chi_+^{''}$ is responsible for damping. The maximum value of $\chi_+^{''}$ is 1/($\Omega\alpha$) and it occurs when Z-Ω = 0. The full width at half maximum ΔZ can be derived as follows:

$$\frac{\Omega\alpha}{(\Delta Z/2)^2 + \alpha^2\Omega^2} = \frac{1}{2\Omega\alpha} \tag{2.27}$$

This gives

$$\Delta Z = 2\Omega\alpha \tag{2.28}$$

$$\Delta B = \frac{2\omega\alpha}{\gamma} \tag{2.29}$$

or

$$\Delta H = \frac{2\omega\alpha}{\gamma\mu_0} \tag{2.30}$$

ΔZ, ΔB and ΔH correspond to the full resonance linewidth at half maximum. Equation 2.30 is used to find the damping of the magnetic materials.

2.4 Spin pumping

In a ferromagnet when a magnetisation motion is excited, a spin current can be pumped out from the ferromagnet into the paramagnet. This transfer of spin angular momentum from the ferromagnet to the conduction-electron spins in a paramagnet is called the spin pumping effect. The fundamental principle of the magnetisation dynamics in a ferromagnet can be described by the Landau-Lifshitz-Gilbert (LLG) equation (2.7). It was observed in 1999 that the Gilbert damping parameter of Cobalt was found to be increased when a non-magnetic metal is attached [15, 82]. Tserkovnyak et al. developed the spin pumping theory which explains the injection of a spin current from the ferromagnet into the non-magnetic metal due to the scattering at the time-dependent spin potential at the interface [30] .

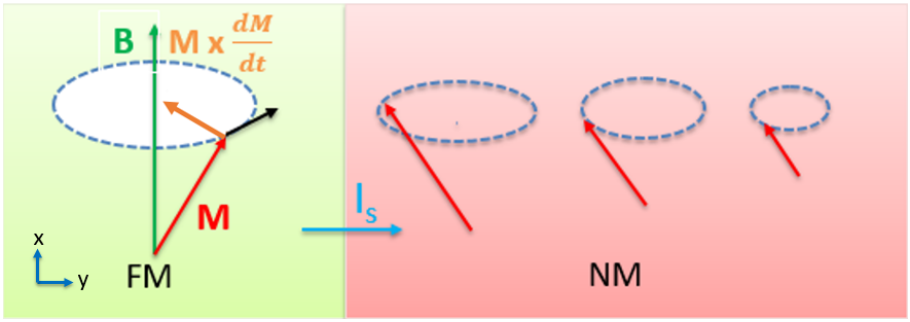

Figure 2.3: *Schematic illustration of the spin pumping process. The magnetization precession in a ferromagnetic (FM) leads to the injection of a spin polarized current I_s into the attached non-magnetic metal (NM).*

The basic principle can be explained in the following way. In equilibrium, in a ferromagnetic material the magnetization is aligned along the bias magnetic field. Now when we apply an alternating microwave magnetic field perpendicular to the external field a torque is exerted on the magnetisation due to which it starts to precess. In the FMR condition, the steady magnetization precession is maintained by balancing the absorption of the applied microwave and the dissipation of the spin angular momentum, i.e., the transfer of angular momentum from the local spins to conduction electrons. Under the FMR condition, the injection of a spin current will take place from the ferromagnet to the normal metal perpendicularly to the interface. Figure 2.3 shows the schematic illustration of the spin pumping process. The direction of emitted spin angular momentum is define by the spin current $\mathbf{I}_s$ which is given by [30]

$$\mathbf{I}_s = \frac{\hbar}{4\pi}\left(A_r\left(\mathbf{m}\times\frac{d\mathbf{m}}{dt}\right) - A_i\frac{d\mathbf{m}}{dt}\right) \tag{2.31}$$

Here $\mathbf{m}$ is the unit vector of magnetization, A_r and A_i are the interface scattering parameters which combine to give

$$A_r + iA_i = \sum_{mn}(\delta_{nm} - r^{\uparrow}_{mn}(r^{\downarrow}_{mn})^*) - \sum_{mn} t^{\uparrow}_{mn}(t^{\downarrow}_{mn})^* = G^{\uparrow\downarrow} - T^{\uparrow\downarrow} \tag{2.32}$$

where $r^{\uparrow}_{mn}$, $r^{\downarrow}_{mn}$, $t^{\uparrow}_{mn}$ and $t^{\downarrow}_{mn}$ are the reflection and transmission matrix elements of spin-up and spin-down electrons at the interface respectively. Here, m and n denote

the transverse modes at the Fermi energy before and after the scattering process [30, 83]. We can also see the angular momentum pumped into the attached non-magnetic metal per revolution is proportional to A_r (equation 2.31). It decays with time along the direction of applied magnetic field [30]. Here, $G^{\uparrow\downarrow}$ is the interface spin mixing conductance and $T^{\uparrow\downarrow}$ is the transmission coefficient. $G^{\uparrow\downarrow}$ describes the transport of spins at the interface non-collinear to the magnetization [83]. For ferromagnetic films which are thicker than the coherence length $\lambda_l = \pi/(k^{\uparrow} - k^{\downarrow})$, where $k^{\uparrow}$ and $k^{\downarrow}$ are the wave vectors of spin-up and spin-down electrons scattered or transmitted from one N-F interface incoherently at the other interface, $T^{\uparrow\downarrow}$ goes to zero [30]. Also, $A_i = \mathrm{Im}(G^{\uparrow\downarrow})$ vanishes for diffusive and ballistic contacts [30]. Therefore, $G^{\uparrow\downarrow}$ denotes the real part of the spin mixing conductance and hence equation 2.31 becomes

$$\mathbf{I}_s = \frac{\hbar}{4\pi} G^{\uparrow\downarrow} \mathbf{m} \times \frac{d\mathbf{m}}{dt} \tag{2.33}$$

During spin pumping, the magnetization precession loses its spin angular momentum due to the injection of spin current form the magnetic material into the non-magnetic metal, so this gives rise to the additional damping. Therefore, we can substitute α by the effective damping parameter α_{eff} which is the sum of the original damping α_0 and the spin pumping contribution $\Delta\alpha$:

$$\alpha_{eff} = \alpha_0 + \Delta\alpha \tag{2.34}$$

We can derive $\Delta\alpha$ from the conservation of the total angular momentum [84]. The temporal decay of the total spin $\mathbf{S}$ in the ferromagnetic layer equals the spin current $\mathbf{I}_s$:

$$\frac{d\mathbf{S}}{dt} = -\mathbf{I}_s \tag{2.35}$$

We know that the total spin $\mathbf{S}$ is related to magnetization as

$$\mathbf{S}(t) = \frac{\mathbf{M}}{\gamma} = \frac{M\mathbf{m}(t)}{\gamma} \tag{2.36}$$

where $\gamma = g\mu_B/\hbar$, μ_B is the Bohr magneton and g is the g-factor.

Thus it follows

$$\frac{d\mathbf{m}}{dt} = -\frac{g\mu_B}{\hbar M}\frac{d\mathbf{S}}{dt} \tag{2.37}$$

Equations (2.33) and (2.37) gives

$$\frac{d\mathbf{m}}{dt} = \Delta\alpha\left(\mathbf{m} \times \frac{d\mathbf{m}}{dt}\right) \tag{2.38}$$

with

$$\Delta\alpha = \frac{g\mu_B G^{\uparrow\downarrow}}{4\pi M} \tag{2.39}$$

Let us introduce $g^{\uparrow\downarrow}$ = $G^{\uparrow\downarrow}$/ A, where A is the interface area, then $\Delta\alpha$ can be expressed as

$$\Delta\alpha = \frac{g\mu_B}{4\pi M_s}\frac{g^{\uparrow\downarrow}}{d} \tag{2.40}$$

where d is the thickness of magnetic layer and M_s is the saturation magnetisation per unit volume. Hence, the effective Gilbert damping parameter is inversely proportional to the thickness of the magnetic layer. In reference [85], dependence of spin pumping effect on the thickness of YIG in YIG/Pt system has been reported. Also it has been shown that with decrease in film thickness the linewidth and the effective damping increases due to the magnetization relaxation through spin pumping in Pt.

2.5 Current induced FMR

Current induced FMR (CI-FMR) is a useful method to drive the magnetization dynamics by the current induced spin transfer torque. It allows us to quantify the contribution from the Oersted field and spin transfer torque in driving the magnetization dynamics in YIG/Pt bilayer structure. An oscillating charge current at microwave frequency flowing in a metal is accompanied by a transverse spin current $\mathbf{J}_s$ due to the spin orbit interaction. This spin current also oscillates at the same frequency and can exert a spin transfer torque (STT) on the magnetization **M**. This resonantly oscillating STT can drive the magnetization precession at ferromagnetic resonance condition. The current in the metal layer generates the Oersted field, can also drive the magnetization

precession. So, both the Oersted field and the spin current excites the magnetization dynamics inside the magnetic layer and thus it is difficult to distinguish. The magnetization dynamics are described by the Landau-Lifshitz-Gilbert equation, including the spin transfer and Oersted field torques:

$$\frac{d\mathbf{M}}{dt} = -\gamma\mu_0\mathbf{M}\times\mathbf{H}_{eff} + \frac{\alpha}{M_s}\left(\mathbf{M}\times\frac{d\mathbf{M}}{dt}\right) + \frac{\gamma\hbar}{2eM_sd_F}\mathbf{J}_s \tag{2.41}$$

where $\mathbf{H}_{eff}$ is the effective magnetic field and α is the Gilbert damping parameter. M_s and d_F are the saturation magnetization per unit volume and thickness of the YIG film.

The magnetization dynamics can be detected electrically as a DC voltage generated via spin pumping and the rectification mechanism of the spin Hall magnetoresistance (SMR). From the lineshape and symmetry of the DC voltage we can understand the nature of the torque acting on the system. Spin pumping is described as the symmetric contribution to the Lorentzian lineshape whereas spin rectification consists of both symmetric and anti-symmetric components in a Lorentzian curve. At the resonance condition, the oscillating magnetization results in a time-dependent SMR in the metal layer at the same frequency: $R = R_0 + \Delta R\cos^2\theta(t)$, which rectifies the AC current and generates a DC voltage along the bar. The spin rectification DC voltage is given by [86]:

$$V_{DC} = V_{sym-SR}\frac{\Delta H^2}{(H_{ext}-H_{res})^2+\Delta H^2} + V_{asy-SR}\frac{\Delta H(H_{ext}-H_{res})}{(H_{ext}-H_{res})^2+\Delta H^2} \tag{2.42}$$

where symmetric V_{sym-SR} and anti-symmetric V_{asy-SR} are Lorentzian components:

$$V_{sym-SR} = \frac{I_0\Delta R}{2}\frac{\sqrt{H_{res}(H_{res}+M_{eff})}}{\Delta H(2H_{res}+M_{eff})}h_{ST}\sin 2\theta \tag{2.43}$$

$$V_{asy-SR} = \frac{I_0\Delta R}{2}\frac{(H_{res}+M_{eff})}{\Delta H(2H_{res}+M_{eff})}h_{Oe}\sin 2\theta\cos\theta \tag{2.44}$$

where ΔH, H_{ext} and H_{res} are the linewidth, external applied magnetic field and the resonant field, respectively; θ is the angle between the applied field and the microwave current I_0e^{jwt} and M_{eff} is the effective magnetization. Thus, Oersted field h_{Oe} induces anti-symmetric components V_{asy-SR} and the V_{sym-SR} is induced by the out-of-plane

field h_{ST} which is responsible for an anti-damping like spin transfer torque. Figure 2.4 shows the schematic of CI-FMR in YIG/Pt bilayer sample with its measurement circuit.

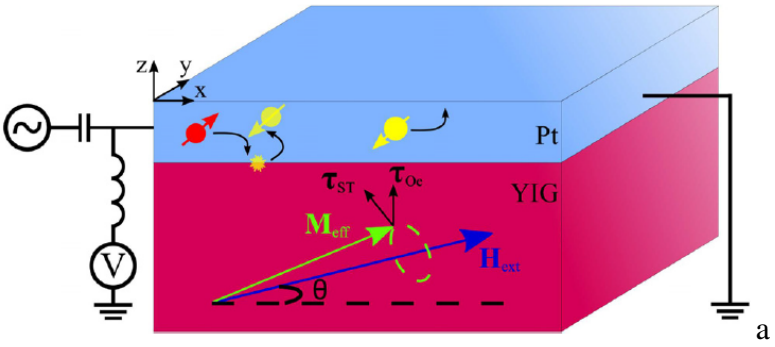

Figure 2.4: *Schematic of a YIG/Pt bilayer thin film illustrating the spin transfer torque τ_{ST} and the Oersted field torque τ_{Oe} driving the magnetization precession about the external field H_{ext}. It is also showing the circuit for CI-FMR measurement where a bias-Tee is used for the transmission of a microwave signal and dc voltage detection simultaneously, via lock-in technique across the Pt bar [86].*

Schreier *et al.* reported the experiment on in-plane CI-FMR in YIG/Pt, in which they found the magnetization dynamics in thinnest YIG sample (4 nm) is driven by the spin transfer torque [87]. Researchers also reported the direct imaging of electrically driven spin-torque FMR (ST-FMR) in YIG by spatially-resolved Brillouin light scattering (BLS) spectroscopy [88]. In our work, we used CI-FMR to drive the magnetization dynamics in YIG/Pt layer with YIG of varying thickness and to investigate the contribution from the Oersted field and spin-transfer torque.

2.6 Spin current and Spin diffusion

An electron has an internal angular momentum. This angular momentum is due to the spin of the electron. The flow of spin is called a spin current. This plays the similar role as the flow of charge in an electrical current. A charge current is defined in terms of the

charge conservation law. The continuity equation of charge, which is a representation of the charge conservation law, defines a charge current density $\mathbf{j}_c$ [89]:

$$\dot{\rho} = -\boldsymbol{\nabla} \cdot \mathbf{j}_c \tag{2.45}$$

However, spin is not conserved completely due to the spin relaxation and it obeys the continuity equation [90]:

$$\frac{d\mathbf{M}}{dt} = -\boldsymbol{\nabla} \cdot \mathbf{j}_s + \mathbf{T} \tag{2.46}$$

The term $\mathbf{T}$ represents the nonconservation of spin angular momentum due to the relaxation and generation of spin angular momentum. Here $\mathbf{M}$ denotes the magnetisation and $\mathbf{j}_s$ is the spin current density. The basic phenomenological model for the spin relaxation can be defined as [90]:

$$\mathbf{T} = -(\mathbf{M} - \mathbf{M}_0)/\tau \tag{2.47}$$

wher τ is a decay time constant and $(\mathbf{M} - \mathbf{M}_0)$ is the nonequilibrium magnetization measured from equilibrium value $\mathbf{M}_0$.

In a ferromagnet/normal metal bilayer structure, a spin current can be injected from a ferromagnet (FM) into a normal metal (NM). Figure 2.5 shows a spin current in a FM/NM junction with a charge current passing through the interface. For a diffusion or drift spin current the driving force is a gradient of the difference in the spin dependent electrochemical potential for spin up ($\mu_\uparrow$) and spin down ($\mu_\downarrow$). With this the charge current density j_c and spin current density j_s can be written as [90]:

$$j_c = j_\uparrow + j_\downarrow = \frac{1}{e}\boldsymbol{\nabla}(\sigma_\uparrow \mu_\uparrow + \sigma_\downarrow \mu_\downarrow) \tag{2.48}$$

$$j_s = j_\uparrow - j_\downarrow = \frac{1}{e}\boldsymbol{\nabla}(\sigma_\uparrow \mu_\uparrow - \sigma_\downarrow \mu_\downarrow) \tag{2.49}$$

where $\sigma_\uparrow$ and $\sigma_\downarrow$ represents the spin up and spin down conductivity respectively.

The continuity equations for charge and spin in the steady state are

$$\boldsymbol{\nabla}.(\mathbf{j}_\uparrow + \mathbf{j}_\downarrow) = 0 \tag{2.50}$$

$$\nabla.(\mathbf{j}_{\uparrow} - \mathbf{j}_{\downarrow}) = -e\frac{\delta n_{\uparrow}}{\tau_{\uparrow\downarrow}} + e\frac{\delta n_{\downarrow}}{\tau_{\downarrow\uparrow}} \tag{2.51}$$

where $\delta n_{\uparrow(\downarrow)}$ is the deviation from equilibrium carrier density for spin up (spin down), and $\tau_{\uparrow\downarrow}$ is the scattering time of an electron from spin state $\uparrow$ to $\downarrow$ or vice-versa. Using the continuity equations and balance principle $\frac{N_{\uparrow}}{\tau_{\uparrow\downarrow}} = \frac{N_{\downarrow}}{\tau_{\downarrow\uparrow}}$, which means that in equilibrium there is no net spin scattering, we obtain the basic equations that describe the charge and spin transport as [90]:

$$\nabla^2(\sigma_{\uparrow}\mu_{\uparrow} + \sigma_{\downarrow}\mu_{\downarrow}) = 0 \tag{2.52}$$

$$\nabla^2(\mu_{\uparrow} - \mu_{\downarrow}) = \frac{1}{\lambda_{sd}^2}(\mu_{\uparrow} - \mu_{\downarrow}) \tag{2.53}$$

Equation 2.53 is known as the spin diffusion equation. Here, $\lambda_{sd} = \sqrt{D}\tau_{sf}$ is the spin diffusion length, D is the spin-averaged diffusion constant and τ_{sf} is the spin relaxation time.

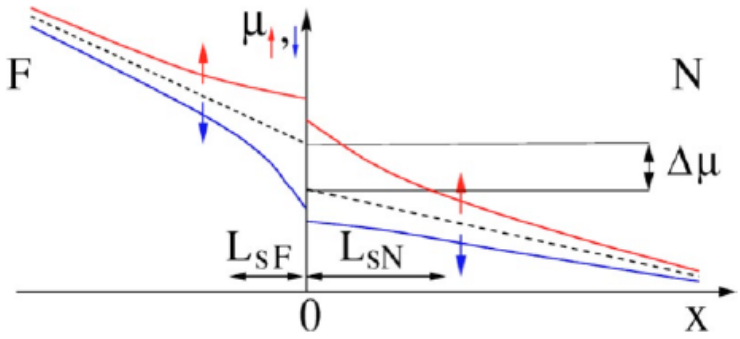

Figure 2.5: *Spatial variation of the spin dependent electrochemical potentials across a current carrying interface at an ferromagnet/normal metal (FM/NM) junction. The decay of spin accumulation away from the interface is characterised by the spin diffusion lengths L_{sF} and L_{sN} in the FM and NM regions, respectively [91].*

In a FM/NM junctions, when a spin polarised current passes into the normal metal the chemical potentials for the spin up and spin down diverge over a short range, over which spin accumulation occurs in the NM. In nonmagnetic metals, the electrical conductivity is spin-independent, and the charge current has no spin polarisation. So the

non-conservation of spin current takes place over a spatial axis defined by the spin diffusion length. As the conduction electrons move into the NM the chemical potentials have to be continuous but due to the interface contact resistance there can be a small difference. The gap between the dashed lines $\Delta\mu$ is called the spin accumulation. The spin accumulation ($\mu_\uparrow$ - $\mu_\downarrow$) decay away from the interface into the FM and NM regions. In the NM, this spin accumulation decays over a spin diffusion length L_{sN}. In the FM near the interface there is a back flow of spin polarised electrons over a distance L_{sF}, induced by the accumulation in the NM.

2.7 Spin Hall effect and inverse spin Hall effect

The spin Hall effect (SHE) is the generation of transverse spin current by an electric charge current with spins oriented perpendicular to the two currents [92]. Electrons with spin up will be scattered in one direction perpendicular to the flow of the electric charge current and electrons with spin down in the opposite direction (figure 2.6a). It does not require any magnetic field. This effect was first predicted theoretically in 1971 by D′yakonov and Perel [93, 94]. But this theoretical work received the attention of the spintronics community when it was rediscovered by Hirsch [32] and Zhang [34] in 1999. The reverse effect is the inverse spin Hall effect (ISHE) which describes the generation of a transverse electric charge current in a normal metal by the injection of a spin polarised current (figure 2.6b). Experimentalists have been able to measure and quantitatively study the spin Hall effect and its inverse in a variety of systems, such as in semiconductors like ZnSe [95] and GaAs [96–98], and metals, for example, Al [99] and Pt [100, 101].

SHE is a consequence of spin orbit interactions [102]. The expression for the spin-orbit interaction in vacuum is [103]:

$$H_{SO} = -\frac{\lambda_0^2}{4\hbar}[\mathbf{p} \times \nabla V(\mathbf{r})].\boldsymbol{\sigma} \tag{2.54}$$

where λ_0 = $\hbar$/mc $\simeq$ 3.9 x 10^{-3}Å is the Compton wavelength of the electron divided

by 2π, $\mathbf{p}$ is the momentum, $V(\mathbf{r})$ is the potential acting on the electron and $\boldsymbol{\sigma}$ is the vector of the Pauli matrices. Traditionally this form is explained as the relativistic transformation of the electric field ∇V to the rest frame of the electron [103]. In solids, the impurity potential gives rise to an additional electric field due to which an electron passing through this field feels an effective magnetic field. This leads to spin-orbit coupling

$$H_{SO}(\mathbf{k}) = -\frac{1}{2}\boldsymbol{\sigma}.\mathbf{B}(\mathbf{k}) \tag{2.55}$$

where $\mathbf{B}(\mathbf{k})$ is an effective $\mathbf{k}$-dependent magnetic field for the electron band considered. This results in a spin dependent perturbation on the conduction electron momentum.

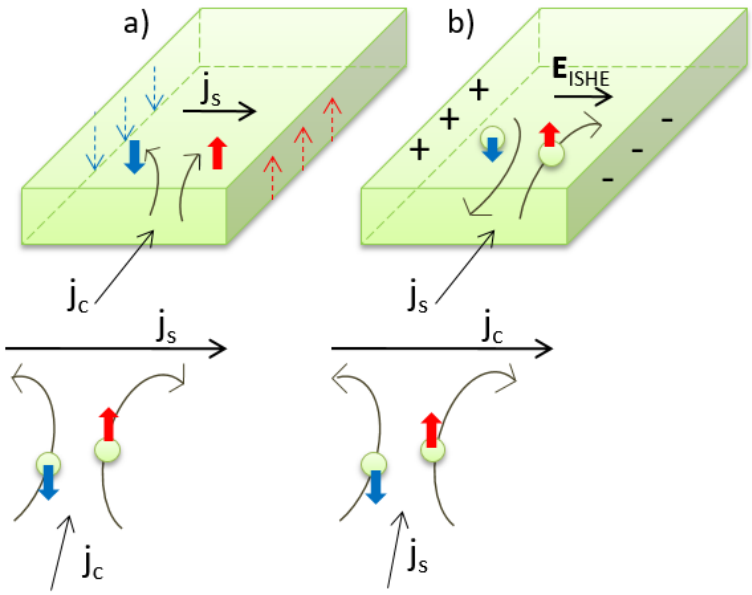

Figure 2.6: *(a) The spin Hall effect (SHE) describes the generation of a spin polarised current (j_s) in a normal metal perpendicular to the charge current (j_c). (b) The inverse spin Hall effect (ISHE) refers to the generation of a charge current (j_c) in a normal metal perpendicular to a spin polarised current (j_s).*

The spin Hall effect can be classified between extrinsic SHEs and intrinsic SHEs depending on the mechanisms. The instrinsic mechanim is related to the spin-dependent band structure of the material [105]. Basically, this mechanism lies in the precession

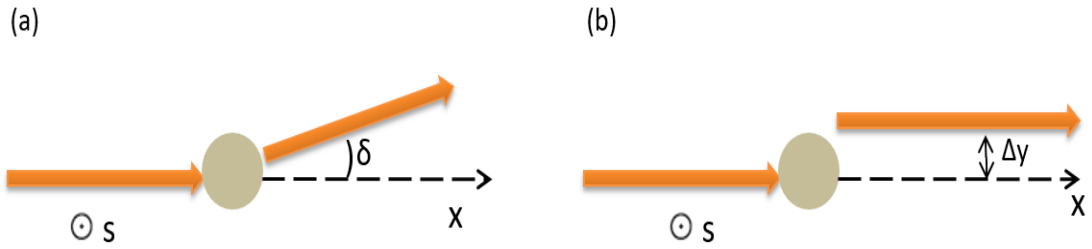

Figure 2.7: *Average motion of an electron after scattering by a central potential in the presence of spin-orbit interaction. (a) Illustration of skew scattering, where the trajectory is deflected by an angle δ after the collision with the impurity. (b) Schematic of the side jump mechanism showing a side jump of Δy from the original trajectory. The spin of the electrons* ***S*** *is directed normal to the plane. Based on [104].*

of spins about the effective magnetic field **B**(**k**) that characterises the band structure. Intrinsic effects can be neglected in metals as the dominating contributions arise due to the extrinsic effects. In our research, Pt was used in spin pumping and current induced FMR experiments, so we focus here on the details of extrinsic effects. The extrinsic mechanism is governed by the spin-orbit interaction with impurities in the crystal, the two forms of this mechanism are: skew scattering and the side-jump mechanisms. Skew scattering is the result of asymmetric scattering of spin up and spin down electrons by a central potential in the presence of spin-orbit interaction [106, 107]. The schematic is shown in figure 2.7a. After having a collision with an impurity, the trajectory of the electrons is deflected at an angle δ. This effect is used to create a spin polarization from an unpolarized beam of electrons. The expression for the skew-scattering contribution to the spin Hall conductivity [103]:

$$\sigma_{ss}^{SH} = \sigma_s \rho_{ss} \sigma_c \tag{2.56}$$

where σ_c is the Drude conductivity, σ_s is the spin conductivity and resistivity $\rho_{ss} = m^*/ne^2\tau_{ss}$. Here, n is the electron density, m^* is the effective mass of the conduction band and $1/\tau_{ss}$ is the skew scattering rate.

The side-jump mechanism originates from the anomalous form of the velocity operator in spin-orbit coupled systems [104, 108]. It is regarded as a discontinuous finite displacement of an electron (represented by a wave packet) transverse to the original direction. This effect arises due to random collisions of electrons with impurities. The jump is not necessarily transverse to the incident wave direction as it can happen in all possible directions. Since the displacement is the same for spin up and spin down electrons but in opposite directions, a spin current perpendicular to the initially unpolarised charge current is generated. The side-jump contribution to the spin Hall conductivity is given by [103]:

$$\sigma_{sj}^{SH} = -2\frac{e^2}{\hbar} n \lambda_c^2 \tag{2.57}$$

where λ_c is the coupling constant of the conduction band and n is the electron density. Thus, the spin Hall conductivity is expressed as the sum of two contributions: $\sigma^{SH} = \sigma_{ss}^{SH} + \sigma_{sj}^{SH}$.

The spin Hall resistivity ρ_H has a linear and a quadratic term in the electric resistivity ρ [109]:

$$\rho_H = a_{skew}\rho + b_{side}\rho^2 \tag{2.58}$$

where a_{skew} and b_{side} are temperature dependent parameters which describes the skew scattering and side jump contribution, respectively.

The spin current density j_s and charge current density j_c are coupled by the following equations [109]:

$$j_c = j_c^0 + \theta_{SHE}\frac{2e}{\hbar}(j_s \times \sigma) \tag{2.59}$$

$$j_s = j_s^0 + \theta_{SHE}\frac{2e}{\hbar}(j_c \times \sigma) \tag{2.60}$$

where j_c^0 and j_s^0 are the original current densities, θ_{SHE} is the spin Hall angle and σ is the spin polarization vector. The spin Hall angle θ_{SHE} is a material parameter and it is the sum of the contribution from skew scattering and side jump scattering mechanisms. The measure of spin Hall effect is given by the spin Hall angle θ_{SHE}, which is defined as the ratio of the spin conductivity and the electrical conductivity. From equation 2.59

and 2.60, it appears that a spin current induces a transverse charge current, while a charge current generates a transverse spin current.

The spin current injected into the non-magnetic metal layer decays along the y-axis (fig.2.3) due to spin relaxation as [110]:

$$j_s(y) = \frac{sinh\frac{d_N - y}{\lambda_{sd}}}{sinh\frac{d_N}{\lambda_{sd}}} j_s^0 \tag{2.61}$$

where d_N is the normal metal thickness, λ_{sd} is the spin-diffusion length and j_s^0 is the spin-current density at the interface. The spin pumping induced spin current is transformed into charge current by ISHE. Here j_c^0 is zero, so eq. 2.59 becomes

$$j_c = \theta_{SHE}\frac{2e}{\hbar}(j_s \times \sigma) \tag{2.62}$$

Substituting j_s using equation 2.61 in eq. 2.62 and averaging over the Pt thickness yields the average current density which is given by [110]:

$$\bar{j}_c = \frac{1}{d_{Pt}}\int_0^{d_{Pt}} j_c(y)dy = \theta_{SHE}\frac{2e}{\hbar}\frac{\lambda_{sd}}{d_{Pt}}\tanh\left(\frac{d_{pt}}{2\lambda_{sd}}\right)j_s^0 \tag{2.63}$$

where d_{Pt} is the thickness of the Pt and λ_{sd} is the spin diffusion length. With A as the cross-sectional area of the Pt layer, the ISHE charge current is given by I_{ISHE} = A $\bar{j}_c$. Hence, the ISHE voltage is E_{ISHE} = I_{ISHE}R, where R is the electrical resistance of the Pt layer.

CHAPTER 3

Experimental Methods

3.1 Introduction

This chapter starts with the introduction of deposition technique of nanometre thick Yttrium iron garnet films and various experimental techniques employed for the characterisation of thin films of YIG. The first section will address the deposition of YIG by RF magnetron sputtering and the process of growing YIG/Pt and YIG/C_{60} bilayer structures. The structural characterisation of thin YIG films involves x-ray reflectivity (XRR) and x-ray diffraction (XRD) in order to determine the thickness, crystallinity and the film quality. The surface roughness of the films was determined using atomic force microscopy (AFM). The magnetic properties of the films are analysed using vibrating sample magnetometer (VSM) and superconducting quantum interference devices (SQUID) VSM. For detailed investigation of the magnetization behaviour at low temperature, we further carried out a temperature dependent polarised neutron reflectometry (PNR) experiment. We also used Ferromagnetic resonance (FMR) techniques to investigate the magnetization dynamics of our films and hence to estimate the value of damping parameter in our nm-thick sputtered YIG films.

3.2 Deposition: DC and RF sputtering

Sputtering is a physical vapour deposition of thin films on the substrates. This technique belongs to the category of plasma deposition. In this process, sputtered gas is ionized electrically to form a plasma, followed by removal of the target material by ion bombardment and ejection of material from the target to the substrate. The main advantages of sputtering are: (a) High deposition rate for DC sputtering. (b) Film uniformity over large areas. (c) Surface smoothness and thickness control. (d) It is a versatile process as it is based on the momentum transfer and not on thermal or chemical reaction, so any kind of material can be sputtered.

The sputtering deposition chamber consists of two electrodes in a vacuum with an external high voltage power supply. The material to be deposited, is called the target

and acts as the cathode, the substrates are placed on the sample wheel which is earthed. A schematic diagram of a sputtering system is shown in 3.1. The sputtering gas is introduced into the vacuum chamber. To sputter an atom from the target, momentum transfer from the ion-induced collision must overcome the surface barrier, given by the surface binding energy. When a voltage is applied between the cathode and anode, an electric discharge is produced. This leads to the partial ionization of the gas and these ions when strike the target with sufficient energy cause ejection of surface atoms from the target and deposition onto the substrate. During this the ionized gas and the free electrons are accelerated by the voltage and continue to collide, causing further ionization of the gas. Finally, a breakdown condition is reached and the plasma is stabilized. The principal source of electrons to sustain the plasma is the secondary electron emission. Sputter Yield gives a measure of ejected surface atoms, and is defined as the ratio between the mean number of ejected atoms from the surface and the number of incident ions bombarding the target. The sputter yield is influenced by the following factors [111]: (a) energy of incident particles (b) the atomic weights of the ion and the target atom (c) incident angles of particles (d) crystal structure of the target surface. The sputter yield shows maximum value in a high-energy region of 10 to 100 keV. The high yield is observed at incident angles between 60° - 80° [111].

Sputtering methods can be classified as DC and RF sputtering depending on the material to be deposited. DC sputtering is used for the metal deposition whereas RF sputtering for the deposition of thin films of insulator. In DC sputtering, a DC voltage ($\sim$ 400 V) is applied to create plasma between the electrodes. In RF sputtering, a voltage oscillating at radio frequency (RF), typically around 13.56 MHz, is applied to bias the electrode and to sustain the glow discharge. As the current is alternating, this will prevent build up of a surface charge of positive ions on the front side of the insulator. On the positive cycle, electrons are attracted to the cathode, creating a negative bias and on the negative cycle, ion bombardment of the target to be sputtered continues. The sputtered atoms are ejected, which are then deposited on the substrate. For magnetron sputtering, permanent magnets are placed beneath the target so as to

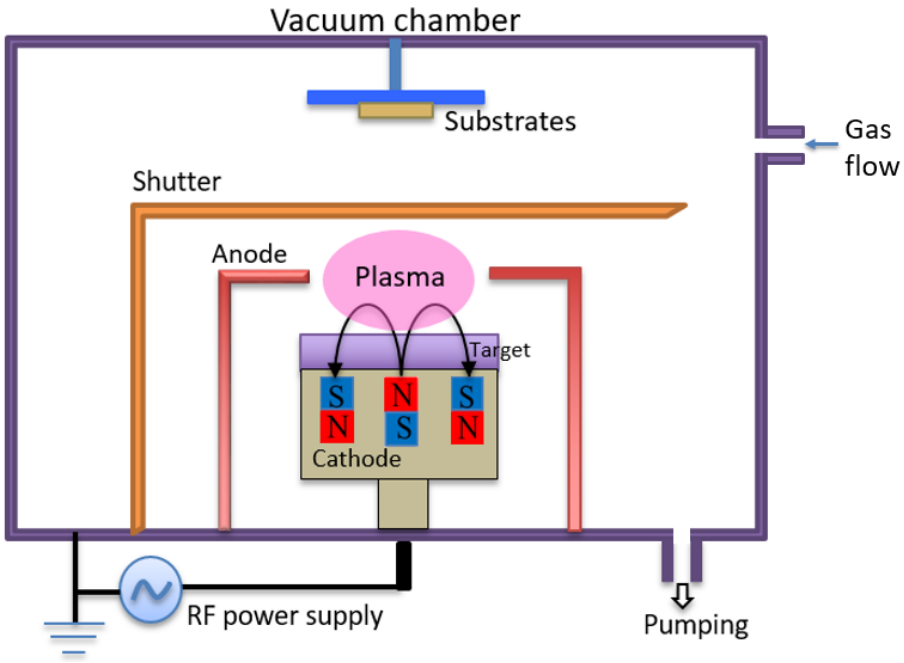

Figure 3.1: *A schematic diagram of an on-axis sputtering system. A RF voltage is applied between cathode (target) and anode (the target can), after introducing sputtering gas to the evacuated chamber. The argon atoms are ionised due to the accelerated electrons between the electrodes resulting in a plasma. Due to the bombardment of the ionised ions on the target, materials are ejected from the surface of the target and get deposited on the substrate.*

confine the plasma by the Lorentz force. The ejected electrons show cycloidal motion and the centre of the orbit drifts in the direction of $\vec{E}$ x $\vec{B}$, where $\vec{E}$ and $\vec{B}$ denote the electric field in the discharge and the transverse magnetic field, respectively (fig.3.2a). The magnetic field is oriented such that these drift paths for electrons form a closed loop around the target that can act as electron trap, shown in figure 3.2b. This electron trapping effect increases the probability of ionization of the sputtering gas and hence the plasma density, which effectively increases the deposition rate.

Our on-axis sputtering system consists of seven sputtering guns, two for magnetic, one for insulator, four guns for metal deposition and one evaporation source for the deposition of C_{60} by thermal sublimation. The sample wheel has 16 different slots for the substrate. There is a shutter system which allow us to grow multilayers of dif-

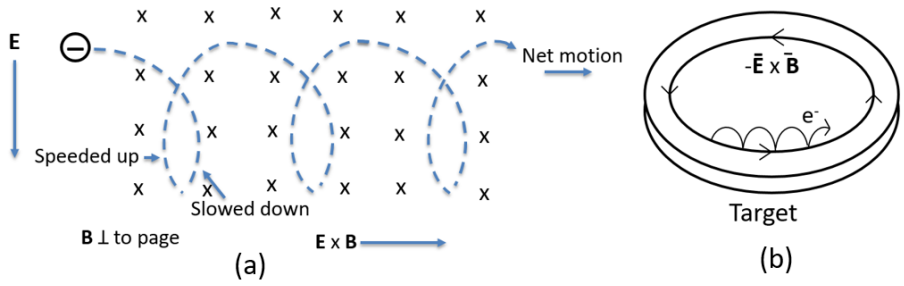

Figure 3.2: *(a) The motion of an electron in presence of an electric and magnetic fields forms a closed loop. (b) The electron drift in the direction of* ***E x B*** *with drift velocity of E/B, executing a cycloidal path.*

ferent materials. We control the sample wheel and the shutter position remotely by using software. The target-to-substrate distance is about 7 cm. Sputtering is carried out under high vacuum conditions with a base pressure of about 10^{-8} Torr. At first, the chamber is evacuated to a pressure of 10^{-7} by using a roughing pump and a cryopump. The pressure is further decreased to a base of 2 x 10^{-8} Torr using a liquid nitrogen trap called Meissner trap, to condense the residual water vapour from the atmosphere. Our thin films of YIG were grown on (111) GGG substrates by RF magnetron sputtering. The deposition rate is greatly influenced by the RF power, pressure, temperature and the flow of sputtering gas. During the deposition of YIG films, the system had a base pressure of 2×10^{-8} Torr in the main chamber, argon and oxygen flow rate was 22.4 SCCM (standard cubic centimetres per minute) and 1.2 SCCM respectively to maintain the proportion of O_2 /Ar = 5 % and the RF power was maintained at 50 W at 13.56 MHz. There is an impedence-matching network between the power supply and discharge chamber, which is tuned to get zero reflected power back to the source. The target and inductance in the matching network are always water-cooled. The electrical resistivity of the cooling water should be high enough to provide electrical insulation. The as-deposited YIG film is amorphous, so the deposited YIG is believed to be deposited as a mixture of its constituent elements. The different elements of YIG have different masses, so the sputter rate for each element will be different and also they

will have different mean free path. By adding oxygen to the argon atmosphere, we slow down the growth rate and allow the yttrium and iron to be deposited as the correct stoichiometry for YIG. The deposition rate used was 0.29 Å/s (Old Target: Target-A). The rate was determined from the thickness of each sample obtained after fitting the x-ray reflectivity curve. Under this deposition condition thin films of YIG of varying thicknesses were deposited on GGG. Later, with the change to a new YIG target (Target-B), the rate was around 0.16 Å/s under the same deposition conditions.

For YIG/C_{60} bilayer structures, C_{60} molecules were deposited on annealed YIG by thermal sublimation. The C_{60} molecules are placed in a crucible in powder form and the crucible is connected to a tungsten filament. When a high current about 20.8 A is applied to the copper rods attached to the tungsten filament, the temperature of the crucible rises and due to this high temperature the molecules are thermally sublimated and deposited on the YIG surface. A water cooling system is arranged with the evaporation source to avoid excessive radiative heating. During the growth of C_{60}, a quartz crystal monitor is used to determine the thickness of the C_{60} layer. After each growth, thickness is measured and the tooling factor of the monitor is calibrated accordingly so as to get the accurate thickness of C_{60} layer.

Our YIG/Pt bilayer samples are made by deposition of Pt by DC magnetron sputtering on annealed YIG samples. Before deposition of Pt the samples are cleaned in ultrasonic bath using acetone and isopropanol. The deposition rate of Pt was 1.65 Å/s at 25 mA with power of 9 W.

3.3 Annealing

The as-deposited YIG films are amorphous and non-magnetic, so it is required to anneal them to get crystalline YIG along the GGG crystalline plane. For annealing, the samples are first cleaned using acetone and isopropanol. Then the samples are immediately placed in a tube furnace to anneal them at 850 °C for two hours under open air conditions. Care was taken to keep the samples within a 15 cm region in the centre

of the furnace where the temperature was approximately uniform. The heating and cooling cycles are run at a rate of 7°C per minute to avoid strain on the films. For the deposition of Pt and C_{60} on YIG, the samples need to be reloaded into the sputtering chamber after annealing.

3.4 Structural Characterisation

3.4.1 X-ray reflectivity (XRR)

X-ray reflectivity is a useful and non-destructive technique for the structural characterisation of thin films. This technique is used to determine the thin film parameters: thickness, density and surface or interface roughness. When x-rays are incident on the sample, the refractive index of the material n is slightly less than one, given by

$$n = 1 - \delta \tag{3.1}$$

where $\delta = \frac{2\pi\rho r_0}{k^2}$. Here, ρ, r_0 and **k** are the electron density, Bohr radius and wave vector of the radiation, respectively. δ is the order of 10^{-5}. When x-rays are incident on a sample at a grazing angle lower than the critical angle of incidence θ_c, they undergo total reflection and do not enter the sample. When the angle of incidence $\theta > \theta_c$, refraction occurs and x-rays penetrate in the material.

Snell's law of refraction gives the relationship between the angle of incidence θ and angle of refraction θ' which is given by

$$\cos\theta = n\cos\theta' \tag{3.2}$$

The critical angle can be derived from the Snell's law by putting $\theta' = \theta_c$ and expanding the cosine in Snell's law to give the expression for critical angle. The critical angle of incidence θ_c is given by the formula:

$$\theta_c = \sqrt{2\delta} = \sqrt{\frac{4\pi\rho r_0}{k^2}} \tag{3.3}$$

Thus, the critical angle provides the information about electron density of the reflecting material [112, 113].

The reflectivity is measured at grazing incidence including the straight-through beam such that the region below $\sim$ 0.4 $^\circ$ is due to the instrument function i.e. the beam optics. This is immediately followed by a sharp decrease in the intensity at the critical angle: the point where the beam just penetrates the top surface. The reflected profile shows oscillations caused by the interference of x-rays reflected from the surface of the film and the interface between the film and the substrate. These oscillations are known as Kiessig fringes [114]. By analysing the reflectivity intensity curves we can determine the thickness, density, surface and interface roughness of the thin films. The quality of the fit gives us confidence that the top layer is stoichiometrically correct (section 4.2.1). The amplitude of oscillations depends on the difference in the densities of the film and the substrate. The higher the amplitude of oscillations larger the difference. So the amplitude of oscillations and the critical angle provide information about the density of film. From the decay rate of reflectivity, we can determine the roughness of the film. For a larger surface roughness reflectivity decreases rapidly, so larger the surface roughness, the faster the decay of oscillations. The angular positions of oscillation give information about the thickness of the film. The thickness of the film, t, can be determined by analysing the angular distributions of the resulting interference pattern using the Kiessig equation:

$$\lambda = 2t\sqrt{\sin^2\theta_n - \sin^2\theta_c} \tag{3.4}$$

where n is an integer, λ is the wavelength and θ_n is the angular position of constructive peaks [113, 115].

3.4.2 X-ray diffraction (XRD)

X-ray diffraction is a technique used for the determination of the crystal structure of the material. This technique is based on the coherent interference of scattered waves

from electron dense regions. When electromagnetic radiation, x-rays with wavelength comparable to the atomic spacing of the crystal are incident on the atomic planes and are scattered by the atoms in the crystal, then diffraction occurs. In order to interfere constructively from the successive crystallographic planes, scattered rays must satisfy the condition given by Bragg's law:

$$n\lambda = 2d_{hkl}\sin\theta \tag{3.5}$$

where n is an integer determined by the order of the diffraction peak, λ is the wavelength and d_{hkl} is the lattice spacing. This law is the basis of XRD that produces Bragg's peak in high angle scan. This equation was first derived in 1913 by Sir W.H. Bragg and his son Sir W.L. Bragg to explain why cleavage faces of crystals reflect x-ray beam at a certain angles of incidence. In our system, Cu-K_α x-rays are produced from a copper target with a characteristic wavelength of λ =1.54 Å. To generate x-rays, a tungsten filament is heated up and surface electrons are emitted via thermionic emission. A high voltage is applied to accelerate these electrons towards a copper target. These high energy electrons hit the target, lose their kinetic energy, and can cause electrons from the K shell in the metal atoms to be knocked out. This hole is then filled up by the electrons dropping from the L and M shells, which results in the emission of x-ray photons with an energy corresponding to the difference between the energy levels with characteristic wavelength of Cu K_α and Cu K_β. These x-ray photons pass through a series of slits and filters to produce collimated monochromatic beam and filter out the Cu K_β.

Figure 3.3a shows an incident x-ray beam interacting with the atoms arranged in a periodic manner in a lattice plane. The atoms are represented as spheres forming different set of lattice planes in the crystals, designated by Miller indices. Here, Bragg's Law illustrates that a set of parallel planes with index hkl and lattice spacing d_{hkl} generates a diffracted beam when x-rays of wavelength λ incident on the atoms at an angle θ and are reflected at the same angle. Figure 3.3b shows the basic components of an XRD set up, consisting of an x-ray source, sample stage and the detector. X-rays are

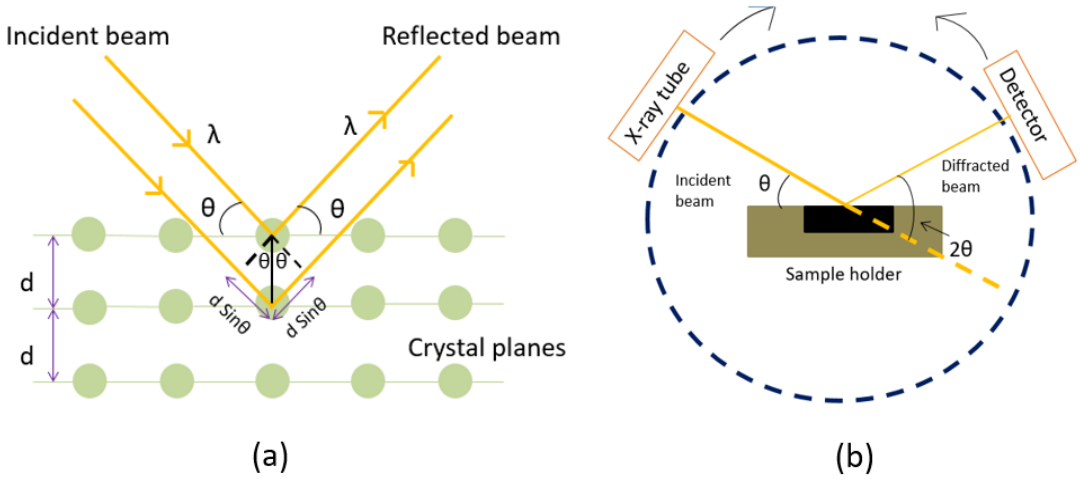

Figure 3.3: *(a) Bragg conditions for X-ray diffraction from atomic planes in the crystal. The incident waves are reflected by the crystal planes. The diffracted waves will be in phase when the Bragg's Law, $n\lambda = 2d \sin\theta$ is satisfied. (b) Schematic of x-ray diffraction (XRD) set up. Its basic components are x-ray source, a sample stage and a detector.*

incident on the sample at an angle θ and reflected x-rays are detected by a movable detector at angle 2θ. To measure at specular condition, the detector moves double the angle the sample moves. Measurements were carried out by varying the angle of incidence and the corresponding intensities of the diffracted peaks produce a diffraction pattern.

3.5 Magnetometry

3.5.1 Vibrating sample magnetometer

A vibrating sample magnetometer (VSM) is a device used to measure the magnetic moment of magnetic thin films. It operates on Faraday's Law of Induction, which tells us that a change in magnetic flux will produce an induced electromotive force (EMF) in a coil and this electric field gives the information about the changing magnetic moment. The sample to be studied is kept in a magnetic field. If the sample is magnetic,

this magnetic field will magnetize the sample by aligning the magnetic domains, or the individual spins, with the field. The magnetic dipole moment of the sample will then create a magnetic field around the sample, called the magnetic stray field. As the sample is vibrated at a known frequency, this magnetic stray field changes as a function of time. This alternating magnetic field will then produce an electric current in the pick-up coils according to Faraday's Law of Induction. This current will be proportional to the moment of the sample.

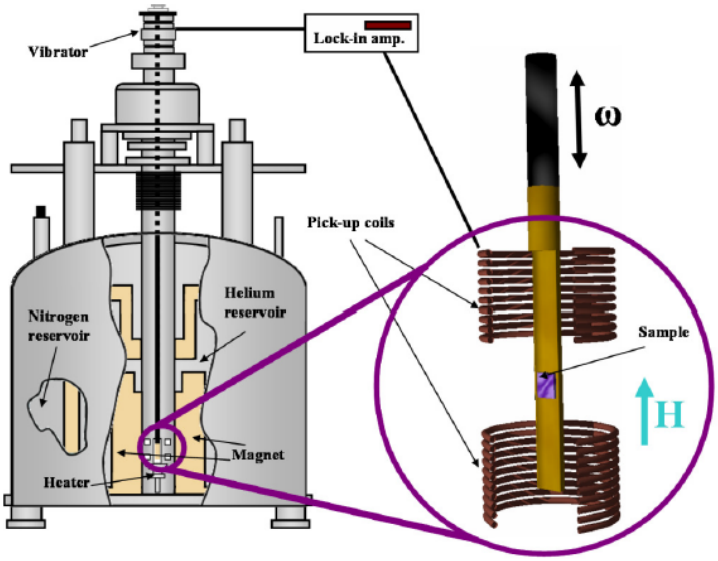

Figure 3.4: *Schematic of a vibrating sample magnetometer. Samples are vibrated in presence of an applied magnetic field. Induced voltage in the two coils is measured which are wound in opposite directions to reduce any background interference [116].*

Our Oxford Instruments Maglab VSM provides temperature control over a range of 1.5 K to 305 K. Figure 3.4 shows the schematic of a vibrating sample magnetometer. The sample is mounted on a Polyether etherketone (PEEK) paddle. This paddle is then attached to a carbon-fibre rod and inserted into a helium flow cryostat where the sample is held between two pick-up coils. This rod is placed in a variable temperature insert (VTI) surrounded by a liquid helium bath. The liquid helium is surrounded by a nitrogen reservoir and separated by a vacuum jacket. Temperature control is

maintained by the flow of liquid helium, fed into the VTI by a small helium inlet (needle valve) and a DC resistance heater located at the base of the VTI. The pressure inside the VTI is constantly maintained by a roughing pump. The sample is then vibrated in presence of an applied magnetic field which will magnetise the sample. Through the superconducting magnet surrounding the sample chamber we can apply a magnetic field up to 9 T parallel to the rod. The sample vibrates at 55 Hz as determined by the lock-in connected to a vibrator at the top of the VTI. As the sample vibrates, this results in a change in magnetic flux through the coils that induces an EMF. Current generated in the pick-up coils due to the change in flux at the driving frequency was amplified and interpreted by the lock-in amplifier.

Care must be taken for any background signal from substrates and the probe that can interfere with the small useful signal from thin magnetic films. We should prepare our samples in a clean environment to avoid surface contamination by magnetic impurities.

3.5.2 Superconducting quantum interference device

The superconducting quantum interference device (SQUID) is the most attractive magnetic sensor to measure very small magnetic moments with high sensitivity. It is based on quantum effects in superconducting loops. A Josephson junction is the heart of squid technology in which current flows between two superconductors separated by a thin insulator through quantum tunnelling. A Josephson junction is a small gap between two superconductors through which Cooper pairs can tunnel. A squid consists of a single (rf squid) or double (dc squid) Josephson junctions in a superconducting loop. Figure 3.5 shows the schematic of a Josephson junction.

In the Josephson equation, the supercurrent I_s passing through the junction is related to the relative phase difference δ across the junction and the critical current of the junction, I_0 as

$$I_s = I_0 \sin \delta, \quad \delta = \theta_1 - \theta_2 \tag{3.6}$$

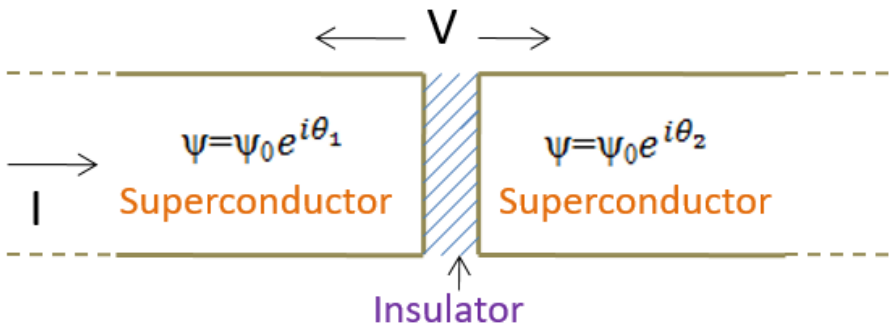

Figure 3.5: *Schematic of a Josephson junction. It consists of two superconductors separated by a thin insulator through which cooper pairs can tunnel and leads to the flow of supercurrent.* Ψ *is the wavefunction of the superconducting state in the left and right superconductors, and* θ_1 *and* θ_2 *are the phases.*

where δ is the difference between the phases θ_1 and θ_2 of the two superconductors.

In this research, Quantum Design SQUID-VSM MPMS3 detection system (figure 3.6) has been used to investigate the magnetic properties of the samples. This system has a sensitivity of about 10^{-8} emu and can operate over wide temperature range 1.8 K to 1000 K with magnetic fields up to 7 T. It consists of a set of superconducting detection coils inductively coupled to the DC SQUID. The sample is mounted on the quartz sample holder which is then fixed to sample rods made of tapered carbon fibre tubes, with adapters on either end. The sample is vibrated at frequency ω by the measurement system about the centre of the detection coils, where the signal peaks as a function of sample position. The default vibration frequency is 14 Hz and the default vibration amplitude is 2 mm. As the magnetized sample vibrates through the coils, a change in flux is produced in the detection coils. A change in magnetic field at the detection coil induces a change in field at the input coil. This input coil is magnetically coupled to the primary coil of the DC SQUID and it detects a change in magnetic flux.

DC squid consists of two Josephson junctions in parallel in a superconducting loop. In the absence of any external magnetic field, the input current I is split equally through the two junctions. When a small external magnetic filed is applied, a screening current I_s starts circulating in the superconducting loop and generates a magnetic field which

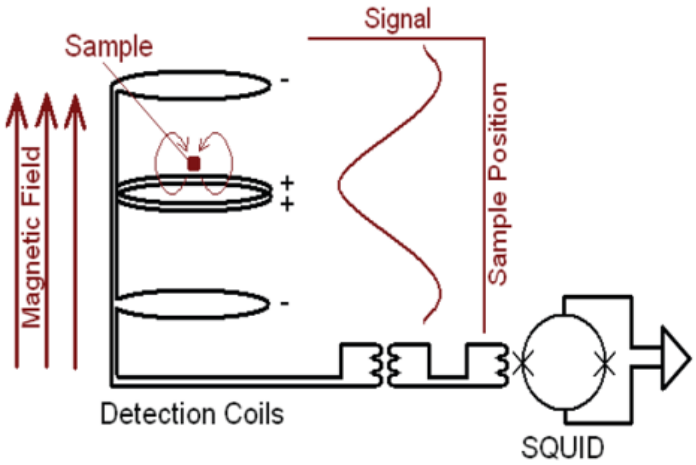

Figure 3.6: *Schematic of SQUID VSM MPMS3 detection system [117]. In this system, superconducting detection coil is coupled to an input coil of an inductor which in turn is inductively coupled to the DC SQUID.*

is equal but opposite to the applied field, that cancels the applied net flux. Now the current I_s is in the same direction as I in one of the branches of the superconducting loop, and is opposite to I in the other branch; the total current becomes I/2 + I_s in one branch and in the other I/2 - I_s. As soon as the current in either branch exceeds the critical current of the junction, a voltage appears across the junction. Now as we increase the magnetic flux ϕ, the screening current increases and when the magnetic flux reaches half a quantum ϕ_0 (ϕ_0 = h/2e is the flux quantum), the junctions become momentarily resistive with total current through the SQUID being zero (theoretically). At half of flux quantum, the screening current changes sign and at one flux quantum, it becomes zero and the total current is increased back to its maximum value. The screening current is periodic with a period equal to ϕ_0. The expression for the total current is given by

$$I_{tot} = 2I_0 \mid cos(\frac{\pi\phi}{\phi_0}) \mid \tag{3.7}$$

This variation of the current in the detection coils corresponds to the change in magnetic flux and produces an output voltage V across the junction which is thus a function

of the applied magnetic flux and the period equal to ϕ_0. SQUID feedback circuit cancels the current in the detection coils except the induced current due to a change in flux in them [118, 119]. The SQUID voltage is then amplified and digitized by the instrument electronics. To obtain high sensitivity it is necessary to have high magnetic coupling efficiency between the input coil and the primary coil of the SQUID.

3.6 Atomic force microscopy

Atomic force microscopy (AFM) gives the scientific community the ability to image with lateral resolution of the order of tens of nanometre and vertical resolution up to 0.1 nm. AFM was invented by Gerd Binnig and the first experimental investigation was made in 1986 [120]. The key part of atomic force microscopy is the measurement of interaction (force) between the end of tip of an AFM cantilever and the sample surface. During oscillation, the forces are of two main types: van der Waals and short range repulsive (contact) forces [121–123]. In some cases, there are other forces such as adhesion and capillary forces. In our case, AFM was operated in tapping mode, so it prevents the surface damage of the sample. In tapping mode, the cantilever tip is forced to oscillate at or near its resonance frequency ω_0 by a driving force of amplitude F_0 as the tip scans the surface of the sample. This is done by placing the cantilever in contact with a piezoelectric crystal to which an oscillating voltage is applied. The motion of the cantilever tip can be described by the non-linear second order differential equation given by

$$m\frac{d^2z}{dt^2} + kz + \frac{m\omega_0}{Q}\frac{dz}{dt} = F_{ts} + F_0\cos(\omega t) \tag{3.8}$$

Q, ω and k are the quality factor, angular frequency of the driving force and force constant of the free cantilever, respectively. Here, z represents the transverse displacement of the cantilever. F_{ts} represents the tip-surface interaction forces. In absence of these forces, this equation (3.8) describes the motion of a forced harmonic oscillator with damping. The solution of this equation consists of a transient term and a steady solu-

tion. Intially, both motions are dominant but after a certain time ($2Q/\omega_0$), the transient term will reduce by a factor of 1/e and from then the motion is dominated only by the steady solution. The steady state solution of this equation is a sinusoidal function given by

$$z(z_c, t) = z_0(z_c) + A(z_0)\cos(\omega t - \phi(z_c)) \tag{3.9}$$

where z_0, A and ϕ are the mean deflection, amplitude and phase shift of the oscillation, and z_c is the distance between the tip and sample surface [121, 122].

As the tip scans the sample surface, the vibration amplitude as well as the phase difference between the cantilever response and the excitation changes. The oscillating signal is measured by the photodetector. In general, in order to optimise the sensitivity of the amplitude measurement, we choose to work at a slightly lower frequency than the resonance. In order to produce an image of the sample surface, the tip must be scanned over the area of interest, and, point by point, the interaction of the tip with the surface is measured. For this, three piezoelectric crystals are used to move the tip in a controlled manner above the surface; two control the (x, y) movement of the tip over the sample and the third (z) precisely controls the tip-sample distance. Tapping mode tips have high spring constants ($\sim$50 N/m), short cantilevers (125 μm) and high resonance frequencies ($\sim$300 kHz).

During tapping mode operation, a feedback loop is necessary to maintain a constant cantilever oscillation amplitude. Figure 3.7a shows the schematic of atomic force microscopy set up with AFM electronics. A laser beam is reflected by the backside of the cantilever and the reflected intensity is measured by a four quadrant photodetector (figure 3.7b). As the tip approaches or retracts from the surface, the signal changes because the interaction between tip and surface changes the resonance frequency of the tip of the cantilever. In the tapping mode, the high frequency voltage applied to the excitation piezo is also the reference signal for the lock-in amplifier which is used to obtain the amplitude signal from the photodetector data. The measured signal is then compared via the feedback loop with the Setpoint value (a voltage) chosen by the

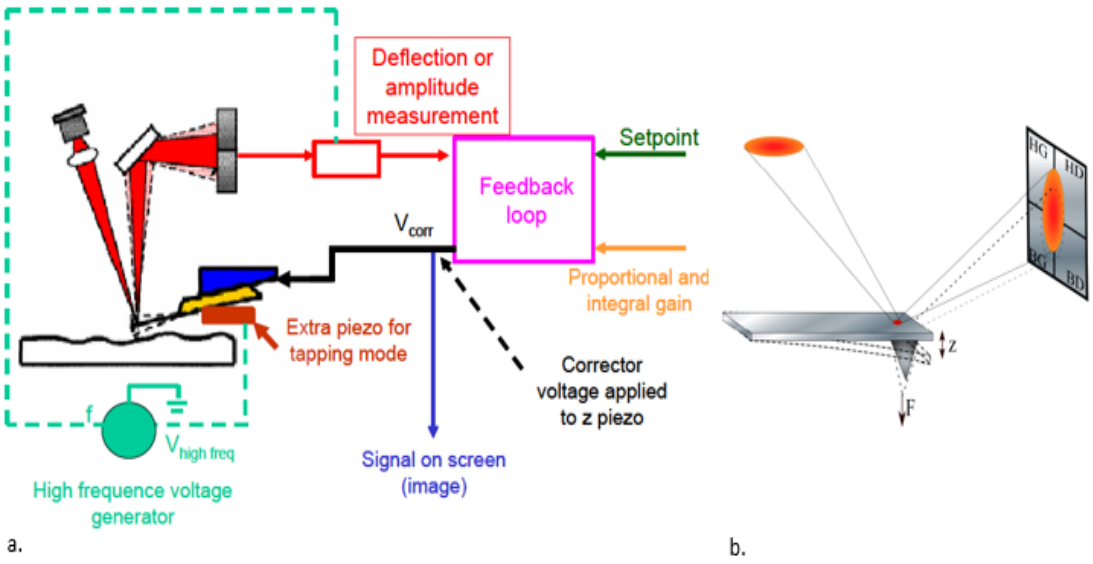

Figure 3.7: *(a) Schematical set up of an Atomic force microscopy (AFM). It operates in tapping mode in air. A cantilever tip scans over the surface of a sample. A feedback loop controls the distance between tip and sample, which is evaluated by a computer and results in a topographical image of the sample (b) A laser beam is reflected by the backside of the cantilever and the reflected intensity is measured by a four quadrant photodetector.*

operator. In tapping mode, the Setpoint is the percentage of the free amplitude. If the measured and Setpoint values are equal, the feedback loop does nothing. If, however, the measured and Setpoint values differ, the feedback loop sends a signal V_{corr} to the z piezo so that the tip either approaches or is retracted as necessary so that the measured amplitude then equals the Setpoint value. It is this signal V_{corr}, calibrated in nm, which gives us quantitative information which is used to extract the root mean square (RMS) roughness as a measure of the surface roughness in the resulting image of the sample surface on the computer screen. The proportional and integral gains need to be optimized so that the feedback loop responds quickly without adding too much noise to the data. The raw AFM image was analysed by Nanoscope analysis software. In our work, roughness of the YIG samples were analysed using AFM.

3.7 Polarised neutron reflectivity

Polarised neutron reflectivity (PNR) is a layer selective technique based on the magnetic interactions between the neutron magnetic moment and the magnetisation of the medium. This gives us the magnetisation profile of the film and structural information such as film thickness and interface roughness. It is a unique technique which gives quantitative information about the magnetic moment of the sample in the monolayer range. In a polarised neutron reflectivity experiment, the magnetisation of the film is saturated along the direction of the neutron spin and we measure the reflectivity for the two neutron spin states. The neutron reflection amplitude is sensitive to the surface roughness, from this we can estimate the interface roughness of the film, within the range 0-50 Å [124]. Also, from the fringe spectra obtained due to the multiple interference of the neutron beam within the sample layers, we can obtain the thickness of each layer of the film.

A neutron can be represented as a plane wave of wave vector $\boldsymbol{k}$ in three dimensions as

$$\psi(\boldsymbol{k}, \boldsymbol{r}) = e^{i\boldsymbol{k}.\boldsymbol{r}} \tag{3.10}$$

where $\boldsymbol{r}$ is the position vector of neutron in space.

In matter the neutron interacts through a neutron potential and a magnetic potential which affect the magnitude of **k**. The strength of these potentials are characterised by scalar coherent scattering lengths. The propagation of single neutron plane wave can be represented by a time-independent Schrodinger equation:

$$\left[\frac{-\hbar^2}{2m} \bigtriangledown^2 + V(\boldsymbol{r})\right] \psi = E\psi \tag{3.11}$$

where $V(\boldsymbol{r})$ accounts for the potential energy of the neutron, m is the neutron mass and E represents the total energy of the neutron.

Now, in a continuous medium with density N, consisting of a single isotope of a

given element, the potential energy is given by [125]

$$V = \frac{2\pi\hbar^2}{m} Nb = \frac{2\pi\hbar^2}{m}\rho \tag{3.12}$$

where b is the coherent scattering length and $\rho = Nb$ is the scattering length density (SLD).

In specular condition of reflection, the neutron incident on the surface of the sample at an angle θ and the reflected at an angle θ. The scattering geometry of reflectometry experiment is shown in figure 3.8. The interfaces of the sample are perpendicular to the scattering vector **q**, where **q** is given by

$$|\mathbf{q}| = |\mathbf{k}_f - \mathbf{k}_i| = \frac{4\pi}{\lambda}\sin\theta \tag{3.13}$$

where λ is the neutron wavelength, $\mathbf{k}_i$ and $\mathbf{k}_f$ are the incoming and outgoing neutron wave vectors.

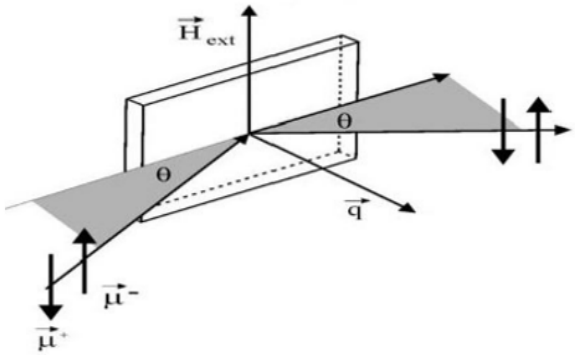

Figure 3.8: *Scattering geometry of the neutron reflectometry experiment with the neutron scattering angle θ, scattering vector **q**, external magnetic field H_{ext} and the magnetic moment for spin-up neutrons (μ^+) and spin-down neutrons (μ^-) [126].*

The neutron spins oriented either parallel or antiparallel to the external field which is in the plane of the magnetic film. The magnetic moment of the neutron, μ is associated with the intrinsic spin angular momentum and corresponds to two discrete energy states in a given magnetic field **B**. The energies corresponding to these states are

$$E_{\pm,magnetic} = \mp\mu|\mathbf{B}| \tag{3.14}$$

where the plus (minus) sign denotes the direction of spin parallel (anti-parallel) to the magnetic induction. For a grazing incidence the interaction with the film can be described with an effective potential given by the sum of a nuclear and a magnetic component, Zeeman interaction. This potential is given by

$$V = \frac{2\pi\hbar^2}{m} N b^{nuc} - \vec{\mu}.\mathbf{B} = \frac{2\pi\hbar^2}{m}(\rho_n \pm \rho_m) \tag{3.15}$$

where N and b^{nuc} denote the atomic density and coherent nuclear scattering length. The quantity, ρ_n = Nb^{nuc} is the nuclear scattering length density whereas the magnetic contribution to the potential is expressed in terms of magnetic SLD, ρ_m = Nb^{mag}. The first term represents the interaction of the neutron with the nucleus and the second term signifies the interaction of neutron with the magnetic field. So, the potential V^+ and V^- for spin up and spin down neutrons can be expressed as follows [126]:

$$V^{\pm} = \frac{2\pi\hbar^2}{m}(N b^{nuc} \pm N b^{mag}) \tag{3.16}$$

As the nuclear and magnetic SLD are of same order of magnitude, PNR is very sensitive to magnetic structures. The reflectivity of the sample can be derived by solving the Schrodinger equation (3.11) using the potential mentioned above. The spin-up and spin-down reflectivities R^+ and R^- can be expressed as

$$R^{\pm} = \frac{q - \sqrt{q^2 - 16\pi(\rho_n \pm \rho_m)}}{q + \sqrt{q^2 - 16\pi(\rho_n \pm \rho_m)}} \tag{3.17}$$

The reflectivity R = 1 upto a critical edge q_c =$\sqrt{16\pi(\rho_n \pm \rho_m)}$, which is of the order of 0.01 Å^{-1} for most of the materials. Beyond this point, the reflectivity decays rapidly with a mean asymptotic q_z^{-4} dependence [127].

For polarised neutron reflectivity, we define spin asymmetry SA as

$$SA = \frac{(R^+ - R^-)}{(R^+ + R^-)} \tag{3.18}$$

where R^+ and R^- are the spin up and spin down reflectivities. SA gives a measure of the difference in the reflectivity due to the spin dependent magnetic interaction.

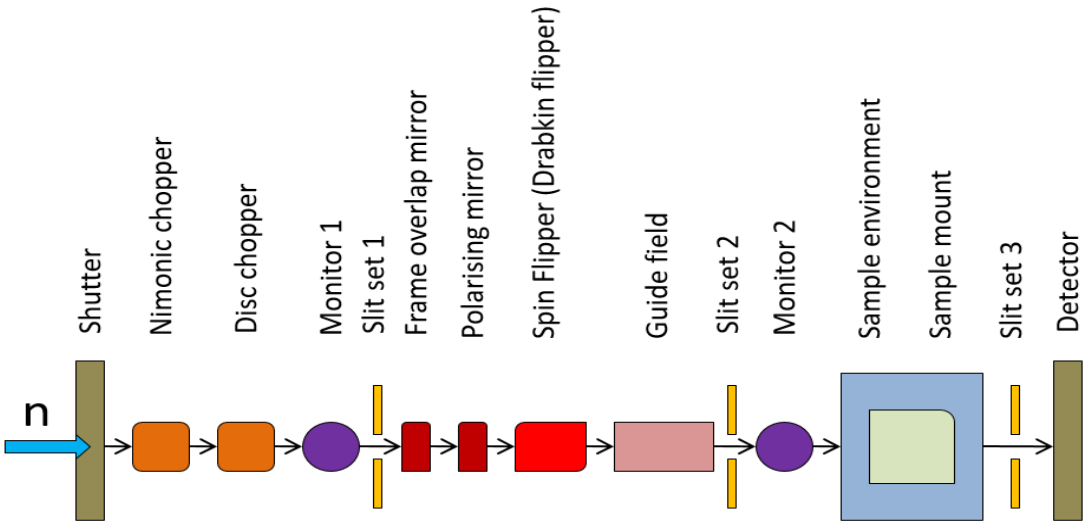

Figure 3.9: *Schematics of the polarised neutron reflectometry experiment polREF at ISIS neutron source at Rutherford Appleton Laboratory (RAL), Oxford [128].*

Now, we will discuss the experimental setup of PNR measurements polREF at ISIS neutron source at Rutherford Appleton Laboratory (RAL), Oxford. The polREF is a polarised neutron reflectometer, uses polarised neutrons to study inter and intra-layer magnetic ordering in thin films and surfaces. An outline of polREF is shown in figure 3.9. A variable aperture disc chopper is used to obtain a wavelength band of 1-14 Å for polREF. The polREF beamline uses the neutrons which are produced via spallation of a target by high energy proton beam and have wide range of energies. The highest and lowest energy neutrons are removed using a nimonic chopper, which is basically a spinning disc with holes cut into it that rotates in phase with the proton beam pulse so as to pass only those neutrons that are travelling with a definite range of velocities. This range of neutron velocities is called a frame. After the chopper, the passage of neutrons is monitored by a beam monitor. Additional frame overlap suppression is done by the frame overlap mirror, which further removes the long wavelength neutrons. A polarising supermirror is used to get high polarisation, high reflectivity and high transmission neutron beam. This set of polarising mirror followed by a spin flipper and a static guide field provide a particular polarisation of neutrons at the sample

position. The flipping elements are characterised by high flipping efficiency over the entire wavelength range and the beam size. The detected neutron beam is then normalised by a second monitor placed before the sample. The beam is collimated by a slit and directed towards the sample, that sits between the coils of an electromagnet. The sample is mounted in a high precision sample stage. The reflected neutrons are passed through a second set of slits and finally detected by a 3He single detector. Requirements for magnetic field are achieved through bipolar electromagnet (for small fields upto 1.5 T) and superconducting magnet (for high fields upto 10 T). Temperature down to 2 K is achieved with the use of continuous flow cryostat. The average size of the sample used is roughly 20 x 20 mm^2 to get a decent count rate within reasonable q range.

3.8 Ferromagnetic resonance technique

The magnetization dynamics of YIG thin films are investigated by the microwave technique, called ferromagnetic resonance (FMR). The FMR technique has been widely used for the high frequency characterisation of magnetic thin films. We can use the FMR to study the magneto static properties, for example, anisotropies [129, 130], exchange coupling [131–133], and also the spin dynamics; damping constant [134, 135], g factor [135, 136], etc. The precession frequency of a ferromagnet lies at the microwave region, ranged from 0.1 to 100 GHz. Main principle of the FMR technique is to apply a torque on the magnetic moment by applying a rf transverse magnetic field pulse h_{rf} which results in the precessional motion of magnetisation M about the direction of an external magnetic field. The magnetisation follows a helical trajectory due to energy dissipation and this behaviour can be described by the LLG equation 2.7, in section 2.3.1 . In VNA-FMR technique, using a Vector network analyser an electromagnetic wave can be sent to the sample. The incident wave will be reflected and/or transmitted after interacting with the sample (Fig.3.10a). By analysing the reflectance/transmittance,which is the ratio of reflected, transmitted power to that of

incident, we can find the scattering parameters (S_{11}, S_{22}, S_{12}, S_{21}), from which we can extract the properties of the sample. Figure 3.10b shows a two-port device under

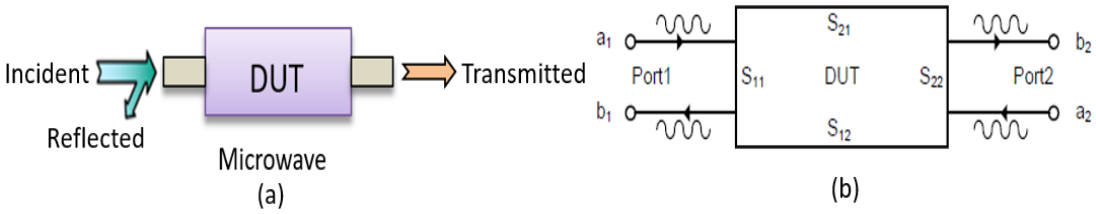

Figure 3.10: *(a) The incident wave will be reflected and/or transmitted after entering the device under test (DUT) (b) Two-port device S-parameters model [137].*

test (DUT) along with the corresponding four S-parameters. For a two port device the S-parameters equations can be written as

$$b_1 = S_{11}a_1 + S_{12}a_2 \tag{3.19}$$

$$b_2 = S_{21}a_1 + S_{22}a_2 \tag{3.20}$$

where S_{11} and S_{22} are the reflection coefficients at the port 1 and port 2 respectively, whereas S_{12} and S_{21} represent the transmission coefficients. So, a microwave leaving the device under test (DUT) (b_1 or b_2) is a linear combination of the waves incident on the DUT (a_1 or a_2). Terminating the DUT with the characteristic impedance Z_0 = 50 Ω allows the extraction of the individual S-parameters. At port 2, if a 50 Ω termination is present, a_2 becomes zero, resulting in S_{11} and S_{21}. We can apply the same principle in the reverse direction to get S_{22} and S_{12} by setting a_1 to zero, as shown in equation 3.21 and 3.22.

$$S_{11} = \left.\frac{b_1}{a_1}\right|_{a_2=0} \qquad S_{12} = \left.\frac{b_1}{a_2}\right|_{a_1=0} \tag{3.21}$$

$$S_{21} = \left.\frac{b_2}{a_1}\right|_{a_2=0} \qquad S_{22} = \left.\frac{b_2}{a_2}\right|_{a_1=0} \tag{3.22}$$

For the FMR measurements, we can sweep the microwave excitation frequency at a fixed bias field or at fixed excitation frequency the static external field can be swept

to achieve the resonance condition. The experimental setup is shown in figure 3.11, where vector network analyser serves as the source and detector of the signal which is guided by the probes. It compares the incoming to the outgoing signals with respect to their amplitude and phase so as to measure the absorption of the sample as a function of frequency. The magnetic sample is mounted on the top of the signal lines of a coplanar waveguide (CPW) and the microwave is conducted into coplanar waveguide. The sample is swept through the resonance condition by means of an external field. The measured FMR signal is proportional to the field derivative of the imaginary part of the ac susceptibility.

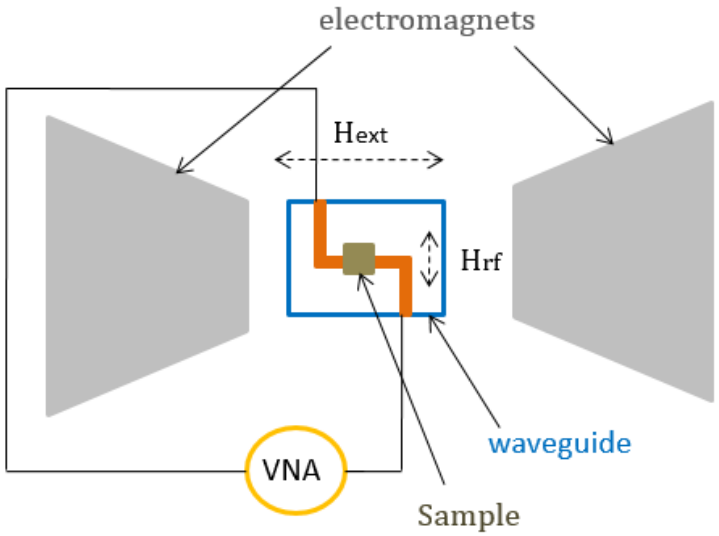

Figure 3.11: *Schematic of FMR technique using Vector network analyser. A 50 Ω impedance matched waveguide is placed at the centre of DC magnetic field H_{ext} and a microwave field h_{rf} is applied transverse to the DC field. The sample is placed with film-side down on top of the waveguide.*

We can also use a lock-in amplifier detection technique for our FMR measurements. Figure 3.12 shows the block diagram of experimental set up of FMR using lock-in amplifier. Here the thin sample is mounted with film-side down onto the top of the CPW, placed in the centre of the electromagnet that provides the dc bias field. The electromagnet has a gap of about 5 cm and a maximum field of 300 mT at 10 A

current can be applied, controlled by KEPCO power supply. The rf microwave source is a broadband microwave generator with maximum power 25 dBm. Large power excitation will drive the magnetization precession in non-linear region. Also the signal will be reduced and broadened. So, in order to determine the lineshapes and width precisely, it is better to use low power to avoid the non-linear region. The signal intensity is proportional to the squre root of power, $V_s \propto \sqrt{P}$ [138]. In our measurements, the microwave frequency is kept constant and the static external magnetic field is swept to obtain the resonance field. The coplanar waveguide system operates in pulse modulation mode. For this, reference pulse signal port of the microwave generator is connected to the low frequency output port of the lock in amplifier so as to keep the reference signal frequency at 73 Hz. At this frequency, we obtained a good signal to noise ratio. The signal generator sends the microwave current to the sample mounted on a waveguide and the transmitted rf FMR signals from the magnetic sample are detected by means of a schottky diode, the output of which is sent to the lock in amplifier. The schottky diode acts as a microwave transducer, i.e. a microwave power is transduced into the voltage. The lock in amplifier then multiplies the diode voltage with the reference signal pulse modulated at 73 Hz and integrates the result over a certain time to give the output voltage. This lock-in technique is useful to enhance the signal to noise ratio.

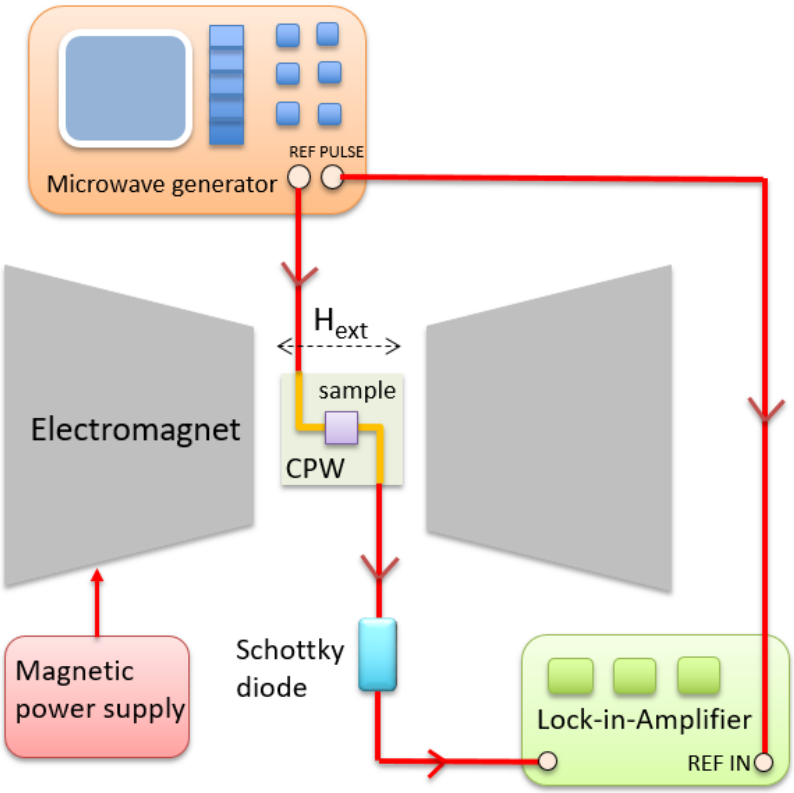

Figure 3.12: *Schematic of lock-in amplifier detection technique for FMR measurements. The sample is mounted on the CPW which is placed at the centre of the electromagnet. The microwave generator sends the microwave current to the magnetic sample and the transmitted signals from the sample are detected using a schottky diode and the output is finally sent to the lock-in amplifier.*

CHAPTER 4

Structural and morphological properties of nm-thick YIG films

4.1 Introduction

Yttrium Iron Garnet (YIG) films were a subject of intensive research since the past ten years. Previously in 1970s, bulk YIG crystals and micrometer thick films grown by liquid phase epitaxy (LPE) have been widely used for the implementation of microwave devices [139]. In recent years, YIG proved to be an excellent material in the emerging field of magnonics [21, 140–142] and spin caloritronics [[37, 38, 143]. However, integration of YIG based spintronic devices requires thin films with high structural quality to ensure good magnetic and dynamic properties, and in particular to develop efficient YIG-based magnetic heterostructures for information transfer. All of the growth techniques for YIG involve the use of high temperatures (>700° C) either during the growth, in-*situ* annealing or in post-growth annealing which can cause significant changes in the structural characteristics. To our knowledge, up to now no detailed studies have been carried out on the effect of high temperature annealing on the YIG/GGG interface despite the fact that YIG-GGG combination has been used widely in the spintronics community [38, 144–147]. In this chapter, we are interested in the structural properties of YIG where small changes at the interface can have significant effects on the fundamental properties of YIG. Our nm-thick single crystal YIG films were deposited on (111) oriented 0.5 mm thick GGG substrates by RF magnetron sputtering followed by high temperature annealing at 850°C in air. Annealed YIG samples are transparent with a pale yellow colour. The as-deposited films on the substrates are amorphous and non magnetic. The crystallinity of the film and the smooth surface are achieved after their annealing.

The structural quality, lattice parameter, thickness, and surface roughness of the YIG films were analyzed using x-ray diffraction (XRD), x-ray reflectivity (XRR) and atomic force microscopy (AFM). For this study, a series of thin YIG films with different thicknesses ranging from 8 nm to 250 nm were deposited under the same deposition condition on the GGG substrate. The film-substrate interface is strongly influenced by the annealing conditions which can affect the structural and compositional behaviour of the films. To understand the influence of annealing at the film-substrate interface we

carried out an atomic-scale investigation of the YIG/GGG interface using aberration-corrected scanning transmission electron microscopy (STEM).

4.2 Structural properties

4.2.1 X-ray reflectivity

In this section, the structural properties of thin YIG films were studied by x-ray reflectivity. This allows us to find the thickness of the film, growth rate of the material, surface and interface roughness and the density.

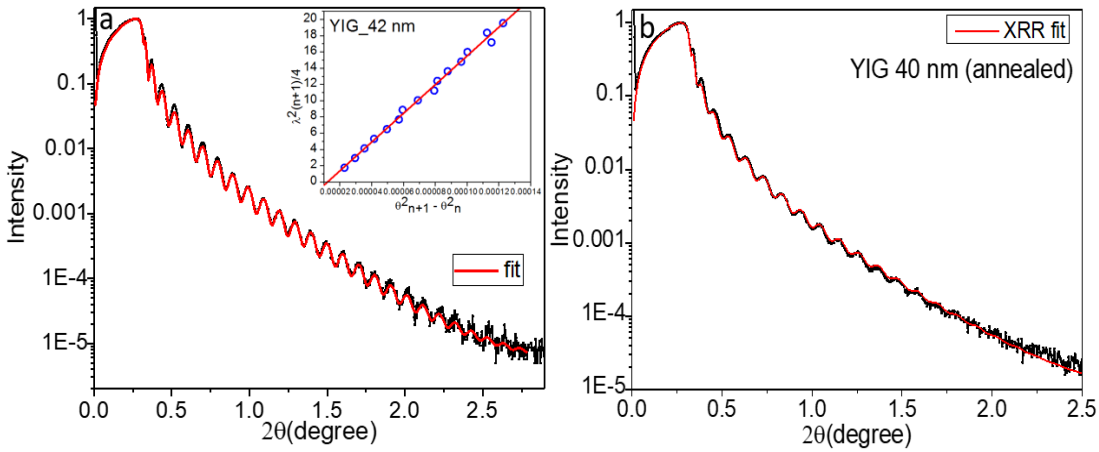

Figure 4.1: *X-ray reflectivity (Cu $K_\alpha, \lambda = 1.54$ Å radiation) of a typical YIG film before annealing (a) and after annealing (b). The points are the measured data and the line is a best fit whose parameters are cited in the Table 4.1. A very good fit is obtained for the unnealed sample with a single layer of YIG. However, for the annealed sample a good fit could only be obtained by incorporating an interface region instead of a sharp GGG/YIG interface.*

Figure 4.1 (a) shows the low angle x-ray reflectivity (Cu $K_\alpha, \lambda = 1.54$ Å radiation) of an unnealed 42 nm YIG film, whose thickness was determined from the angular positions of the Kiessig fringes (inset of figure 4.1a) by using equation 3.4 (section 3.4.1). The reflectivity is measured at grazing incidence including the straight-through beam such that the region below $\sim 0.4^\circ$ is due to the beam footprint. This is followed

by a sharp decrease in the intensity at the critical angle. We measured the thickness of the films before (42 nm) and after annealing (40 nm). After annealing the thickness of the films decreases by a very small amount. The slow exponential decay of the reflectivity curve indicates a smooth surface of the annealed film.

The reflectivity curves are fitted using the software Bede to get further information about the chemical nature of the YIG/GGG interface and also the density. An example of the X-ray reflectivity (XRR) curve with its fitting is shown in figure 4.1 (a) and (b) for a typical YIG sample before (42 nm) and after annealing (40 nm), respectively. The points are the measured data and the red solid line is a best fit to the reflectivity curve. The parameters obtained from the fitting in each case are cited in the table 4.1. For the unnealed sample, the densities of the YIG and substrate are about 96 % of the bulk. For the annealed sample, the total thickness of the film is reduced but the interesting point is that in order to obtain the best fit for the x-ray data, we have to include an additional layer at the interface (figure 5.14). This gives us an indication that there may be diffusion at the interface. Although, we obtained a good fit using only a YIG layer with the goodness of fit (GOF = 0.05), but the density obtained from the fit for the GGG was only 91% that of bulk GGG. A much better fit is obtained by using a trilayer system of GGG/$\sim$ 50-60 Å of Gd-rich layer/YIG where the interface layer has a density that is reduced by about 13%.

With the help of additional structural information from the TEM results (section 4.5.1), we model this interfacial region as a mixed layer of YIG and Gd (YIG1 and Gd in Table 4.1). This shows that we are not relying on a specific crystal structure of the compound GdIG to explain the results. Because this diffused layer will not be stoichiometrically perfect. So, the interface layer is modelled by allowing its total thickness to reach that of the dead layer (6 nm) and by incorporating significant roughness and grading in the layer. In this fit, the roughness is modelled as a Gaussian with the full width at half maximum representing the standard deviation of an effective roughness. Here, the grading is representing the interdiffusion and the roughness is produced by terraces or steps, for example. However, it is difficult to distinguish

Unnealed				
Layer	**Thickness (Å)**	**Density** (%)	**Roughness(Å)**	**Grading(Å)**
YIG	422	96.4	4.6	-
GGG	∞	96.9	6.0	-
Annealed				
YIG	347	99.3	4.3	0.0
YIG1	29	93.2	14	2.3
Gd	18	89.1	7	19
GGG	∞	99.9	8.8	0.0

Table 4.1: *Parameters used in fitting the x-ray reflectivity data for unnealed (42 nm) and annealed YIG (40 nm) films, shown in figure 4.1. The densities are expressed as a per cent of the bulk layer.*

between a chemically graded interface and physical roughness [113] since we are only in the specular regime. Nevertheless, the parameters we obtained from the fit for this layer are as expected - roughness and grading that is nearly equal to the thickness of the layer and have much reduced densities. In this way, we can represent a disordered interface layer. The roughness of the YIG surface are reasonable. We know that in XRR measurement the x-rays illuminate the entire sample, so the YIG surface roughness 4 Å obtained from the fit agrees quite well with the RMS roughness (1-3 Å) of the atomic force microscopy results. The total thickness of the interface region (YIG1 and Gd) varies from 5 - 6 nm between samples. The GOF of the fit for the annealed sample is 0.04 and importantly, the densities for the YIG and GGG are within 1% of the bulk values which indicates that the top layer is stoichiometrically correct.

4.2.2 Crystallinity : X-ray diffraction

For a deeper insight into the structural quality of the film, we performed XRD measurements. We determined the crystalline orientation and the lattice parameter of YIG.

We first started with the results of 2θ-ω scan of a (111) - oriented GGG substrate with and without the monochromator, as shown in figure 4.2 (a) and (b) respectively. Without the monochromator we can see two peaks of GGG corresponding to Cu $K_{\alpha 1}$ and Cu $K_{\alpha 2}$ radiation. With the use of monochromator, a single crystalline (444) peak is observed at $2\theta = 51.03°$ which corresponds to the lattice constant of 12.383 Å.

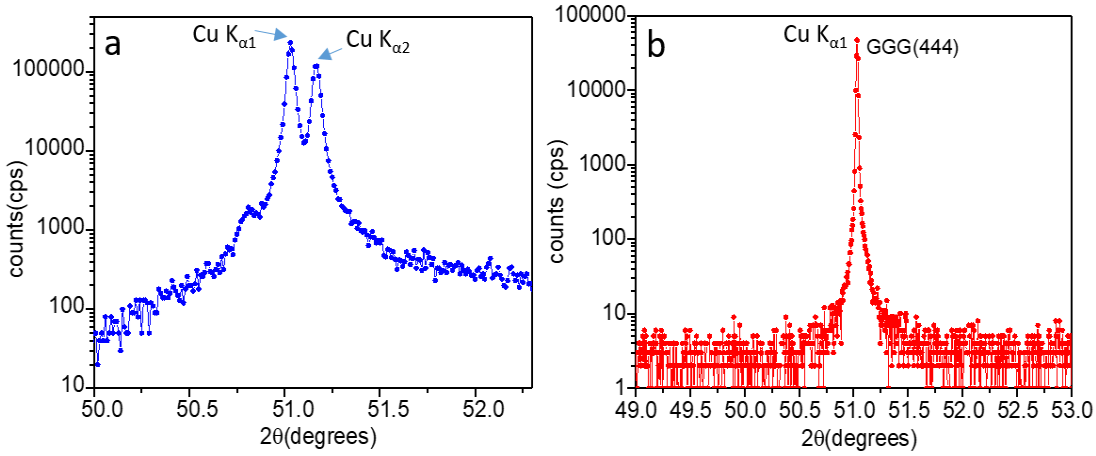

Figure 4.2: *(a) X-ray diffraction for a GGG substrate without the monochromator showing two peaks of GGG. (b) XRD spectra with monochromator showing a single crystalline (444) peak of the substrate with a lattice constant of 12.383 Å.*

Figure 4.3 shows the XRD scan of a YIG sample without the monochromator, where the YIG (444) peak has two clearly resolved $K_{\alpha 1}$ and $K_{\alpha 2}$ lines. The use of monochromator allows easier identification of peaks with Cu $K_{\alpha 1}$ wavelength only. A monochromator was installed to filter out the Cu $k_{\alpha 2}$ and to only observe the Cu $k_{\alpha 1}$. For all our XRD measurements, the monochromator was used for better investigation of the YIG peaks. For the unnealed YIG sample, only the substrate peak is visible because the as-deposited YIG samples are amorphous.

Figure 4.4 presents the X-ray diffraction (XRD) spectra for four samples of YIG with thicknesses 30, 50, 78 and 250 nm. For all these samples, the YIG (444) peak are observed at lower angle than the substrate peak. These data show the evolution of a peak with the sample thickness. With increase in sample thickness the intensity of

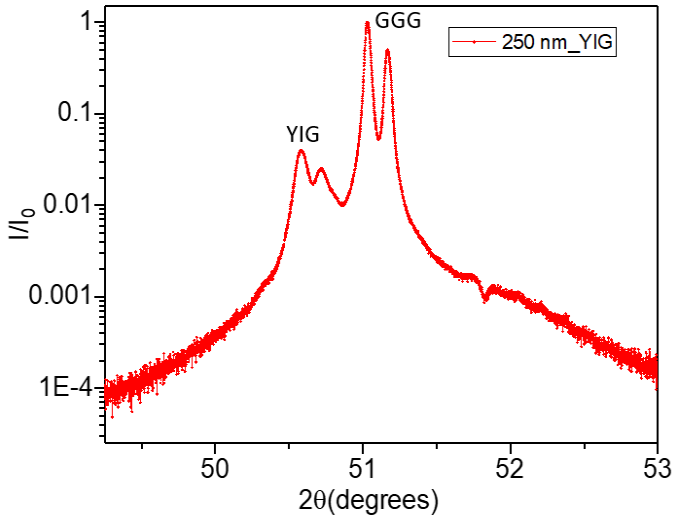

Figure 4.3: *X-ray diffraction for a 250 nm thick YIG film without the monochromator which shows the YIG (444) peaks corresponding to both Cu $K_{\alpha 1}$ and Cu $K_{\alpha 2}$ radiation.*

YIG (444) peak increases. This is because as the thickness increases we are adding more atomic planes and we will have more constructive interference. The XRD peak with the highest intensity is observed at 2θ = 50.57° for the thicker film of 250 nm. Figure 4.5 shows the XRD rocking curve of 250 nm YIG film which exhibit a FWHM of 0.0072 $\pm$ 0.0001 degrees confirming the high crystalline quality. For thinner films below 30 nm, it was difficult to distinguish between the YIG peak and substrate peak. The lattice constant is calculated from the Gaussian fit of the YIG peak for each sample. The lattice constant as a function of thickness is plotted in figure 4.6. Inset shows the gaussian fit of YIG peak for 250 nm thick film, giving lattice constant of 12.491 $\pm$ 0.002 Å. The lattice parameter of bulk YIG is 12.376 Å. This slight increase in lattice parameter might be due to the rhombohedral distortion in the YIG crystalline lattice [148]. This variation of the XRD spectra with respect to the film thickness tends to give an indication towards a critical thickness for strain relaxation. The variation of lattice constant with thickness is also reported in ref. [149] where the lattice constant of sputtered YIG varies from 12.427 Å to 12.390 Å for the thickness range 16 nm to 164 nm, respectively.

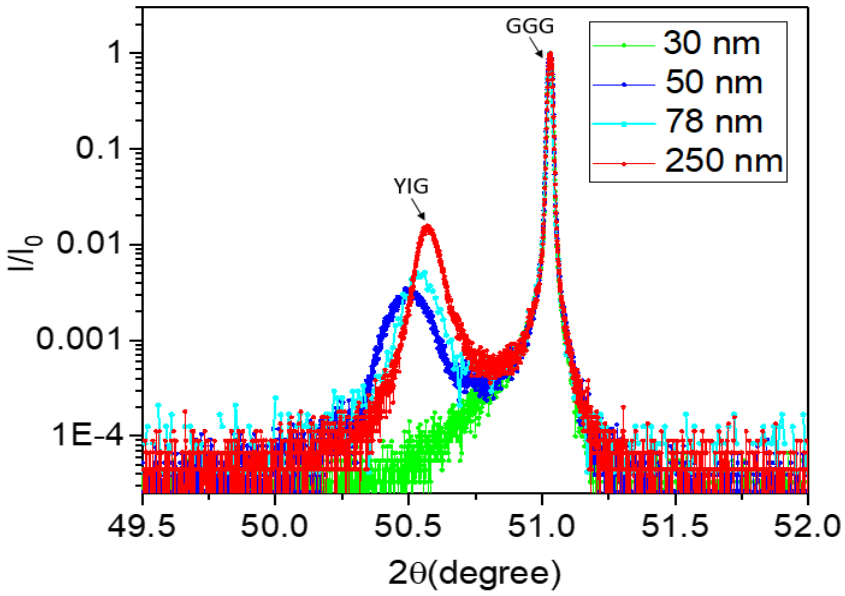

Figure 4.4: *The YIG has a (111) crystalline orientation and films develop a diffraction peak. Intensity of the peak varies as a function of thickness that corresponds to a lattice constant of 12.4905 ± 0.002 Å for 250 nm film compared to 12.376 Å for bulk YIG. For the thinnest films, the YIG peak is masked by the substrate peak. The peak at 51.03° corresponds to the GGG substrate with the out of plane lattice constant of 12.383 Å.*

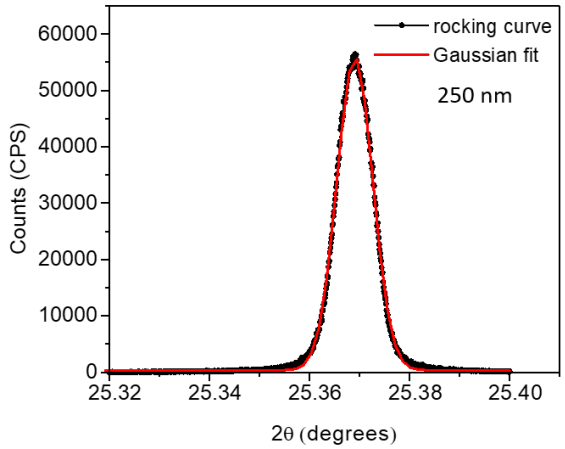

Figure 4.5: *XRD rocking curve of a 250 nm YIG film exhibiting FWHM of 0.0072 ± 0.0001 degrees showing the excellent crystalline quality of our YIG films.*

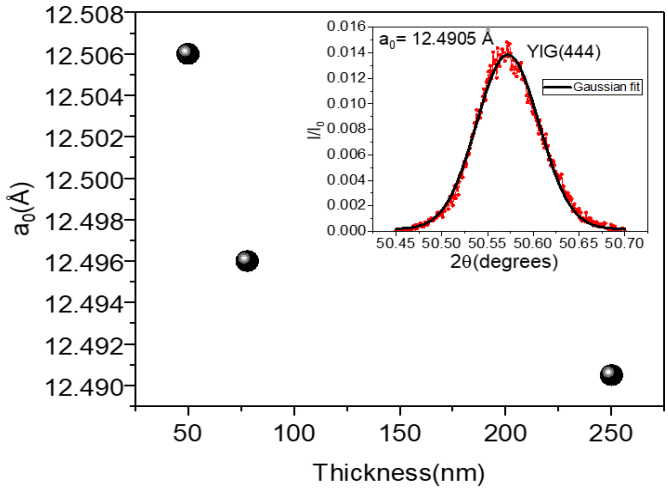

Figure 4.6: *The lattice constant (a_0) as a function of thickness of the YIG sample. Inset of the graph shows the fitting of the YIG (444) peak with the gaussian function.*

During the last year of my research work, we used a new target of YIG (Target-B) for the growth because with time we found that the samples grown from the old target have a high deposition rate and were showing poor quality with high magnetization (higher than bulk value). This is most possibly due to the use of the old target (Target-A) over a long period of time and most of the material was almost sputtered. We used the same deposition conditions to grow YIG from the Target-B, and the films were annealed immediately under the same conditions. But this time with the same growth parameters, we found the deposition rate of the material is about 0.16 Å/s. Figure 4.7 shows the high angle (2θ-ω) scans of three samples grown from Target-B: 125 nm, 66 nm and 42 nm, all of which exhibit distinct Laue oscillations in the vicinity of the GGG peak. These Laue oscillations observed in the high angle scan to the left and right of the substrate peak indicating the films are highly crystalline with (111)-oriented growth on the lattice matched GGG substrate, ordered and uniform. For these samples, the YIG peaks are at higher angle than the GGG substrate, which is in contrast to the one observed with Target-A samples. Inset of figure 4.8 shows the YIG peak which is fitted with gaussian function to obtain the peak position and hence to calculate the lattice constant using the Bragg's equation. The lattice spacing

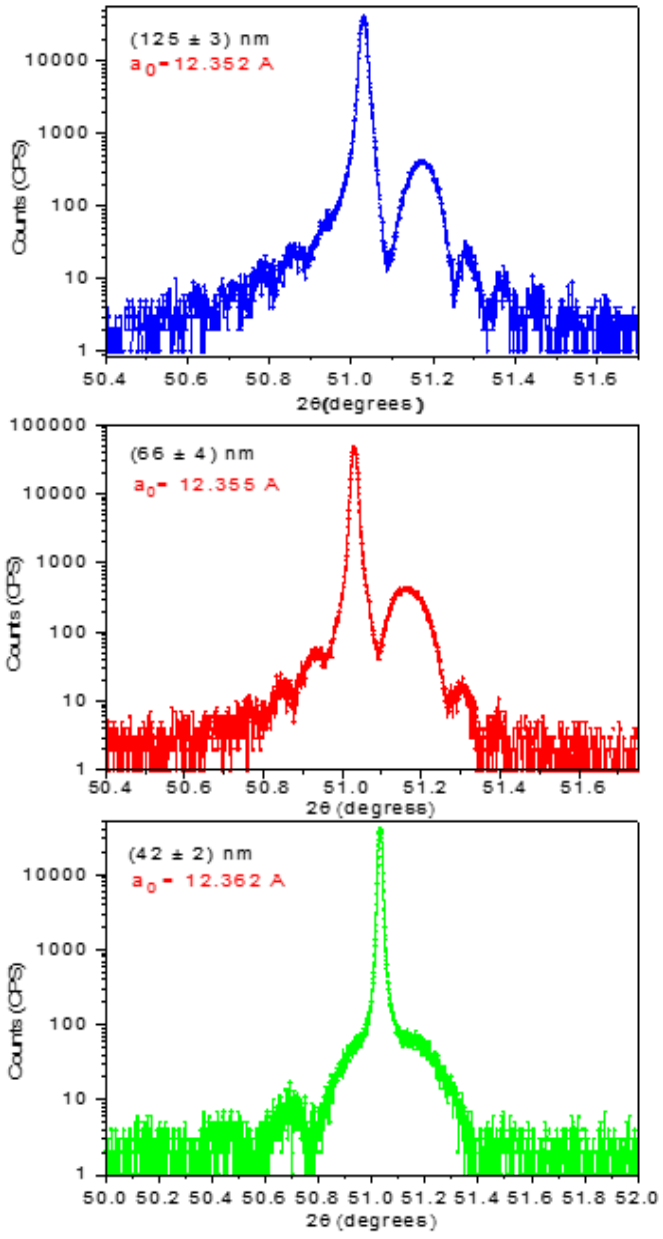

Figure 4.7: *High angle XRD scans of YIG films of thickness 125, 66 and 42 nm grown on the GGG substrate showing single crystalline YIG (444) peak, from which the lattice spacing of the YIG (444) planes is determined. All of the samples exhibit distinct Laue oscillations on either side of the substrate peak indicating the films are highly crystalline, ordered and uniform.*

between the adjacent YIG (444) planes is 7.132 Å, 7.133 Å, and 7.137 Å corresponds to YIG cubic lattice constants of 12.353 Å, 12.355 Å and 12.3617 Å for the 125, 66 and 42 nm films, respectively. In ref. [65], the YIG peaks have also appeared on the right side of the GGG peak. For our 42 nm thick YIG, the intenisty of YIG peak is very low and hence it was hard to distinguish from those of the substrate. Figure 4.8 shows the variation of lattice constant as a function of thickness. With decrease in film thickness, the lattice constant shows a slight increase. This thickness dependence of lattice constant was also observed for off-axis sputtered YIG films with thicknesses 10, 20, 50 and 80 nm [65]. From the comparison of our XRD spectra, we found that films grown at much slower rate from the Target-B shows Laue oscillation. Also, the lattice constant is more close to the bulk value of YIG which indicates minimal distortion or strain as compared to the films grown from the Target-A.

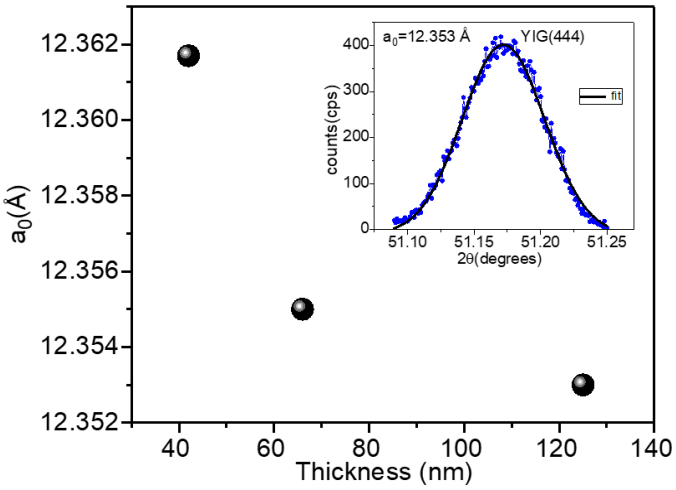

Figure 4.8: *The lattice constant (a_0) as a function of thickness of the YIG sample. Inset of the graph shows the fitting of the YIG (444) peak with the gaussian function used for the determination of the lattice constant of YIG.*

Altogether, we believe that we have found a set of growth parameters that allow the growth of high quality single crystalline YIG films on the GGG substrate from a polycrystalline target.

4.3 Morphology

The surface morphology of YIG film was measured by atomic force microscopy, operated in tapping mode in air. AFM was done on the annealed YIG films to track the surface roughness. The surface roughnesses were measured over a different scan size of the films over a wide range of thicknesses. Before annealing, we analysed the surface of as-deposited YIG film which shows a rough surface with roughness of about 30 Å, shown in figure 4.9. .

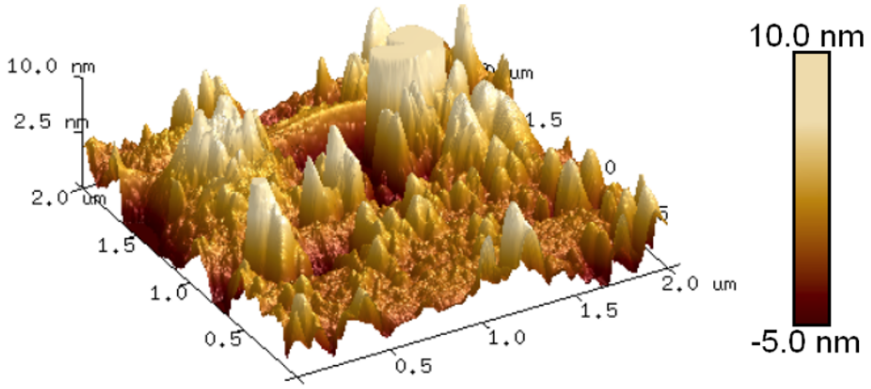

Figure 4.9: *AFM image showing the topography of an as-deposited 60 nm YIG film. The film appears very rough with surface roughness of 30 Å.*

Now we are going to show our AFM results of annealed YIG films. For a 60 nm thick film, the roughness of the film is 1.25 Å over a scan size of 5 μm^2 and 40 nm thick YIG showed smooth surface with R_{RMS} = 0.9 Å over a scan size of 4.5 μm^2, shown in figure 4.10. RMS roughness reported in ref. [59] are between 2 Å and 3 Å over 1 μm^2 ranges for all films (4-20 nm) deposited by pulse laser deposition (PLD). Figure 4.11a shows the surface morphology over a large scan size of about 13 μm^2 with its top view image (figure 4.11b) with RMS roughness value 1.8 Å. So our films have uniform roughness over a large area also. Our YIG films appears smooth over a large area for a wide range of thickness. The surface roughness of a series of YIG films in the 6-70 nm thickness range have surface roughness of 1-3 Å, shown in figure

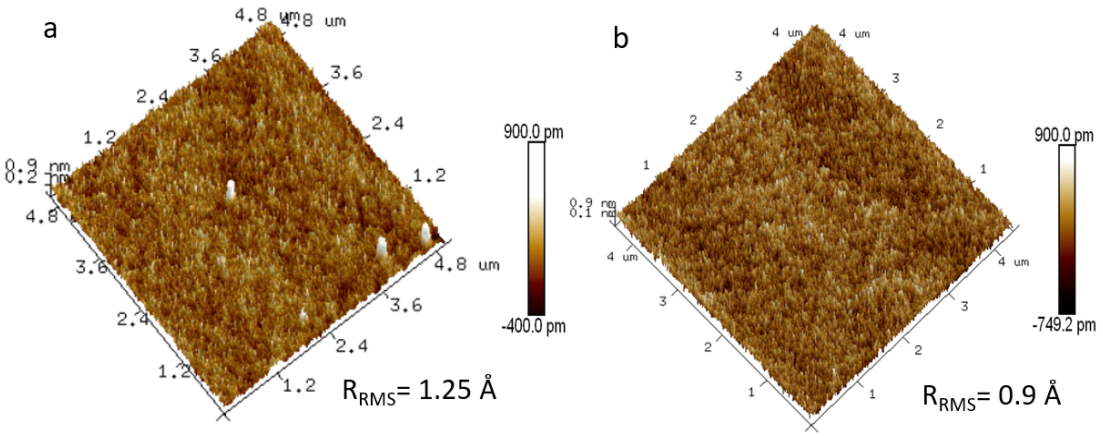

Figure 4.10: *5 μm X 5 μm AFM surface topography of a 60 nm (a) and 40 nm of scan size 4.5 μm X 4.5 μm (b) YIG films on GGG (111). Films are smooth with RMS roughness of about 1.25 Å and 0.9 Å respectively.*

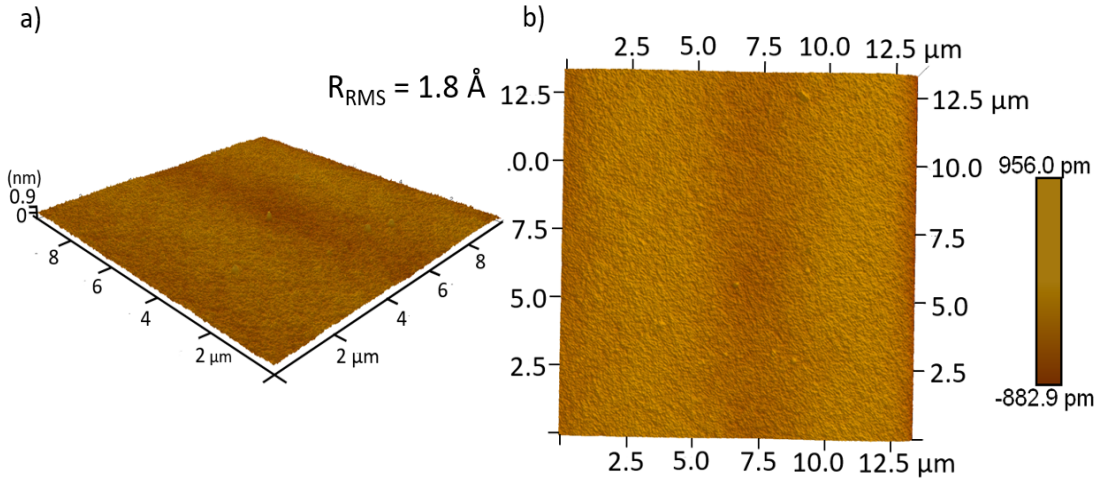

Figure 4.11: *Surface topography of a 40 nm thick film over a large scan size of about 13 μm^2 with its cross-sectional (a) and top view image (b) showing RMS roughness value 1.8 Å. Films appear smooth over a large area.*

4.12. This flat smooth surface is very important to make a good YIG/metal bilayer structures.

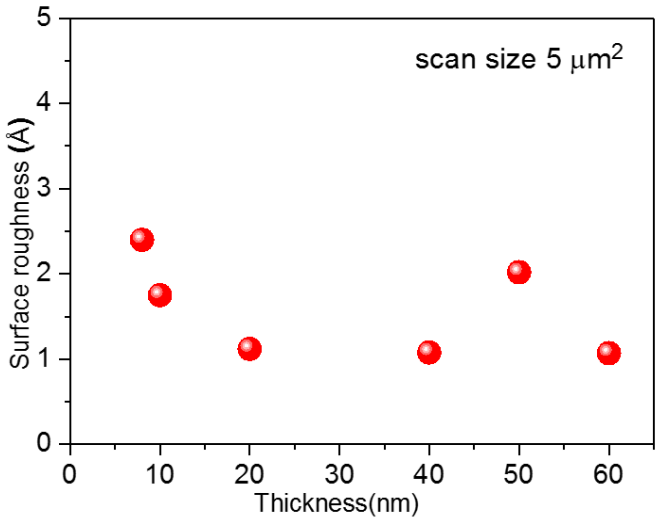

Figure 4.12: *Average surface roughness of annealed YIG films was measured by atomic force microscopy (AFM) over an area of 5 x 5 microns. The films surface morphology was plotted over a wide range of thickness where it can be seen that the surfaces are smooth with an RMS roughness of about 1-3 Å.*

4.4 Effect of Piranha etching

We did the surface treatment of YIG films by piranha etching [51, 150]. Piranha etch solution is a mixture of sulphuric acid (H_2SO_4) and hydrogen peroxide (H_2O_2) in the ratio of 3:1. It is strongly oxidising and removes metals and organic contamination. As our films are annealed in open air conditions, this could have lead to the contamination of the top surface. To get rid of the contamination from the YIG surface we treated our samples in piranha solution.

Before the actual surface treatment by piranha, all samples went through a conventional pre-cleaning step consisting of basic cleaning by acetone and isopropanol in an ultrasonic bath. Due to the self-decomposition nature of hydrogen peroxide, each time piranha solution was freshly-prepared. After mixing the solution, an exothermic reaction takes place at 120°C. The equation for this reaction is:

$$H_2SO_4 + H_2O_2 \rightarrow H_2SO_5 + H_2O \tag{4.1}$$

The etching rate depends on the temperature and volume of the etching solution. Also, immersing a sample into the solution should be done slowly to prevent thermal shock that may crack the material.

Piranha etching removes the contamination from the top surface, and in addition it removes magnetic material from the top (section 5.2.3). The XRR is necessary to know the final thickness of the sample after etching, and hence the etching rate. In general, the hotter the acid the higher the etch rate. The rate of cooling after the sample inserted cannot be controlled with the available facilities. Also, it is known that the wet etching process is difficult to carry out in a very controlled manner. From the XRR measurements of etched samples (figure 4.13), we found a considerable decrease in the thickness of the sample, which confirms it is removing active layer from the top surface. From figure 4.13, we can see that the thickness gets reduced by about 5 nm after etching. This in turn will reduce the magnetisation of the etched sample. XRD measurements are not substantially affected by piranha etching of the YIG as no difference was observed except an anticipated reduction in the peak intensity that is proportional to the removed YIG thickness from the top.

Figure 4.14 (a) and (b) shows the surface topography over 5 x 5 μm^2 for 19 nm and 39 nm annealed YIG sample after etching. It gives the surface roughness of about 2 Å for each film. Thus, from our AFM analysis of etched film we observed that there is no degradation of surface roughness of YIG films after the etching.

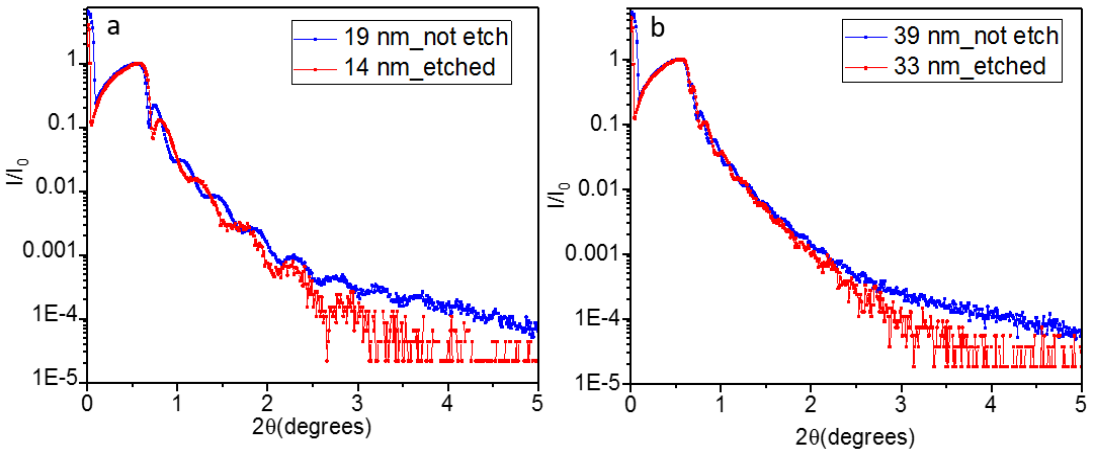

Figure 4.13: *X-ray reflectivity curves of 19 nm (a) and 39 nm (b) thick YIG films, which shows a considerable reduction in the thickness after piranha etching, giving 14 nm and 33 nm respectively.*

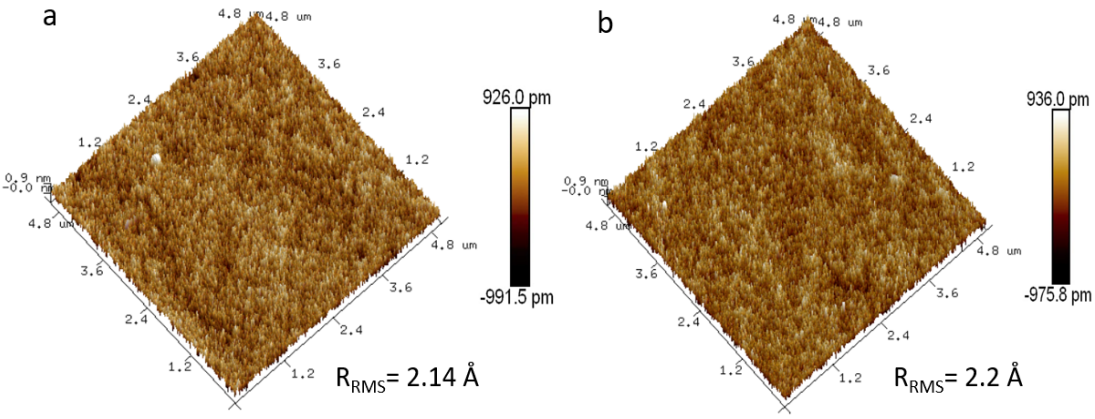

Figure 4.14: *AFM images of the YIG thin films of two different thicknesses: 19 nm (a) and 39 nm (b) after etching. Topography of the films over 5 x 5 μm^2 showed smooth surface with an RMS roughness of about 2 Å.*

4.5 Compositional analysis

4.5.1 Atomic scale investigation using scanning transmission electron microscopy (STEM)

We carried out an atomic-scale investigation of the YIG/GGG interface using aberration-corrected scanning transmission electron microscopy (STEM) in order to get direct confirmation of interdiffusion at the YIG/GGG interface. This work was done in collaboration with Q. Ramasse of SuperSTEM Laboratory in Daresbury. Scanning transmission electron microscopy (STEM) and electron energy loss spectroscopy (EELS) were carried out on a Nion UltraSTEM100 instrument operated at 100 kV acceleration voltage. From the EELS maps, we estimated the composition profiles (and averaged across the interface). These are known to be inaccurate for most of the edges in these compounds. Therefore, the compositions should only be seen as indicative of trends and the uncertainty on these numbers is of the order of 10 %.

From the High-angle annular-dark-field (HAADF) images of the interface along the [110] zone axis, we observed a gradual transition of the intensity from the GGG substrate to the YIG film: this is shown in figure 4.15a, with identical observations along the entire interface. Given the sensitivity of this imaging mode to the average atomic number, Z, of the material (the HAADF contrast is approximately proportional to $Z^{1.7}$) [151], this indicates a chemically-diffuse region at the interface, rather than a sharp interface. This is in good agreement with our XRR fitting results. Electron energy loss spectroscopy (EELS) provides further evidence of the interdiffusion of the various cations across the interface. The chemical maps of Ga, Gd, O, Y and Fe were recorded across the interface region, defined by the white rectangle in figure 4.15a. We obtained the averaged composition profiles by integrating these maps across the interface, which indicate a 6.5 nm wide region of mixed chemical composition. The compositions on either side of this region correspond to the expected bulk values for YIG and GGG, as shown in figure 4.15b.

This interdiffusion region is marked by dotted lines, for a guide to the eye in fig-

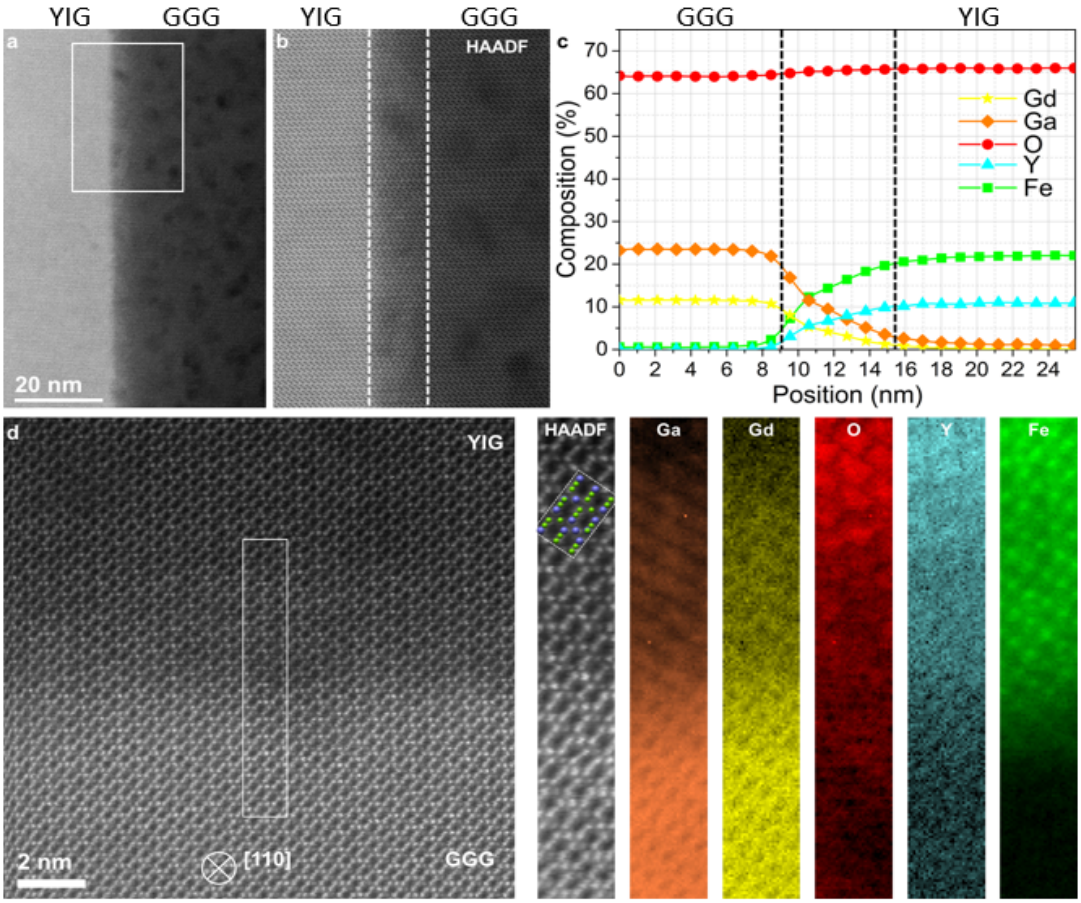

Figure 4.15: *Analytical STEM characterisation of the YIG/GGG interface. (a) HAADF survey image of the interface (YIG: left, GGG:right). A white box indicates the region over which the EELS spectrum imaging was carried out, yielding compositional profiles (obtained using tabulated Hartree-Slater cross-sections) averaged across the interface (YIG:right, GGG:left) (c). The HAADF intensity recorded simultaneously with the EELS maps is shown in (b) with white dotted lines indicating as a guide to the eye a* $\sim$ *6 nm wide region over which some interdiffusion of Gd, Y, Ga and Fe is observed (corresponding to the region marked with dotted lines on the profiles in (c)). Panel (d) shows a higher magnification EELS analysis of the interface (rotated 90 degrees to (a)) in the region indicated by a white box on the HAADF survey image. Maps for Ga, Gd, O Y and Fe are presented, along with the simultaneously acquired HAADF intensity, over which a ball model of YIG in [110] orientation is overlaid (green balls represent Fe, blue balls represent Y, and oxygen is not represented for clarity). Image courtesy: Q. Ramasse.*

ure 4.15b and the HAADF image was acquired simultaneously with the EELS (figure 4.15c). The shape of the EELS element intensity profiles are consistent with diffusion of Gd and Ga from the substrate into the YIG layer. The intensity profile for Y and Fe is inverted, this is most possibly indicating diffusion of vacancies from within the YIG layer to the original YIG/GGG interface (which probably acting as a vacancy sink) and hence Y and Fe are diffusing away from the interface. As a result, we can make a point that we have a 4-6 nm wide Gd- and Ga-doped YIG layer near the interface. Images and chemical maps obtained at higher spatial sampling provide an atomic-scale picture of the interface. But due to tight packing arrangements of the atoms in this orientation, it is difficult to confirm the exact lattice position of the interdiffused cations (figure 4.15d). In figure 4.16, we presented a ball model of YIG in [110] orientation, where green balls represent Fe, blue balls represent Y, and oxygen is not represented for clarity. Nevertheless, from these results we are now in a position to have a clear confirmation about the extent and chemical nature of the interdifusion at the YIG/GGG interface. This is in remarkable agreement with the conclusions obtained about the interfacial diffusion from the other techniques. In the YIG/GGG system, it is known that Gd and Y diffuse in pairs with similar diffusion coefficients through the *c* sites, reported in reference [152]. An interdiffusion region of width 6 nm corresponds to a diffusion lengthscale of $\sim$3 nm either side of the original interface boundary. We estimated a diffusion coefficient of $\sim$1.25 x 10^{-17} cm^2 s^{-1} from our annealing conditions (850°C for 2 hours). This value compares favourably with a extrapolated diffusion coefficient for Y in YIG at 850°C of between 10^{-17} and 10^{-18} cm^2 s^{-1} (from Fig 8 in ref [153]).

From the work reported by the Gallagher *et al.*[149], one can see that a STEM/EDX profile across a similar YIG/GGG interface exhibits an interfacial transition regions of about 5 nm (for Ga and Fe). They interpreted this to delocalisation of the X-ray emission due to probe broadening and inelastic delocalisation rather than elemental interdiffusion; however, this delocalisation appeared to vary between different elements. We believe our STEM/EELS results, which were measured on a large number of different regions along the interface, do not suffer such problems with delocalisation and

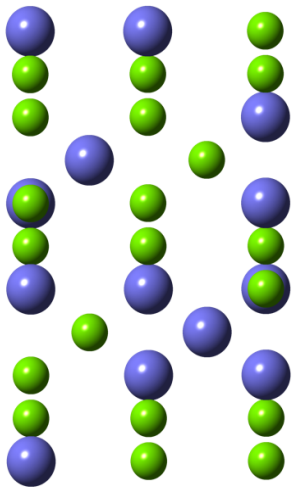

Figure 4.16: *A ball model of YIG in [110] orientation is overlaid (green balls represent Fe, blue balls represent Y, and oxygen is not represented for clarity).*

hence can be attributed to chemical intermixing. This gives a good matching with our results obtained from the XRR data fitting and room temperature magnetometry.

4.5.2 Rutherford back scattering (RBS) study

Rutherford back scattering (RBS) determines the elemental composition of a material based on the energies of scattered alpha particles. Rutherford backscattering (RBS) measurements were done at the CTN/IST Van de Graaff accelerator in the universal chamber where one detector is installed at 160° scattering angle. Spectra were collected for 2 MeV $^4He^+$. The angle of incidence was from 5° (near normal incidence) to 80 ° (grazing angle). This measurement is performed at Campus Tecnológico e Nuclear, Instituto Superior Técnico in Portugal. The RBS data were analysed with the IBA DataFurnace NDF v9.6h [154] by N.P. Barradas.

For each sample, always more than one spectrum was acquired at different angles of incidence θ. It was not possible to analyse all the spectra from one sample with the same model (i.e. depth profile), which is an indication that the films are not homogeneous. A further indication of film inhomogeneity was that, the determined YIG film

thickness showed variation for different angles of incidence, for the same sample. This means that the beam is normally probing areas with different film thickness. Quantification of diffusion becomes difficult to analyse, because diffusion is observed in the data as signal broadening, and a distribution of film thickness is also seen as signal broadening.

As the angle of incidence grows towards grazing incidence, the beam spot size on the sample becomes larger with $1/\cos(\theta)$. This means that a larger part of the sample is analyzed. Therefore, if there is indeed an inhomogeneous film thickness, we could expect that at a more grazing angle the signal broadening would increase. This would lead to a larger "diffusion" to be determined. This is actually the case: for a given sample, the larger (more grazing) the angle of incidence, the more diffusion is needed in the model to explain the data. However, while precise values for diffusion cannot be determined from the data, it is possible to determine average thickness values, as well as elemental concentrations.

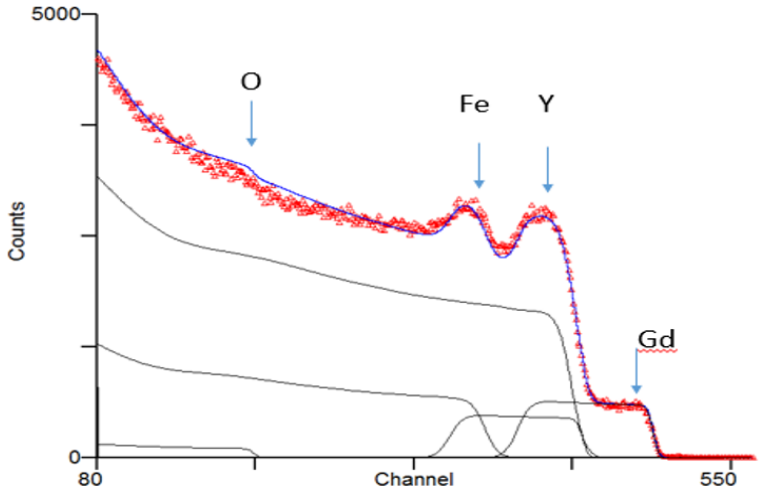

Figure 4.17: *RBS spectrum of 80 nm annealed YIG sample with 2 MeV 4He$^+$ beams at a scattering angle of 75°. The solid line (blue) is a fit to the experimental data (red dotted curves). The RBS spectra shows four sharp discontinuities corresponding to $^4He^+$ ions backscattered from O, Fe, Y and Gd atoms.*

Figure 4.17 shows the RBS spectrum of 80 nm thick YIG sample with blue curve

is a fitting to the experimental data (red dotted curve). The fitting of the RBS spectra shows four sharp discontinuities corresponding to $4He^{+}$ ions backscattered from O, Fe, Y and Gd atoms. Gd is apparently diffusing from GGG substrate at the YIG/GGG interface. It is possible to estimate the elemental depth concentration profiles for each to obtain the stoichiometric value. Figure 4.18 shows the elemental depth concentration profile used to make the fit. This shows that the top layer of the annealed YIG film contains Y, Fe and O with the corrrect stoichiometric value of the film $Y_3Fe_5O_{12}$. But near the interface ($\sim$6 nm) we observed the depression in the Y and Fe concentration. From the model, it indicates that at the interface region there are other elements Gd, Ga in addition to Y, Fe and O. This tends to indicate diffusion in the open lattice structure of YIG due to high annealing temperature. We can estimate the stoichiometry near the interface to be $Y_{0.4}Gd_{2.6}Fe_5O_{12}$. It seems that Y and Gd diffusion occurs in pairs and this agrees well with the YIG/GGG system as reported in [152].

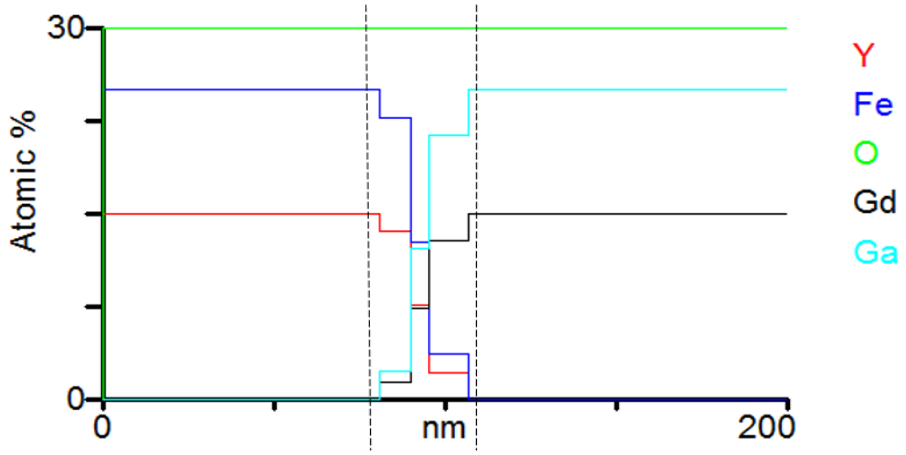

Figure 4.18: *Elemental depth concentration profiles of Y, Fe, O, Gd, and Ga near $Y_3Fe_5O_{12}$ surface and YIG/GGG interface estimated by RBS. The top layer of the film contains Y, Fe and O with the correct stoichiometric of the film $Y_3Fe_5O_{12}$. The interface region as shown between the dotted boundary lines indicates the presence of other elements Gd, Ga in addition to Y, Fe and O.*

4.6 Conclusion

In this chapter, we performed a comprehensive study of the crystallinity and morphology of the RF sputtered YIG films and also the chemical nature of the YIG/GGG interface after annealing. The influence of the deposition and annealing conditions on the structural quality of the samples was studied by x-ray reflectivity and x-ray diffraction analysis. The single crystalline (111)-oriented YIG films are grown from the polycrystalline YIG target. From XRR results of annealed YIG sample, we identified an interdiffusion region of about 6 nm thick at the YIG/GGG interface.

The low deposition rate and optimum target-substrate distance enabled the growth of smooth YIG films. Our AFM results for a series of YIG films of varying thickness confirmed that our films are smooth with roughness about 1-3 Å. From x-ray reflectivity measurements we found that piranha etching removes the active layer of YIG from the top surface while removing the contamination. The surface of the YIG films remain smooth after etching.

The results obtained using atomic resolution STEM emphasize the impact of high temperature annealing at the interface of YIG and GGG. This also confirms the diffusion of Gd and Ga at the interface forming Gd and Ga-mixed YIG region, which can affect the stoichiometry of YIG near the interface. Our YIG/GGG system can be approximately represented by a two-layer model: YIG and another layer of YIG doped with Gd. The Gd-rich YIG layer with a highly disordered structure is located near the interface and the upper layer can be estimated as an almost perfectly formed YIG. In addition to STEM results, RBS measurements tend to indicate that Y and Gd diffusion in pairs. The formation of diffusion region due to high annealing temperature can lead to structural modifications and anamolous magnetic properties of YIG as compared to bulk YIG.

The most important result is the 4-6 nm Gd-rich diffused layer at the YIG/GGG interface. So, there is a further scope to optimise the growth methods and annealing conditions to minimize the diffusion. We could possibly use low temperature annealing to avoid this interlayer mixing. We can also try to introduce a buffer layer between the

YIG and substrate interface. In summary, we suceeded to grow good quality ultrathin YIG films by sputtering which are useful in the investigation of the origin of novel magnetic phenomena in insulator metal hybrid structures.

CHAPTER 5

Magnetic properties of nm-thick YIG films

5.1 Introduction

In this chapter, we report the magnetic properties of nanometre thick RF sputtered YIG films. For the growth of high quality thin films the lattice mismatch between the film and the substrate is an important parameter. The lattice constant of cubic GGG is 12.383 Å which leads to negligible lattice misfit (0.03%) and makes GGG an excellent choice as substrate. The nm-thick single crystal YIG films were deposited on (111) oriented 0.5 mm thick GGG substrates. YIG exhibits a ferrimagnetic order with the transition temperature of 560 K. Below the Curie temperature, the Fe^{3+} spins of the *a* sites align antiparallel to those present at the *d* sites due to the superexchange interaction and along the magnetic easy axes (111) directions (section 2.2).

Fabrication of spintronic and magnonic devices requires thin films of YIG with high magnetic quality, even though a detail characterisation of the magnetization is lacking. Here, we investigated the magnetic properties of single crystal YIG films by using VSM and SQUID-VSM. The thickness dependence measurement is performed to find the saturation magnetisation, coercivity and the thickness of the dead-layer region. Results from SQUID-VSM magnetometry have made a major contribution to this work by measuring the magnetic moment of the samples with very high sensitivity in the wide temperature range 1.8 K to 300 K. The temperature dependence of the magnetisation M(T) shows an unexpected downturn in magnetisation in the low temperature region which has not been reported before. These M(T) measurements were done for different thicknesses of YIG ranging from 10 nm to 250 nm. The Curie temperature (T_C) of bulk YIG is 560 K, so we measured at high temperature to find the value of T_C for nm-thick YIG films. We carried out the surface treatment of YIG by piranha etching to study its effect on the magnetisation of YIG. We also measured the temperature dependence of magnetisation of YIG deposited on YAG ($Y_3Al_5O_{12}$) substrates and compared the M(T) results with that obtained from the YIG on GGG substrate.

Polarised neutron reflectivity (PNR) is an excellent tool to provide magnetic information of the sample. To our knowledge so far we are the first to perform the PNR

experiments in YIG samples to extract the magnetic information, particularly at the YIG/GGG interface. Then, we compared our magnetometry and PNR results to get an idea about the orientation of the magnetic moment of Gd-diffused region at the YIG/GGG interface. Finally, we used a simple two-layer model (YIG and Gd-diffused YIG layer) for our film to fit the M(T) curves for each YIG thickness. The correlation between the results obtained from the magnetometry, polarised neutron reflectivity and our fitting is very high.

5.2 Magnetometry

5.2.1 Thickness dependent magnetic properties

We have studied the thickness dependent magnetic properties of YIG on (111) GGG substrate by using Vibrating sample magnetometer (VSM). In the following, we compared our results with the values obtained for bulk YIG. At first, we measured the hysteresis loops as a function of applied field at 295 K to find the net magnetic moment m and the coercivity H_c. For this, a magnetic field of 5 mT was applied in plane along the easy axis of the sample. We set the direction of easy axis of our samples during the growth with the help of an array of magnets attached to the shutter wheel. During the deposition, the substrate sits at the centre of these magnets. Measurements were carried out at constant temperature for each sample. Figure 5.1 shows a typical dependence of the magnetic moment versus in plane magnetic field (m-H) of a 40 nm thick YIG film at 295 K (blue curve). We observed that in magnetometry measurements the signal from the thin film of YIG is dominated by the paramagnetism induced by the Gd^{3+} ions in the GGG substrate generating a large background signal (black curve).

To substantiate the paramagnetism in GGG, we measured a m(T) curve at 10 mT on cooling the GGG substrate from 300 K to 3 K as shown in figure 5.2. The temperature dependence of the magnetization curve in GGG obeys the Curie law ($\propto$ 1/T). The paramagnetic background signal increases with decreasing temperature. Inset shows

the inverse of the susceptibility χ as a function of temperature that provides the value

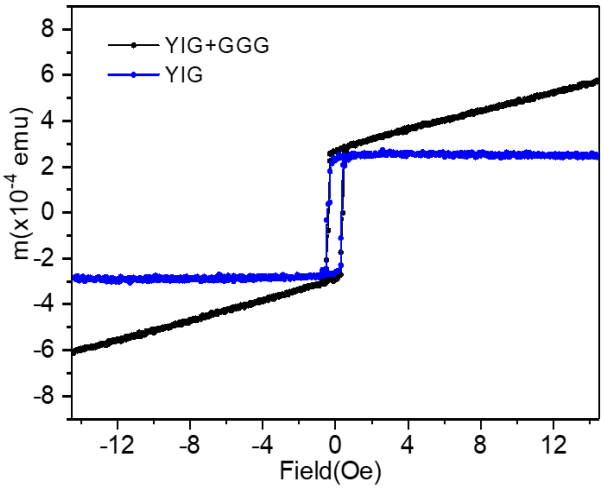

Figure 5.1: *The net magnetic moment of a 40 nm thick YIG film on GGG substrate versus in plane magnetic field at 295 K (black curve). The blue curve shows the magnetic moment as a function of applied magnetic field after the subtraction of the paramagnetic contribution from the GGG substrate.*

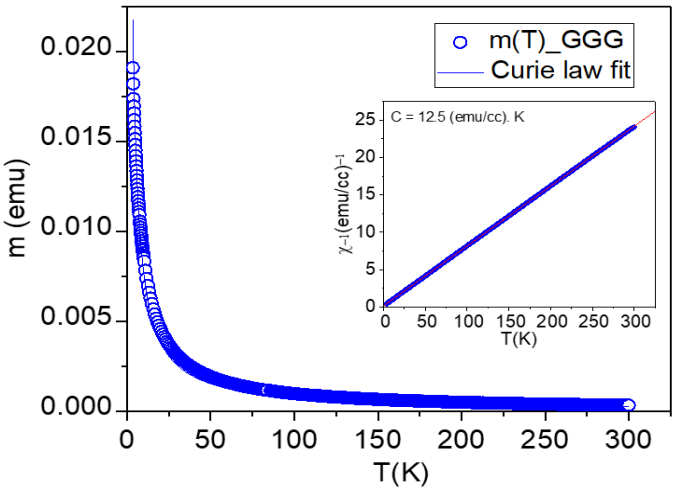

Figure 5.2: *m(T) curves at 10 mT for a (111) GGG substrate on cooling the substrate from 300 K to 3 K. This shows the large paramagnetic signal coming from the localized Gd^{3+} moments of the GGG substrate. Inset: 1/χ vs. T which gives Curie constant C = 12.5 (emu/cc)K.*

of Curie constant C. The volume of a film, for example, 50 nm YIG film, V_{film} = 0.4 cm x 0.4 cm x 50 nm = 8 x 10^{-7} cm^3 is about 4 orders of magnitude smaller than the volume of GGG substrate, V_{GGG} = 0.4 cm x 0.4 cm x 0.5 mm = 8 x 10^{-3} cm^3. So, the total measured magnetic moment of substrate and film is dominated by the paramagnetic moment of the substrate. Hence, the data needs to be corrected by subtracting the paramagnetic background signal coming from the GGG substrate.

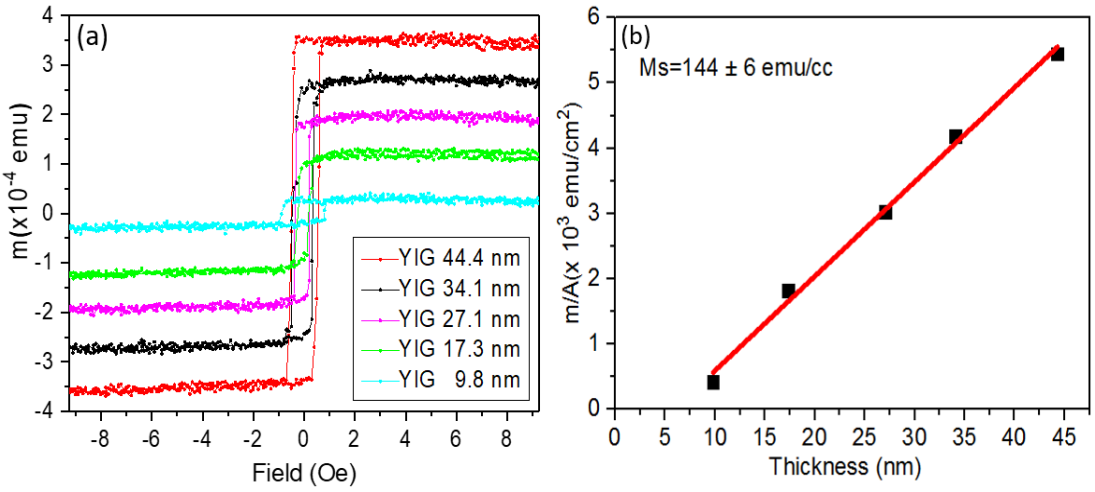

Figure 5.3: *(a) Magnetic moment as a function of applied field at room temperature for a range of YIG thicknesses, obtained after subtraction of the paramagnetic contribution from the GGG substrate. The data shows that the coercivity of our films is very low, 0.30 ± 0.05 Oe. (b) The linear extrapolation of the saturation magnetic moment over area as a function of thickness indicates that there is a dead layer of about 6 nm thick. The saturation magnetisation obtained from the slope is Ms = 144 ± 6 emu/cc.*

Figure 5.3a shows the hysteresis loops at 295 K for different thickness of YIG ranging from 9.8 - 44.4 nm, obtained after the subtraction of the paramagnetic contribution from the GGG substrate. The data shows that the coercivity is similar across these range of samples with a value of 0.30 ± 0.05 Oe. The coercivity of our film is very low which also indicates the high epitaxial crystal structure and high magnetic uniformity of our sputtered YIG films. Our coercive field value is comparable to the value of 0.35 Oe for off-axis sputtered, 16 nm - 164 nm thick YIG films [149, 155].

Our H_c value is about 10 times smaller than reported in ref. [156] for PLD-grown YIG film (2 Oe) and about 100 times smaller than reported in ref.[157], which is 15-30 Oe for different YIG thicknesses. The saturation magnetic moment *m*, depends linearly on the thickness of the film (figure 5.3b). The magnetization can be obtained from the measured magnetic moment by determining the thickness of each sample and using the volume of the material. The linear extrapolation of the magnetic moment over area versus thickness indicates the presence of a *magnetically-inactive layer*, sometimes called a dead layer, of $\sim$ 6 nm. In magnetic thin films, it is common that the dead layers are usually found at the sample/substrate interface and in this YIG/GGG system, the dead layer thickness corresponds remarkably well to the diffusion region indicated by the x-ray reflectivity (section 4.2.1) and the STEM analysis (section 4.5.1). The interpretation thus far is that Gd and Y have interdiffused at the interface region during annealing, but at room temperature this interface is paramagnetic because 295 K is well above the ordering temperature of Gd^{3+}(which is between 65 K - 85 K) in Gd-doped YIG [158]. The slope of this curve indicates a saturation magnetisation value of 144 $\pm$ 6 emu/cc, which agrees well with the bulk magnetisation value M_s = 140 emu/cc at 295 K [159]. This also indicates that at room temperature the magnetization is independent of thickness.

The Curie temperature of a ferrimagnet is given by

$$T_C = \mu\sqrt{C_A C_B} \tag{5.1}$$

where C_A and C_B are the Curie constants of Fe^{3+} ions on the *a* and *d* sites respectively, and μ is the mean field constant [160].

Figure 5.4 shows the Curie temperature of a 72 nm thick YIG film. The experimental data is fitted using Bloch's $T^{3/2}$ law, which describes the temperature dependence of magnetisation of magnetic materials [160]. The magnetisation as a function of temperature is given by

$$M(T) = M_0[1 - (T/T_C)^{3/2}]^{\beta} \tag{5.2}$$

where M_0 is the spontaneous magnetisation at absolute zero, T_C is the Curie temper-

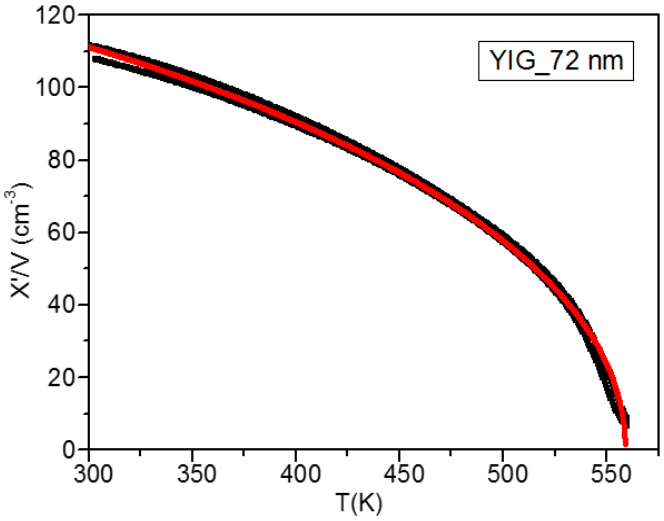

Figure 5.4: *Susceptibility versus temperature for 72 nm thick YIG film. The solid line is a fit using the Bloch $T^{3/2}$ law and this gives the value of Curie temprature 559 $\pm$ 4 K which is close to the bulk value 560 K. Here β = 0.47.*

ature and β is a critical exponent. This equation is an empirically modified version of Bloch's law to take into account the anisotropy and behaviour close to T_C. The fitting to the Bloch law illustrating that the value of T_C = 559 $\pm$ 4 K, is close to the bulk value of YIG which is 560 K [160]. This value is comparable to 551 K as reported by K. P. Belov *et al* [161]. The observed Curie temperature in YIG is due to the superexchange interaction between ferric ions in *a* and *d* sites mediated by the O^{2-} ions. Superexchange interaction is defined as an indirect exchange interaction between two non-neighbouring magnetic ions mediated by a non-magnetic ion which is located between the magnetic ions.

5.2.2 Temperature dependence of magnetisation

Magnetic characterisation was performed in the temperature range of 1.8 K to 350 K in a vibrating sample superconducting quantum interference device (SQUID) magnetometer: MPMS3 by Quantum Design. The magnetic field was applied in plane to our

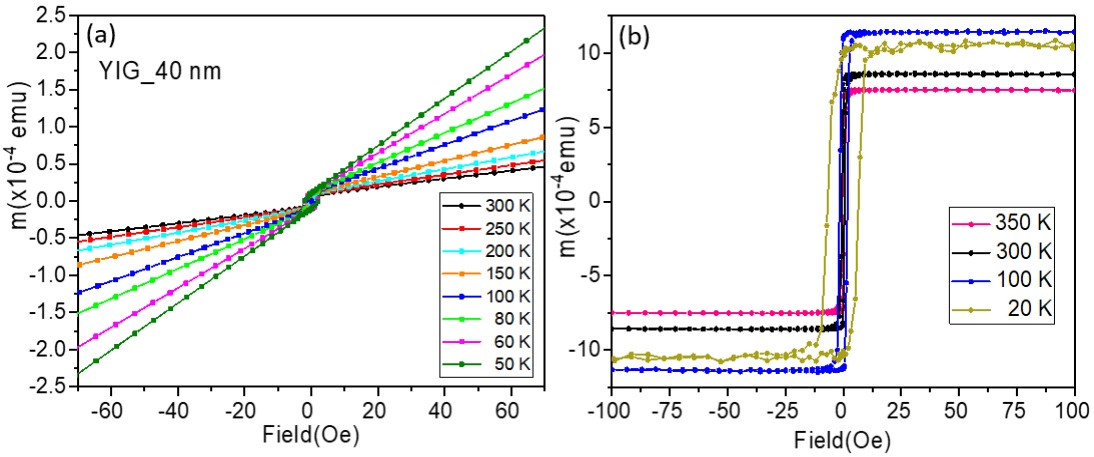

Figure 5.5: *(a) Hysteresis loops as a function of applied field at different temperatures for 40 nm thick YIG film. This shows that with decrease in temperature paramagnetic background signal from the substrate increases. (b) Hysteresis loops obtained after the subtraction of paramagnetic background shows that due to the role of Gd^{3+} ions, magnetic moment starts to decrease at low temperature.*

samples. Hysteresis loops were obtained at various temperatures in an applied magnetic field (H) of -300 Oe to 300 Oe to ensure that the sample was saturated (figure 5.5a). From these hysteresis loops, one can easily observe an increase in the paramagnetic contribution with decrease in temperature, that is in accordance with the m(T) behaviour of GGG as shown in section 5.2.1. The magnetic moment at each temperature was calculated from the hysteresis loops by correcting the linear paramagnetic slope, shown in figure 5.5b. These measurements were done for different thickness of YIG films to obtain the magnetisation curve for each sample.

The saturation magnetisation as a function of temperature M(T) for a series of YIG thicknesses is plotted in figure 5.6, which shows an unexpected *decrease* in magnetisation with decrease in temperature in the low temperature region. The most probable explanation on the reduction of magnetisation (ΔM) at low temperature is as follows. Diffusion of Gd from the GGG substrate as a result of annealing at high temperature will substitutes Gd for Y to form either Gd-doped YIG or highly disordered Gd-rich

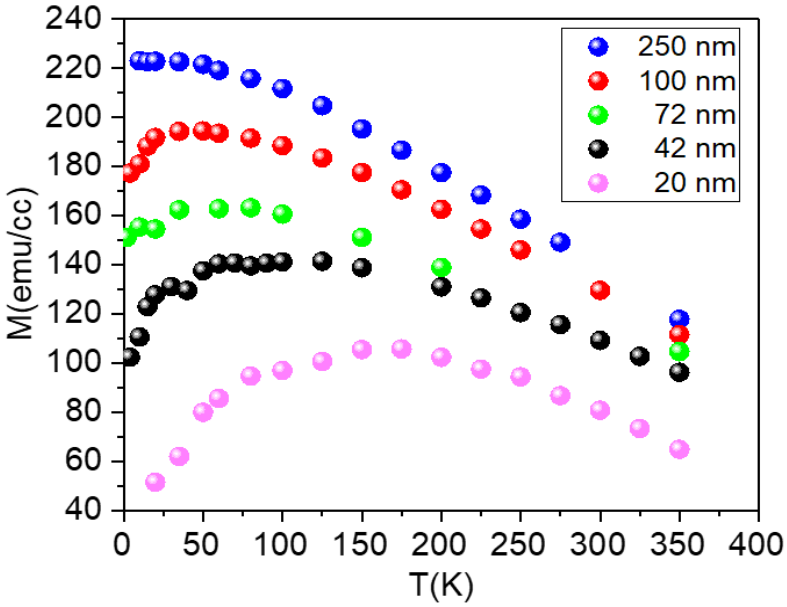

Figure 5.6: *The temperature dependence of the saturation magnetisation for different YIG thickness where we observed an unexpected decrease of M(T) in the low temperature region. Each data point presented in the M(T) curve is extracted from the hysteresis loops measured at different temperatures.*

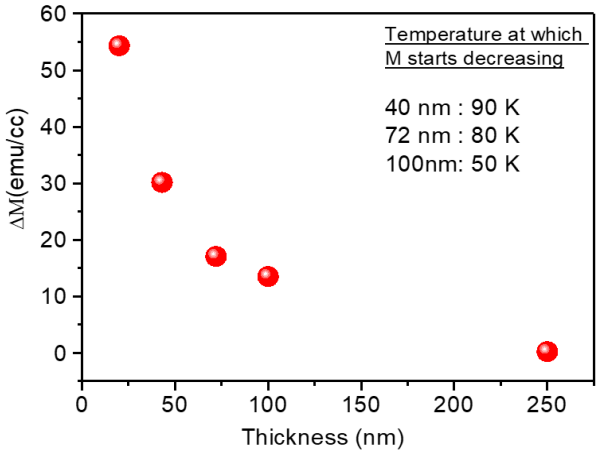

Figure 5.7: *Magnetisation reduction ΔM as a function of thickness. It shows that with the increase in film thickness the amount of reduction in the magnetisation decreases and almost disappears for 250 nm thick film.*

YIG layer at the interface between GGG and YIG. Our fit to the x-ray reflectivity curve gives an estimate of Gd diffusion region thickness of about 6 nm at the interface. Also from the magnetometry data at room temperature, we obtained the value of dead layer thickness, which is 6 nm (fig.5.3b, section 5.2.1). The magnetic behaviour of Gd sub-lattice has a strong temperature dependence. It is well known that Gd in GdIG orders antiparallel at low temperature and dominates the magnetic behaviour. The ordering temperature of Gd spins is 65-85 K in GdIG, due to which as the temperature is reduced, the magnetization of the Gd sub-lattice strongly increases and aligns antiparallel to the net magnetic moment of YIG.

So, our interpretation for the *magnetisation suppression* in YIG at lower temperature is that the Gd-spins in the Gd-diffused region aligning antiparallel and plays the dominating role to lower the net magnetization value in YIG near the interface. As indicated in figure 5.7, one can also see that with the increase in film thickness, the amount of reduction in the magnetisation (ΔM) decreases. This is because the thickness of Gd-diffused region forming at the bottom remains nearly the same but the thickness of the YIG layer increases. So for the thicker film, the magnetization of YIG starts dominating and the net cancellation by Gd spins gets reduced at lower temperature. This reduction in magnetisation almost disappears for 250 nm thick YIG film.

Next we deposited a very thin sample of 10 nm YIG on GGG, with the assumption that we could measure mainly the effect of Gd-spins diffused into the YIG from GGG after annealing. Figure 5.8a shows the temperature dependence magnetisation data for a 10 nm thick YIG film. This is a very important result which highlights the role of Gd spins at the YIG/GGG interface. This M(T) curve clearly shows a compensation point around 100 K. This region is near to the ordering temperature of Gd spins, indicating that the Gd magnetic sublattice dominates at lower temperatures. In GdIG ($Gd_3Fe_5O_{12}$), there are three magnetic sublattices: Gd^{3+}(*c* sites), Fe^{3+} (*a* sites), and Fe^{3+} (*d* sites) [163] (figure 5.8b). Above the compensation temperature T_{comp} (T $> T_{comp}$), the magnetic behaviour is mainly due to the two Fe sub-lattices which are

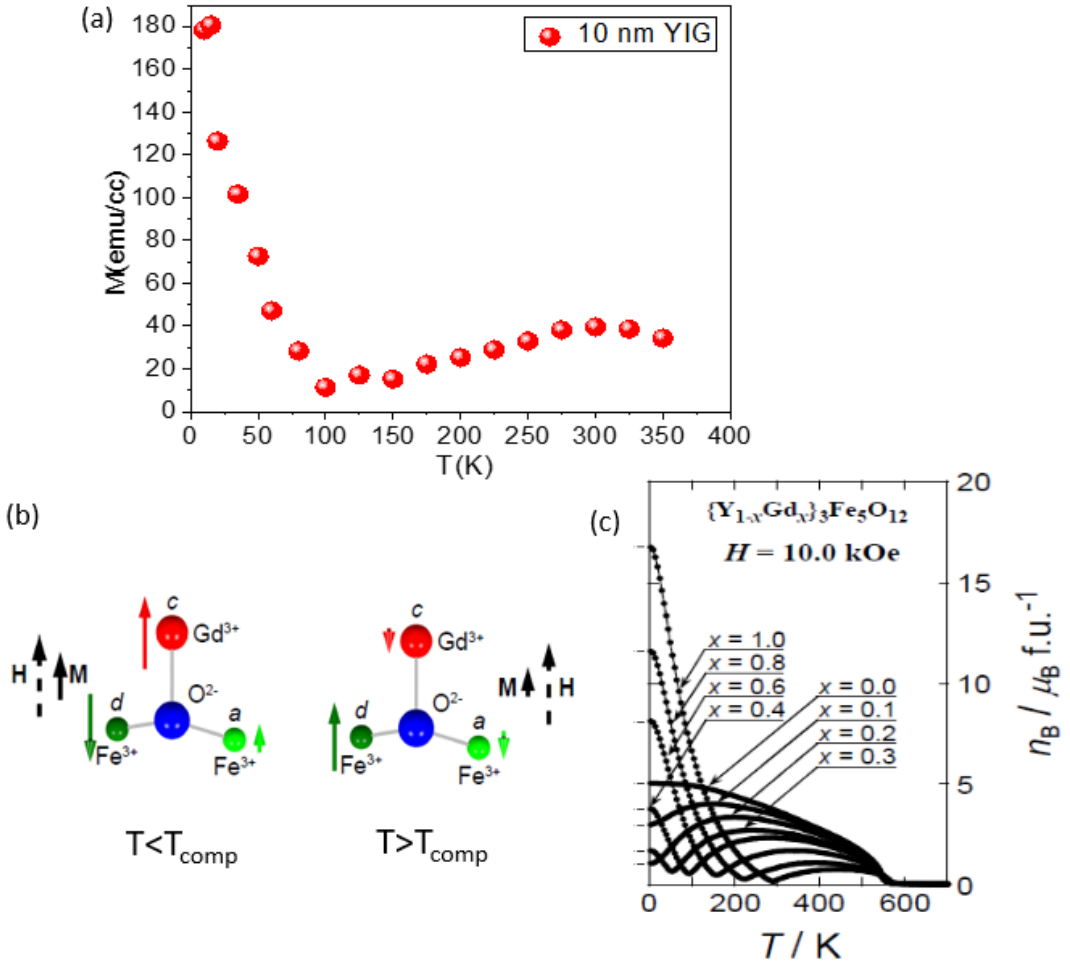

Figure 5.8: *(a) Temperature dependence of magnetisation of 10 nm thick YIG. (b) Schematic of three magnetic sublattices in GdIG. It shows the alignment of each sublattice below and above the compensation temperature T_{comp} [162]. Due to strong temperature dependence of the Gd sub-lattice, it dominates the magnetic behaviour for T <Tcomp, whereas for T >Tcomp the magnetic behaviour is mainly caused by the antiferromagnetic coupling between Fe sub-lattices at a and d sites. (c) The temperature dependence magnetisation curve for varying Gd concentration, which shows 40% Gd doping corresponds to 100 K compensation temperature [158].*

strongly coupled via antiferromagnetic superexchange with a Néel temperature T_N = 550 K. As the temperature decreases, the magnetization of the Gd sub-lattice strongly

increases, and together with the Fe magnetization at *a* sites overcomes the Fe magnetization at *d* sites. But since the Gd is weakly exchange coupled to the Fe at *a* sites, it leads to an ordering temperature of Gd spins around 65 K-85 K. At high temperature, Gd^{3+} ions lose their magnetization rapidly with increasing temperature and Fe ions at *d* sites dominate the magnetization of GdIG. So at the magnetic compensation temperature T_{comp}(GdIG) $\sim$ 288K (bulk value) [164, 165] the magnetization of the *a* site of Fe and the *c* site of Gd is equal in magnitude but aligns antiparallel to the magnetization of the d site of Fe, resulting in zero remanent magnetization of GdIG. According to the study reported in figure 5.8c of reference [158], the compensation temperature decreases with decreasing the concentration of Gd in Gd-doped YIG. In our 10 nm YIG film, a 100 K compensation temperature corresponds to 40 % Gd diffusion in the lattice structure of YIG. Since our magnetometry measurements are done in a 10 nm YIG film with 40 % Gd in the interdiffusion region at the YIG/GGG interface, the net magnetization does not vanish completely but reaches a minimum at the compensation point due to the response of the Gd sublattice. And at higher temperature the magnetisation increases again when the Fe^{3+} moments start to dominate. After a short increase in M, it attains a local maximum and after that the exchange interaction between ferric ions in *a* and *d* sites increases which finally leads to the zero magnetization of YIG at the Curie temperature, which is 560 K (bulk value).

From our magnetometry data, we observed a temperature evolution of the coercive field in the temperature range of 5 K to 385 K (figure 5.9). The coercive field decreases with increasing temperature. In successive temperature regions, we observed different slopes with breaking points, one at 50 K and another one around 325 K. In 1990s, G.Vertesy *et al.* reported the temperature dependence of coercive field in large family of epitaxial magnetic rare earth garnet films from 10 K to 485 K (Néel temperature) [166]. All the films considered for their study were grown on (111) oriented GGG substrates. They found the temperature dependence to be piecewise exponential with breaking points in subsequent regions. In figure 5.9, we also observed the similar behaviour, the semilogarithmic plots of $H_c(T)$ shows the decrease to be piecewise

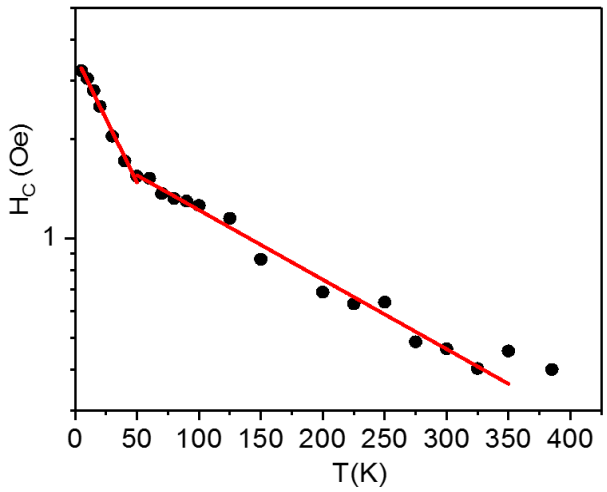

Figure 5.9: *The temperature dependence of the coercive field $H_c(T)$ of 100 nm annealed YIG sample shows a piecewise exponential dependence at successive temperature regions with different slopes and having breaking point around 50 K and 325 K. The semilogarithmic plot of $H_c(T)$ is fitted with the exponential function, $H_c(T)$=$H_i$exp(-T/T_i) in each of its linear parts.*

.

exponential having different slopes at two successive temperature regions. The semi-logarithmic $H_c(T)$ was fitted to the exponential function (eq. 5.3) in each of its linear parts.

$$H_c(T) = H_i \exp(-T/T_i) \tag{5.3}$$

where H_i and T_i are the characteristic values for the i-th temperature range. For each exponential segment, the fitting gives the values of H_i and T_i. In the temperature range 5 - 50K, H_i = 3.58 Oe and T_i = 56.5 K and for 50 - 325 K, H_i = 1.98 Oe and T_i = 206 K. This behaviour can be explained as the existence of two different types of wall-pinning traps (material defects) in the sample, each of them dominating in one of the two different temperature regions [166]. The breaking points on the plot marks the interaction of the wall-pinning traps, where the limits of activity of one type of wall-pinning trap and taking over of the next type. The temperature range and the position of breaking points can be considered as the characteristic of the sample. The change of slope of the $H_c(T)$ curve indicates the temperature at which a set of defects takes over

the dominant role in the domain wall coercivity from the previous set of defects. The decrease of $H_c(T)$ is less rapid at higher temperatures, which is most probably due to the existence of different sets of mutually nonequivalent wall-pinning defects in the sample. A large number of rare-earth garnet films demonstrated similar behaviour of piecewise exponential dependence of coercive field with temperature, resulting from the mutual interaction of wall-pinning traps [166, 167].

5.2.2.1 YIG/Pt hybrid structures

For our spin pumping and current induced FMR experiments, we used YIG/Pt bilayer structures, so it is crucial to check the magnetometry results after deposition of Pt on YIG by DC sputtering. For YIG/Pt hybrid structures, the obtained SQUID magnetometry results for the YIG layer remain unchanged qualitatively and quantitatively, as shown in figure 5.10.

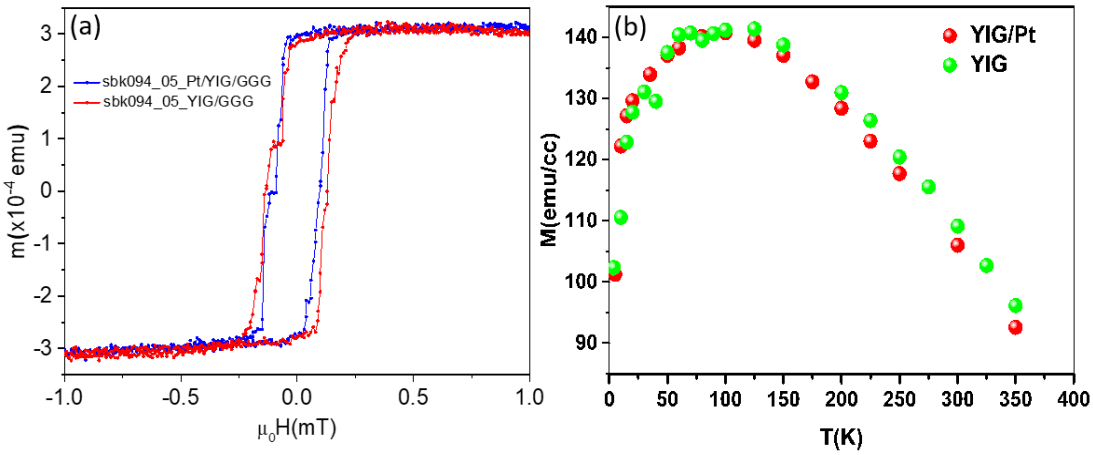

Figure 5.10: *(a) Hysteresis loops before (red curve) and after deposition of 10 nm Pt (blue curve) on 40 nm YIG films. (b) Temperature dependence of magnetisation for the same YIG (40 nm) and YIG(40 nm)/Pt(10 nm) hybrid structures which shows the same magnetisation reduction at low temperature.*

5.2.3 Effect of Piranha etching on magnetization

In this section our aim is to get confirmation about the location of magnetically dead layer near the YIG/GGG interface. For this we analysed our samples before and after etching. YIG samples were treated with Piranha solution (section 4.4) under same conditions and the etching time was kept constant.

To study the effect of etching, the magnetisation of the samples was measured at room temperature using a magnetometer. We observed that etching leads to the removal of a magnetically active layer from the top surface in addition to the contamination, leading to a decrease in the magnetic moment in each sample after etching, as shown in figure 5.11a and b. For the 40 nm sample, before etching the moment, m = 3.3 x 10^{-4} emu and after etching, thickness of YIG is 34 nm and the moment, m_1 = 2.7 x 10^{-4} emu. Hence, 6 nm reduction in thickness corresponds to 18% decrease in magnetic moment after etching. For an unetched 20 nm sample, m = 1.2 x 10^{-4} emu and after etching m_1 = 8.71 x 10^{-5} emu. So, a 27% decrease in the magnetic moment corresponds about 8 nm reduction in thickness. These values are an approximate as we should note that there is an effect of Gd at the interface in each film which we discovered later at the end of our study.

After etching, one of the samples was measured in the temperature range of 1.8 K to 385 K to get the temperature dependence of the magnetisation. If we compare the M(T) results before etching (42 nm YIG) and after etching (35 nm YIG), one can still observe the same downturn of magnetisation at lower temperature (figure 5.12). This is a good indication of the presence of diffused dead layer at the YIG/GGG interface. Also we found that the etching removes magnetically active layer from the top, and hence the magnetisation gets reduced, so we did not continue this piranha etching process anymore.

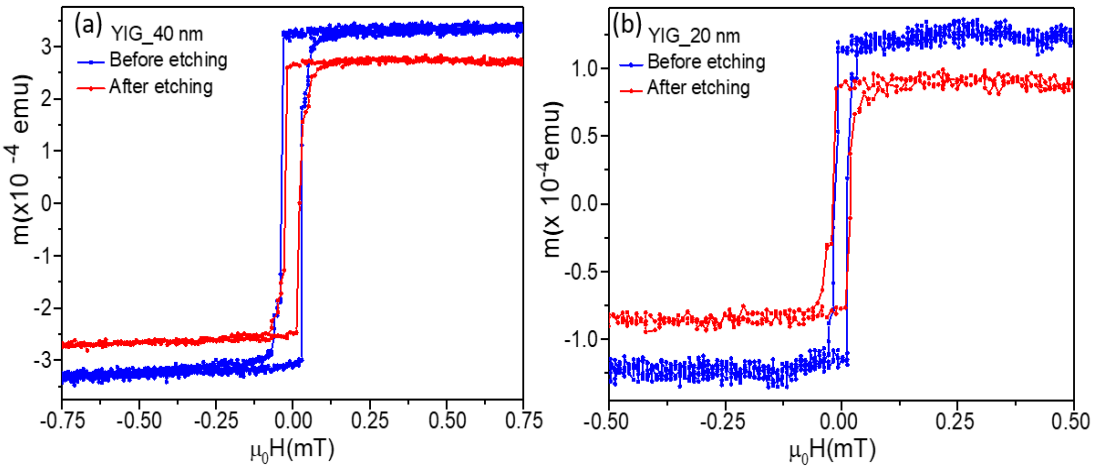

Figure 5.11: *Moment versus applied field curve before (blue curves) and after etching (red curve) of 40 nm (a) and 20 nm (b) thick YIG films. This shows degradation of magnetic moment after etching and hence removing an active layer from the top surface of YIG. For the 40 nm sample, the moment decreased by 18% after etching whereas for 20 nm thick YIG it shows 27% decrease.*

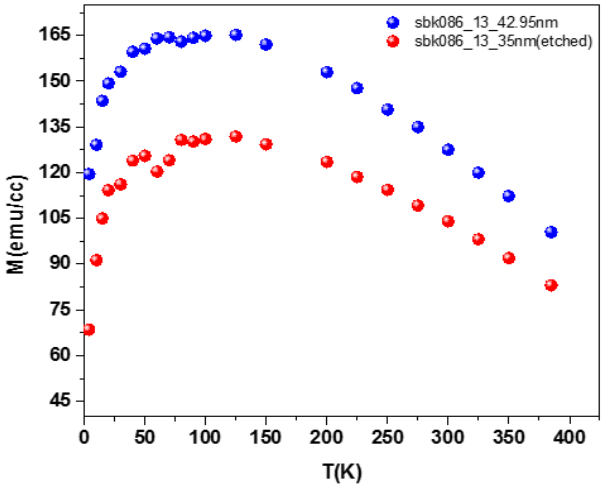

Figure 5.12: *Temperature dependence of the saturation magnetisation of 42 nm thick YIG before (blue dotted curves) and after Piranha etching (red dotted curves) where below 100K there is a reduction in M(T). The downturn behaviour is same in both cases but it is quantitatively different.*

5.3 Polarised neutron reflectivity measurements

To get more information of the magnetic behaviour and further confirmation about the magnetization downturn in this complex material YIG, a depth-resolved technique is required. Polarised Neutron Reflectivity (PNR) technique, is ideally suited for these measurements. The specular reflectivity of spin polarized neutrons depends on the depth profile of the sample magnetization parallel to the applied field as well as the depth profile of the nuclear composition. The YIG samples were taken to the Polarised Neutron Reflectometer, POLREF, at the ISIS neutron spallation source, Rutherford Appleton Laboratory for the temperature dependent polarised neutron reflectivity (PNR) measurements. By using a GMW electromagnet, the samples were magnetised in a field of 300 mT, far in excess of the required field to saturate the sample. For neutron reflectivity data, a neutron spin flipper was used to record both the spin up and spin down neutrons. The samples were then field-cooled to 250 K in a standard Oxford instruments He flow cryostat at the saturating field, where we performed our initial PNR measurement. Measurements were then carried on in the following order at 5 K, 50 K, 80 K and 150 K without changing the applied field at any point, in order to make the best use of the available counting time. The dimension of the samples was 20 mm x 20 mm on a 0.5 mm thick GGG substrate. The 80 nm and 10 nm thick YIG samples are used for these measurements. It would seem that the room temperature magnetic properties of YIG do not reveal any influence of the Gd-diffused layer but, with decrease in temperature, the magnetic ordering of the Gd-diffused layer takes place which is immediately evident in the magnetisation.

Figure 5.13 shows the spin-polarised neutron refectivity data (left hand column) and spin assymetry curves (right hand column) along with their fits as a function of scattering vector q_z for a 80 nm thick YIG film at 5 K, 50 K, 80 K, 150 K and 250 K. From the reflectivity data we derived the spin asymmetry (SA) using the equation:

$$SA = \frac{I_{\uparrow} - I_{\downarrow}}{I_{\uparrow} + I_{\downarrow}} \tag{5.4}$$

where $I_{\uparrow}$ and $I_{\downarrow}$ refer to the neutron spin reflectivities with orientation parallel or anti-

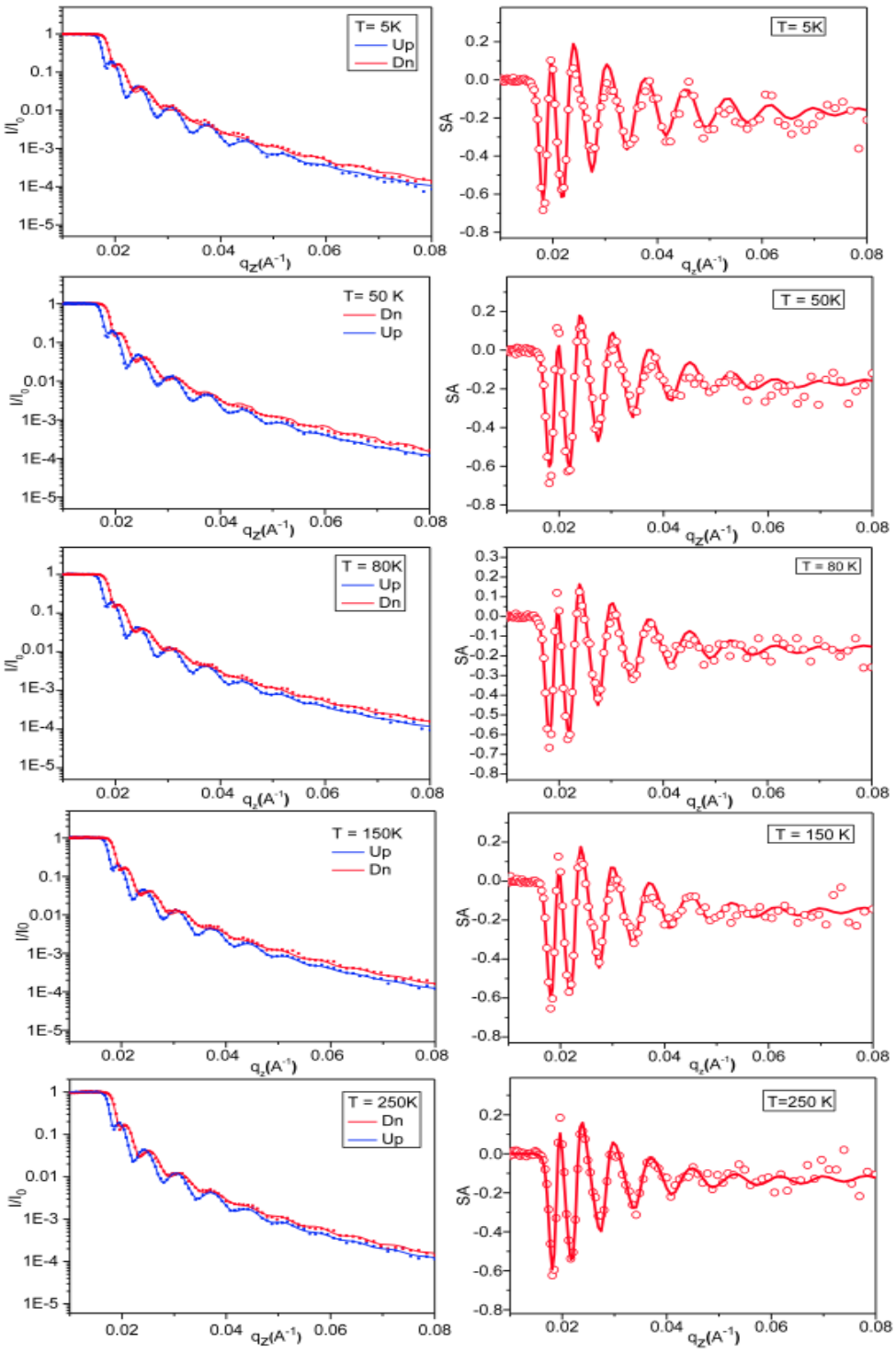

Figure 5.13: *Spin-polarised neutron reflectivity data (left hand column) for a 80 nm-thick YIG film and extracted spin asymmetry data (right hand column) along with their fits as a function of scattering vector q_z at 5 K, 50 K, 80 K, 150 K and 250 K. The solid lines are results from the simulations showing a good fit to the experimental data.*

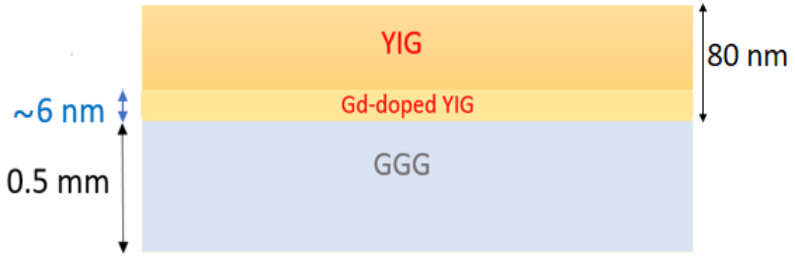

Figure 5.14: *Schematic of a two layer model approach used for fitting the PNR data of 80 nm YIG sample in Gen-X. It consists of Gd-doped YIG region of about 6 nm thick at the YIG/GGG interface.*

parallel to the applied magnetic field, respectively. As spin asymmetry is sensitive to the magnetic component, it represents the reflectivity difference caused by the spin dependent magnetic interaction. The fittings for the reflectivity data and SA are obtained from simulations done by using Gen-X [168]. For the simulations, we approached a two layer model for YIG and Gd-doped YIG near the YIG/GGG interface (figure 5.14). In this model, the roughness of the substrate is about 1.2 nm and then a 6-7 nm thick layer of interdiffusion region (Gd-rich YIG) at the YIG/GGG interface. We note that Gd has a significant neutron absorption cross-section which makes us more sensitive to it. So, we included this absorption to our model to fit the data accurately.

From the PNR model we obtained the scattering length densities and we plotted it as a function of distance for different temperatures in figure 5.15a. The z-axis represents the distance along the vertical direction of the sample, where z = 0 represents the YIG/GGG interface. The areas under the SLD curves were integrated (β_{SLD}) to get the integrated SLD as a function of temperature (figure 5.15b). Since the scattering length densities with magnetic components (ρ_{mag}) is directly proportional to the magnetisation of the sample:

$$\rho_{mag}(z) = C \sum_{i} N_i(z)\mu_i \tag{5.5}$$

where the summation is over each type of atom in the system, N is the in-plane average of the number density, μ is the magnetic moment in Bohr magnetons and C is a

constant. So, the integrated SLD can be converted to a magnetisation (emu/cc) using the relation: $m = \beta_{SLD}/nC$ where m is the magnetisation, n is the atomic number density, and $C = 2.853 \times 10^{-9}$ cm^3/emu [169]. From figure 5.15a, one can see that at 250 K, the SLD near z = 0 indicates a region which is paramagnetic but this region becomes magnetic and orders anti-parallel to the rest of the YIG as we cooled the sample down to 5 K: this is indicated by a negative SLD. The total thickness is given by the Kiessig fringes and the model gives a value of $\sim$ 6 nm for the Gd-diffusion region which again agrees well with our x-ray reflectivity data, the superSTEM and the room temperature magnetic data. Then, we measured the temperature dependence of the magnetisation M(T) on the sample, from 350 K down to 1.8 K using a SQUID-VSM in an applied field of 50 mT, and have analysed these in combination with the PNR data as a function of temperature. The integrated SLD is then plotted together with the independently measured M(T), as shown in figure 5.16. Both these data show a very good agreement. We know that the moment in YIG is a result of the antiferromagnetic superexchange mediated by the O^{2-} between the Fe^{3+} ions on the octahedral (*a* sites) and tetrahedral (*d* sites) sites. This is the strongest of the interactions, so the Gd-doping does not change the Curie temperature of YIG. Gd substitution for Y on the *c* sites and its antiparallel alignment to the net moment of the *a* + *d* sites, leads to magnetization reduction only at low temperature region. This explains the observed PNR results.

In Gd-doped alloys, it has been reported that when Gd concentration exceeds 24%, there is a compensation temperature where the total moment passes through zero, and interestingly, the Gd-YIG system rotates coherently as the compensation temperature is passed [158]. We note that a clear compensation temperature was observed in our YIG/GGG system, for 10 nm YIG sample (figure 5.8a), and the 100 K compensation temperature agrees well with that found for a 40% Gd doped YIG film as shown in ref. [158]. For this 10 nm sample, PNR measurements were done in the same way as for the 80 nm film. But using the same two-layer model approach, it was difficult to fit the PNR data in Gen-X. This is most likely due to the wide Gd-rich diffused region and continuous composition gradient within the sample. Figure 5.17a shows the spin

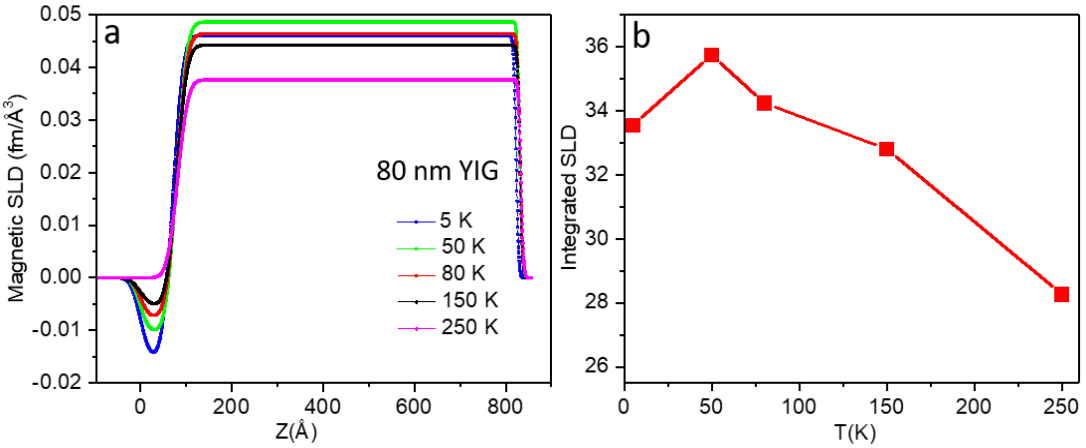

Figure 5.15: *We show (a) the scattering length density (SLD) as a function of distance through the 80 nm sample (z = 0 is the GGG/YIG interface) and temperature. Clearly visible (between 0 and 50 Å) is the increase in the Gd moment ordering antiparallel to the YIG moment as the temperature is reduced from 250 K to 5 K. (b) Integrated SLD as a function of temperature.*

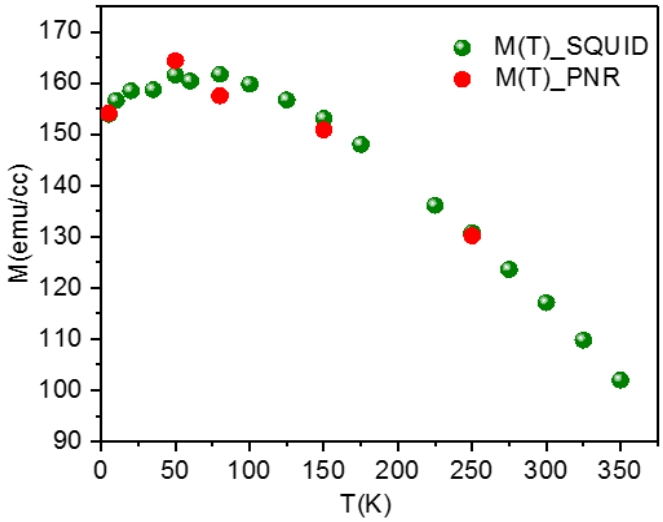

Figure 5.16: *The temperature dependence of the magnetisation for the same 80 nm YIG sample measured by SQUID magnetometry. The points overlaid are the integrated SLD which shows a convincing correlation between the two measurements.*

asymmetry curve for different temperatures for 10 nm YIG.

For each temperature, the amplitude of spin asymmetry (Δ_{SA}) at $q_z \approx 0.047$ Å^{-1}

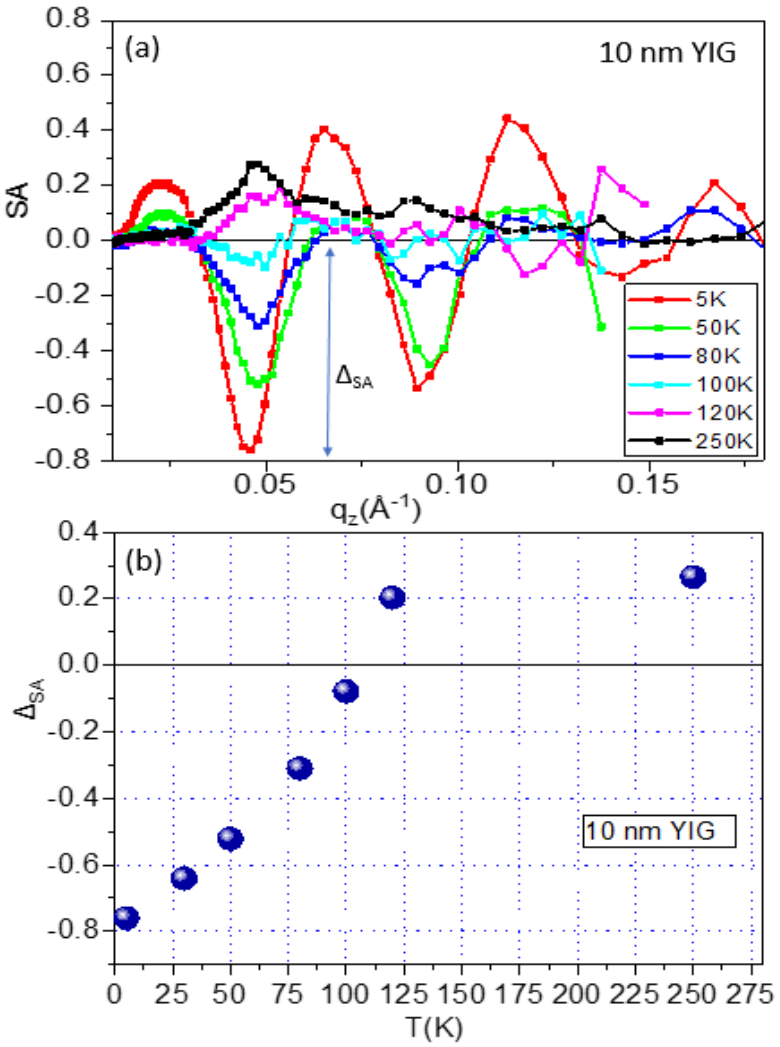

Figure 5.17: *(a) Spin asymmetry plotted as a function of q_z for different temperatures for 10 nm thick YIG film. (b) Amplitude Δ_{SA} (at 0.047 $Å^{-1}$) is plotted as a function of temperature for 10 nm YIG. This shows a transition around 100 K which is consistent with its magnetometry result.*

is extracted and this value Δ_{SA} is plotted as a function of temperature (figure 5.17b). It shows a transition near 100 K, where Δ_{SA} changes from negative to positive value. This gives a quantitative information about the magnetic behaviour and the compensation point of 40% Gd-rich YIG sample. Also, it agrees very well with the independently measured M(T) result for 10 nm YIG. This indicates that below 100 K, inter-

action of neutron magnetic moment with the magnetisation of the sample is different from that above 100 K.

With the information obtained from the PNR results of 80 nm YIG, we developed a mean field model for the magnetisation as function of temperature M(T) for the YIG/GGG system based on two layers: YIG and Gd-rich YIG layer, where:

$$M(T) = M_y B(J_y, z_y) + M_g B(J_g, z_g) \tag{5.6}$$

where B is the Brillouin function, M_y and M_g are the saturation magnetisations of the YIG and Gd-rich YIG layers respectively. z_y and z_g are defined as

$$z_y = \frac{g\mu_B H_y J_y}{k_B T} \left(\frac{t - t_g}{t}\right) M_m(T) \tag{5.7}$$

and

$$z_g = \frac{g\mu_B H_g J_g}{k_B T} \left(\frac{t_g}{t}\right) M_m(T) \tag{5.8}$$

where t is the thickness of the total layer, t_g is the thickness of the Gd-doped region, which we considered to be 6 nm for all samples, H_y and H_g are the Weiss fields for YIG and Gd-doped YIG, and are fitting parameters. J_y and J_g are the spin quantum numbers for the two layers taken to be: $J_y = 5/2$ and $J_g = 7/2$. $M_m(T)$ is the measured value of the magnetisation.

Figure 5.18 shows the temperature dependence of the saturation magnetisation with their fits for different thickness of the YIG. In the left hand column are the M(T) measurements for various thicknesses and the solid line represents the fit using the two-layer mean field model. The right hand column shows the magnetisations for the two individual layers (YIG in red and Gd-doped YIG in green) where a negative sign indicates an antiparallel moment. One can see that the simple two-layer model fits all the data consistently for all samples with a common Gd region of 6 nm. The saturation magnetisation of YIG obtained from the fit are close to the accepted value. We have considered a fixed thickness of 6 nm for Gd-layer, but the behaviour of the Gd-layer varies slightly among the samples, this difference is due to the Weiss field fitting parameter. We have taken a constant thickness of the Gd-layer to maintain

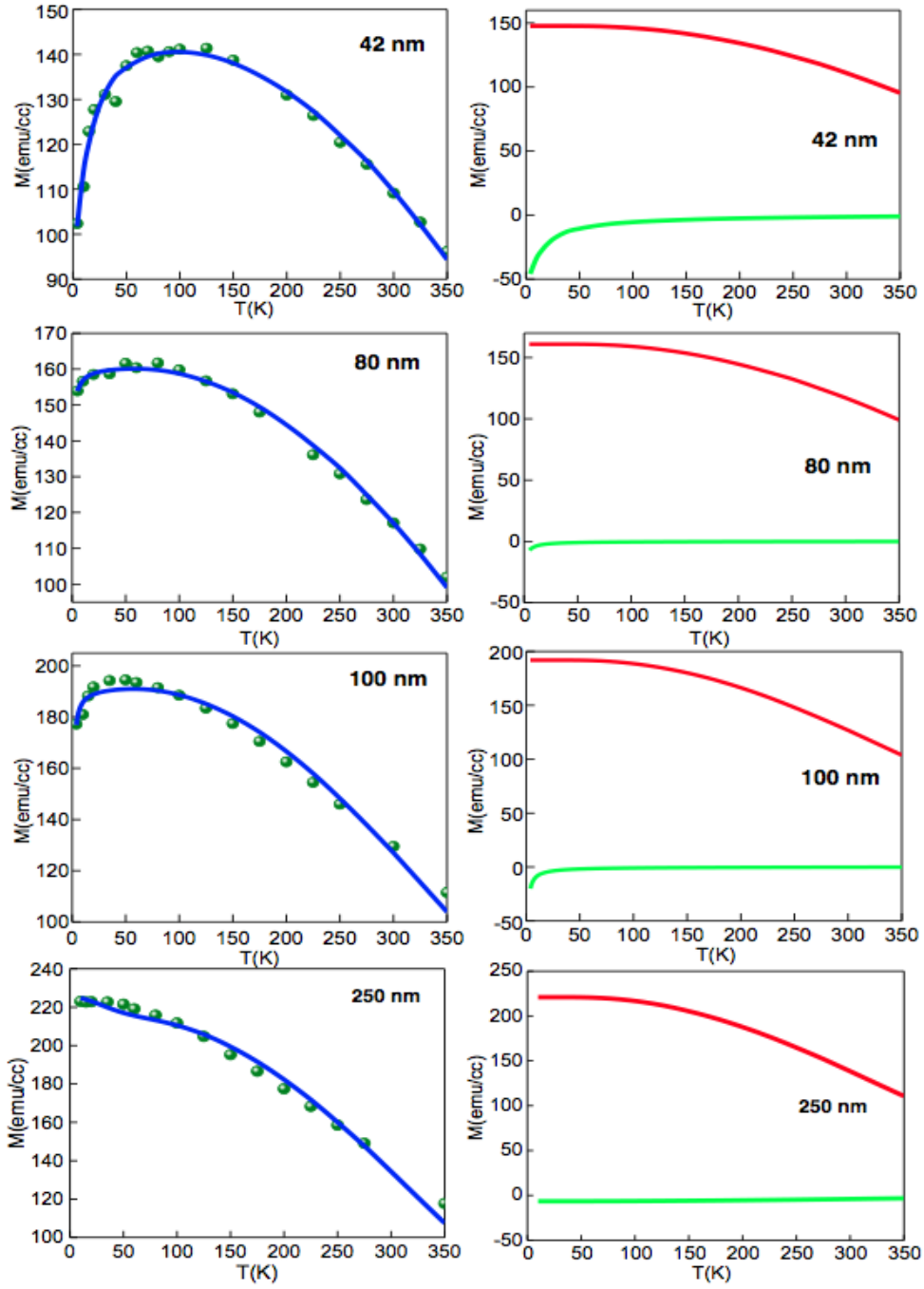

Figure 5.18: *Temperature dependence of magnetisation for a series of YIG film thickness. The left hand column shows the M(T) data where the line is a fitting to the data using a mean field approach. The model uses two magnetic layers: YIG and Gd-doped YIG. The right hand column shows the magnetisation for the individual layers: YIG in red and Gd-doped YIG in green. The negative values for the Gd-doped YIG indicates it is antiparallel to the YIG. M(T) data fitting is done by B.J.Hickey.*

a consistency with the value obtained from the other techniques. We note that for the thickest sample, it is difficult for the fitting model to find an acceptable thickness of Gd-layer as it shows no reduction in M(T) - without this, a single layer fit will satisfy. We were not able to determine the accurate concentration of the elements in the diffusion region. From the diffusion profile of the elements (fig. 4.16c of section 4.5.1), we have assumed that vacancies might be implicated. It is possible that the concentration of vacancies forming after the annealing depends on the thickness of the YIG such that the thinner samples have a higher concentration. Altogether, we can conclude that the correlation between the XRR, STEM, PNR(T) and the magnetometry results is very high indeed.

5.4 Temperature dependence of magnetisation for YIG on YAG

For further verification, we deposited YIG sample of 40 nm-thick on (111) oriented YAG ($Y_3Al_5O_{12}$) substrate and studied the temperature evolution of saturation magnetisation of YIG film. This film was grown on YAG using the same deposition and annealing conditions as for YIG on GGG. The lattice constant of YAG is 12 Å [170] which leads to a lattice mismatch of about 3% and this might result in deteriorating magnetic properties of the YIG films on YAG. YAG is diamagnetic as it does not contain magnetic ions and it can provide nearly temperature independent signal. This will allow easy subtraction of the substrate signal from the measured magnetic moment of the YIG as compared to the paramagnetic, strongly temperature dependent magnetic signal of GGG substrate. This makes YIG film attractive on YAG. We can easily evaluate the low temperature magnetisation data of YIG on YAG as there is no Gd^{3+} ions.

At first, we measured hysteresis loops at different temperatures. We plotted the m(H) curve at T = 20 K, 100 K and 200 K (figure 5.19a,b,c) for YIG/GGG and YIG/YAG on the same graph for each temperature to compare their loops and also

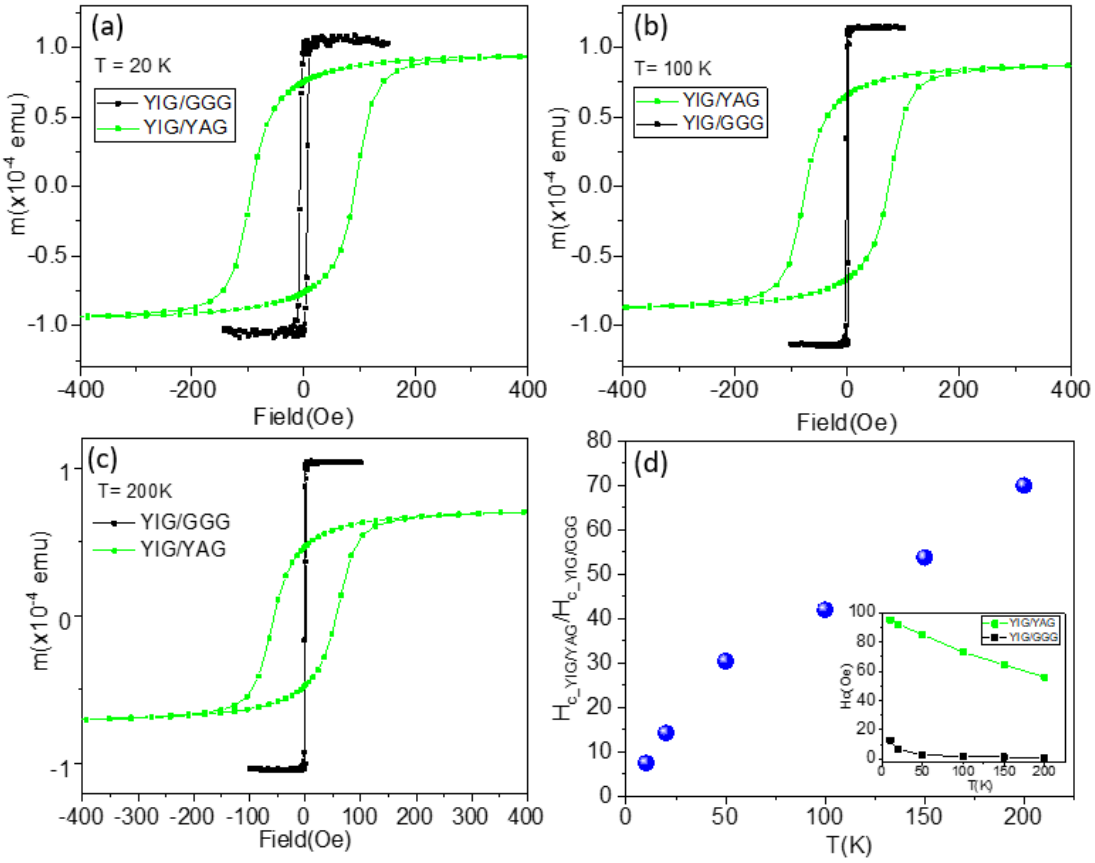

Figure 5.19: *Hysteresis loops as a function of applied field for 40 nm thick YIG film deposited on YAG (green curve) and GGG (black curve) at 20 K (a), 100 K (b) and 200 K (c) respectively. This tells us that YIG films deposited on YAG have higher coercivity compared to those on GGG. (d) Ratio of $H_{c-YIG/YAG}/H_{c-YIG/GGG}$ as a function of temperature showing that it increases with temperature, with 70 times higher coercivity at 200 K for YIG on YAG. Inset shows the $H_c(T)$ for YIG/GGG and YIG/YAG.*

extracted the coercive field in each case. For YIG on YAG, the coercive field is quite high: at 200 K it is about 70 times higher and at 20 K it is 14 times higher than the one obtained for YIG on GGG substrate. The loops are square for YIG on GGG. In figure 5.19d we plotted the ratio of $H_{c-YIG/YAG}$ and $H_{c-YIG/GGG}$ as a function of temperature which increases almost linearly with temperature. The saturation magnetisation obtained for YIG on YAG is low, 98 emu/cc at 200 K, whereas for YIG on GGG, it

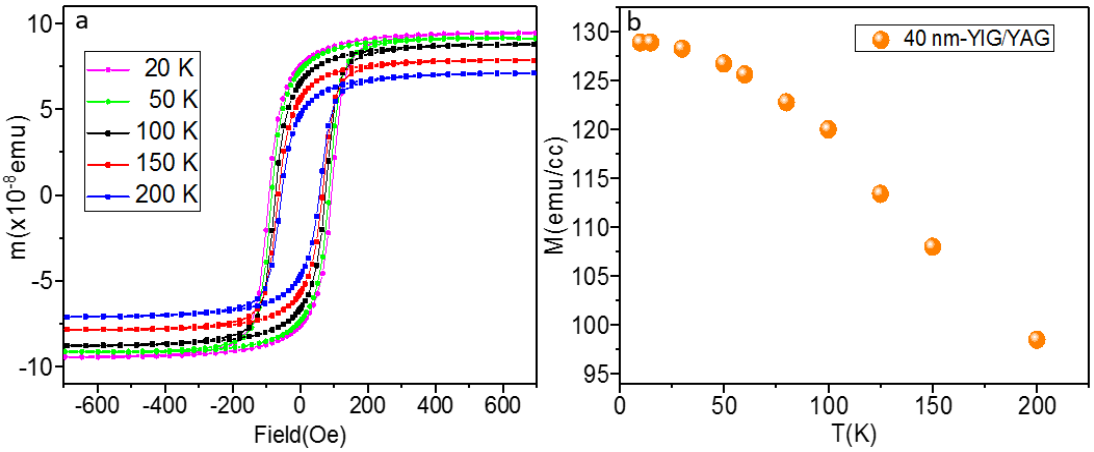

Figure 5.20: *(a) Hysteresis loops as a function of applied field at different temperatures for 40 nm thick YIG film. This shows no background signal from YAG substrate in the net magnetic moment of YIG, because YAG is diamagnetic. (b) Temperature dependence of magnetisation of YIG on YAG showing no downturn of magnetisation at lower temperature.*

was about 125 emu/cc at the same temperature. The polycrystalline nature of YIG on YAG is the most probable reason for the high coercivity and low magnetisation value. We can also attribute high coercive field to the lattice mismatch between YIG and YAG and surface defects in the films. So, in future to grow good quality YIG on YAG, we need to do systematic study for the optimisation of growth conditions and annealing conditions. We measured the temperature dependent magnetisation M(T) for the same 40 nm thick YIG deposited on YAG. The net magnetic moment of YIG has no contribution from the substrate as can be seen in the loops in the wide temperature range (figure 5.20a). Figure 5.20b shows the saturation magnetisation as function of temperature and one can see that there is no reduction of magnetisation at lower temperature. This is obvious as the influence of Gd^{3+} ions are absent in YIG/YAG system.

5.5 Conclusion

In this chapter, we performed a systematic study of the magnetic properties of nm-thick YIG films on the GGG substrate over the wide temperature range. We have adopted a multi-technique approach to investigate the dead layer thickness and low temperature magnetisation suppression. The magnetic properties of YIG on (111) oriented GGG substrate was measured extensively using magnetometry and polarised neutron reflectivity. Measuring the magnetic moment of YIG at low temperatures is quite challenging due to the paramagnetism induced by the Gd^{3+} ions from the GGG substrate, that can easily swamp the magnetic signal from thin YIG films. Our interesting results of YIG on GGG, emphasizing the low-temperature magnetic data highlight the essential role of Gd-diffused interlayer in the temperature dependence of the magnetization of YIG. The results obtained from the room temperature magnetometry show that our YIG films are of high quality with very low coercivity and a saturation magnetisation close to the bulk value (140 emu/cc). We identified a 6 nm thick magnetically dead layer at the YIG/GGG interface. We did the surface cleaning of YIG by Piranha etching to remove organic contamination from the top surface. This contamination is most likely coming from the ex-situ annealing and air exposure. We found that the piranha etching removes the active layer of YIG from the top surface along with the contamination, resulting in a decreased saturation magnetisation of YIG films after etching. Temperature dependence of the magnetisation in an etched YIG sample also confirms the existence of dead layer at the interface. We have also shown that deposition of Pt on YIG in YIG/Pt bilayer films does not alter the magnetisation value of YIG.

The temperature dependence of magnetisation in YIG/GGG system revealed an reduction in magnetisation at low temperature. To complement this result, we performed temperature dependent polarised neutron reflectivity experiment. This gives a very high correlation between the magnetometry (SQUID-VSM) and PNR results. We proposed a simple two-layer model which fits all the M(T) data consistently for different thickness of YIG samples with a common Gd region of 6 nm. Finally, our M(T) results on YIG on YAG substrate which shows no reduction of magnetisation

at low temperature, further confirms the role of Gd^{3+} ions in the YIG/GGG system. The magnetic quality of YIG on YAG deteriorates: low saturation magnetisation and high coercivity. So. it is necessary to optimise the growth and annealing conditions for getting high quality YIG on YAG.

Our most important finding is $\sim$ 6 nm Gd-interdiffusion region at the YIG/GGG interface, which is paramagnetic at room temperature and orders antiparallel to YIG at low temperatures. This interfacial origin of the magnetization suppression affect the properties of YIG and should be taken into account for studies of fundamental magnetic phenomena such as magnetization dynamics, spin pumping effect and STT effect which demands thin films in the region of 10 - 20 nm for YIG-based spintronics devices.

CHAPTER 6

Ferromagnetic resonance properties of nm-thick YIG films

6.1 Introduction

In the magnonics community, researchers are aiming to make pure spin currents as a unique information carrier. For this, YIG is an excellent magnetic material which has been widely used for studying high frequency magnetization dynamics due to its extremely small magnetization damping, 5 x 10^{-5}, high Curie temperature and high chemical stability [35, 40, 171]. Because of its unique properties, in the mid-twentieth century bulk YIG crystal was the standard material for ferromagnetic resonance studies. The emergence of YIG-based spintronic devices requires high quality ultrathin YIG films and understanding of the magneto-dynamic properties in nm-thick YIG films for experiments concerning spin wave propagation. In recent years, YIG/Pt heterostructures have attracted considerable interest. Since YIG is an insulator, direct injection of a spin current from the YIG into the Pt layer is not possible. Spin current injection in the adjacent Pt layer can be possible only by the spin pumping phenomenon, realized through exchange interaction between localized electrons in the YIG film and conduction electrons in the Pt layer. Platinum is the most favourable material due to its high spin-orbit coupling which is necessary for the conversion of spin currents into electrical currents by the ISHE. Spin pumping is an interfacial effect, so good interface quality is necessary to achieve high spin pumping efficiency. It also depends on the spin mixing conductance which can be determined from the Gilbert damping. Spin pumping in a bilayer structure is revealed by the increased Gilbert damping factor, which depends on the temperature and the defects present in a sample [172].

In this work, we investigated the FMR properties and particularly the damping behaviour of RF sputtered nm-thick YIG films using ferromagnetic resonance (FMR) technique. At first we report the thickness dependence of FMR properties for YIG films. We performed temperature dependent FMR measurements in YIG and YIG/Pt samples to extract the behaviour of the Gilbert damping. For the implementation of spin transfer torque (STT) devices using YIG, it is important to understand the nature of the torque acting on the YIG induced by the charge current in metal layers in YIG/metal

system. So, we performed current-induced FMR (CI-FMR) experiment in YIG/metal bilayer structures to characterise and quantify the current induced torque. In this work, we used C_{60} molecules, due to its structural simplicity and robustness to make YIG/C_{60} heterostructures. It has been found that C_{60} has higher spin-orbit interaction due to the curvature of the molecule compared to other carbon allotropes [173]. We investigated the dynamic properties of YIG/C_{60} structures to find the effect of C_{60} molecules on the damping of YIG. With C_{60} on top of YIG, we expect to realise spin pumping from YIG into the molecules. We also performed PNR-FMR experiments in which we combined the FMR technique with polarised neutron reflectivity, to detect spin pumping in YIG/Pt manifested as spin asymmetry.

6.2 Thickness dependent FMR properties

We performed in-plane FMR measurements for different thicknesses of YIG nano films. The samples used for the FMR measurements are about 4 x 4 mm^2. The magnetization dynamics are excited by applying an alternating microwave field oriented perpendicular to the external in-plane bias field. At ferromagnetic resonance condition, the dependence of ferromagnetic resonance frequency on the field follows the Kittel formula [160] :

$$f = (\mu_0\gamma/2\pi)\sqrt{H_{res}(H_{res} + M_{eff})} \tag{6.1}$$

where H_{res} is the magnetic field at the resonance condition for a given fixed frequency and μ_0 is the vacuum permeability. By fitting the field dependence of the resonance frequency with the Kittel formula we can obtain the value of gyromagnetic ratio γ and the effective magnetization M_{eff} for our nm thick YIG films. The effective magnetization is the sum of saturation magnetization M_s and the anisotropy field H_{ani}. Therefore, the effective magnetization takes the out-of-plane anisotropy into account. We can calculate the anisotropy constant K_{u1} by using the relation [86]:

$$K_{u1} = \frac{\mu_0 H_{ani} M_s}{2} = \frac{\mu_0 (M_s - M_{eff}) M_s}{2} \tag{6.2}$$

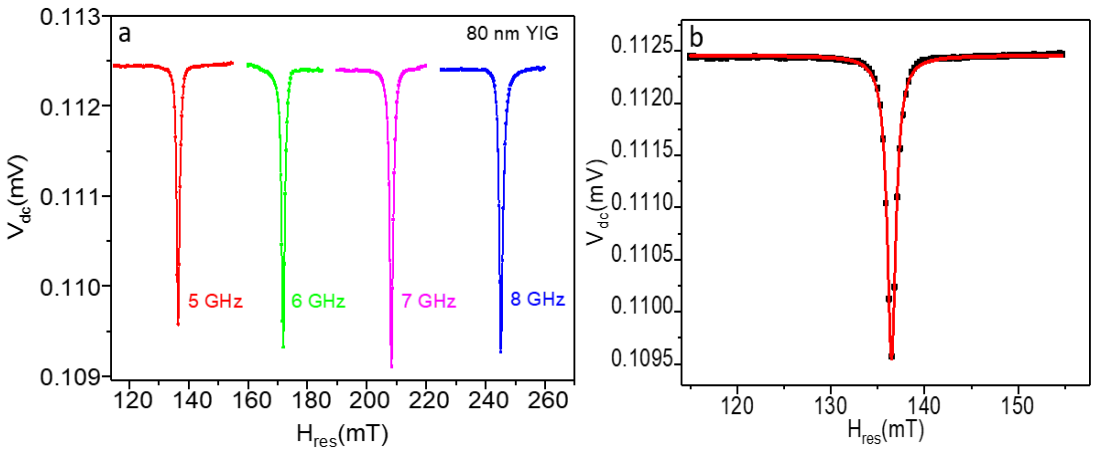

Figure 6.1: *(a) Ferromagnetic resonance spectra of the absorption for 80 nm YIG film at frequencies of 5, 6, 7 and 8 GHz measured at room temperature using lock-in detection technique. (b) A typical FMR data at 5 GHz showing the Lorentzian absorption line with its fit which gives resonance field H_{res} = 136.5 mT and linewidth of 1 mT.*

The Gilbert damping parameter α can be estimated from the frequency dependence of FMR linewidth dH by using the relation:

$$dH = \frac{4\pi\alpha f}{\gamma\mu_0} \tag{6.3}$$

Figure 6.1a shows the typical FMR spectra measured at different frequency (5-8 GHz) using lock-in detection (section 3.8), showing the Lorentzian absorption line and a typical FMR data at 5 GHz is shown with its Lorentzian fit (figure 6.1b). Data were measured at room temperature. Dependence of the FMR frequency on the resonance field for a 80 nm-thick sample is shown in figure 6.2a and the solid line is a Kittel fit to the experimental data. From this we extracted the value of gyromagnetic ratio and the effective magnetization. Figure 6.2b shows the evolution of the FMR linewidth (dH) as a function of frequency. From the linear fit of the frequency dependence of the FMR linewidth we can extract the value of Gilbert damping parameter of the film.

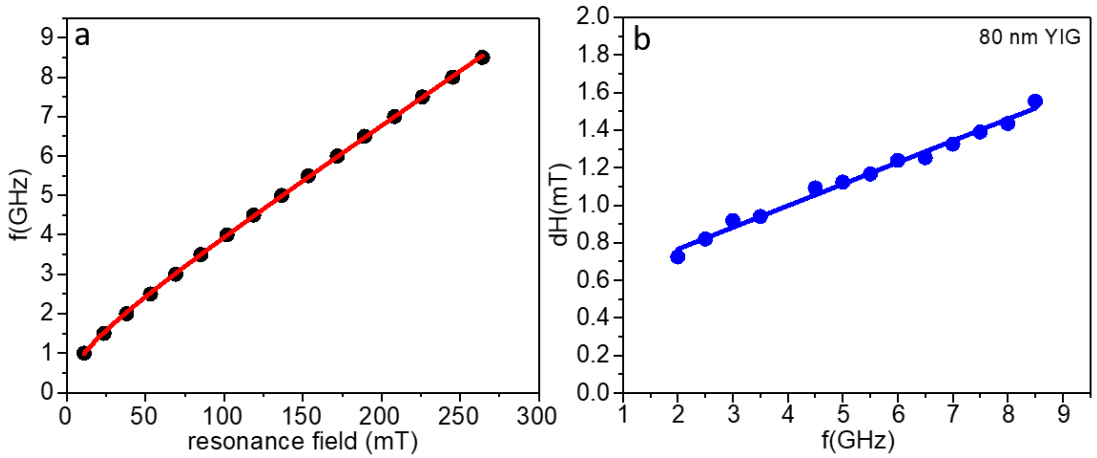

Figure 6.2: *(a) Dependence of the ferromagnetic resonance frequency on the resonance field for a 80 nm-thick sample, the solid line (red curve) is a Kittel fit to the experimental data. This gives a standard value of gyromagnetic ratio 27.2 GHz/T and* $\mu_0 M_{eff}$ *= 110* $\pm$ *2 emu/cc. (b) FMR linewidth as a function of frequency measured at room temperature. The solid lines are linear fits to the data. Damping extracted from the slope of the linear fit is 1.61 x* 10^{-3}.

The Gilbert damping should be proportional to the linewidth while the zero-frequency offset dH_0 along the y-axis is related to the extrinsic contributions to damping, such as film inhomogeneities and two-magnon scattering.

The results of FMR measurements for different YIG thicknesses are summarised in Table 6.1. These samples were grown from the new target (Target-B). Here dH_0, the zero-frequency intercept of the FMR linewidth is extracted from the linear fits to the data (fig. 6.2b), and the damping α is extracted from the slope of the linear fits. The inhomogenous linewidth broadening dH_0 of our films varies between 4 to 6 Oe, which is comparable to the value of 3 to 6 Oe for 19 nm to 49 nm thick YIG films as reported in the reference [174]. The linewidth obtained for a set of RF sputtered YIG samples of 83 nm and 96 nm thick is in the range of 4 to 6 Oe, reported in ref. [64]. The values obtained for M_{eff} is lower than the saturation magnetization for the bulk YIG (140 emu/cc).

We plotted the thickness dependence of Gilbert damping parameter of our nm-

Thickness (nm)	γ (GHz/T)	dH_0 (mT)	$\mu_0 M_{eff}$ (emu/cc)	α	K_{ul} (kJ/m^3)
16	27.6 ± 0.2	0.6 ± 0.03	95 ± 3	$2.80 \pm 0.4 \times 10^{-3}$	4.3
24	27.5 ± 0.2	0.6 ± 0.01	102 ± 3	$2.40 \pm 0.3 \times 10^{-3}$	3.7
28	27.6 ± 0.2	0.5 ± 0.02	109 ± 3	$2.08 \pm 0.5 \times 10^{-3}$	3.1
38	27.2 ± 0.3	0.5 ± 0.06	111 ± 4	$1.92 \pm 0.1 \times 10^{-3}$	2.8
80	27.2 ± 0.1	0.5 ± 0.02	110 ± 2	$1.61 \pm 0.05 \times 10^{-3}$	2.9
125	27.7 ± 0.3	0.5 ± 0.03	115 ± 3	$1.48 \pm 0.07 \times 10^{-3}$	2.5

Table 6.1: Magnetic parameters of the YIG obtained from FMR

thick YIG films which is shown in figure 6.3. The largest damping 2.8 x 10^{-3} is observed in a 16 nm thick YIG film. With increasing film thickness the damping decreases, down to 1.48 x 10^{-3} for 125 nm thick YIG. This behavior has been attributed to two-magnon scattering at the film surfaces and interfaces that becomes increasingly dominant with decrease in film thickness [175, 176]. It has been reported that films with thickness above 1 µm (bulk YIG) can reach values as low as 6.7 x 10^{-5} [177]. Recent studies have also shown that recrystallization of amorphous YIG by annealing in oxygen atmosphere leads to ultra low damping YIG which gives α = 7.35 x 10^{-5} for 20 nm PLD grown YIG films [62]. Our α value for 16 nm YIG agrees well with the value reported in [85], where a PLD-grown 20 nm YIG sample has a damping of (2.169 $\pm$ 0.069) x 10^{-3}. From the comparison of our FMR results, we found that the samples deposited from the Target-A showed lower damping (section 6.3, [174]) as compared to the samples grown from the Target-B. This higher damping is possibly due to the contributions from nanoscale inhomogeneities in the samples deposited from the Target-B.

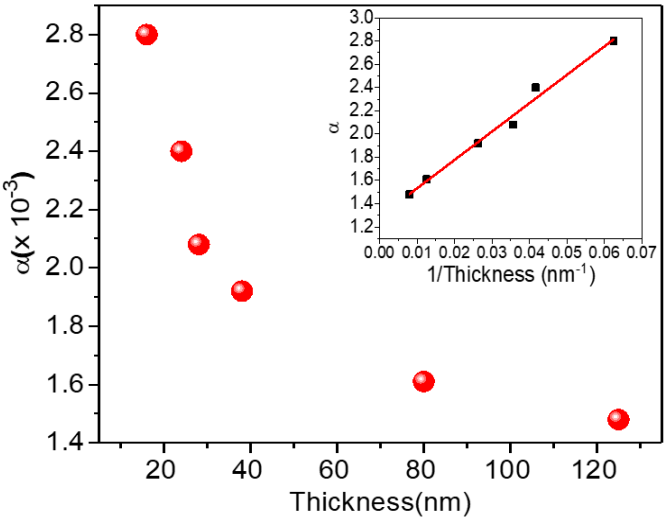

Figure 6.3: *Gilbert damping parameter of nanometre thick YIG films as a function of film thickness. This shows that damping decreases with increase in film thickness. The largest damping is observed for 16 nm thick film, which is about 2.8 x* 10^{-3}. *Inset shows that* α *is proportional to 1/Thickness.*

6.3 Temperature dependence of Gilbert damping in YIG and YIG/Pt

In this study, ferromagnetic resonance properties were measured using coplanar waveguide with frequency band (1-20 GHz) by applying in-plane external magnetic field. The measurements were carried out in the cryogenics system in the temperature range 20 K to 300 K. We used 40 nm YIG and YIG (40 nm)/Pt (10 nm) bilayer samples for our measurements. This 40 nm thick film showed a RMS surface roughness of about 2 Å with (111) crystalline orientation. Before doing the FMR in these films, we measured the saturation magnetization M_s at room temperature and also its temperature dependence using SQUID magnetometry (figure 5.10b chapter 5).

The inset of figure 6.4 shows the FMR profile of the 40 nm thick YIG sample obtained at 9 GHz at 300 K and the solid curve shows the fit to the derivative of Lorentzian function. In the FMR profile, sometimes we also observed more than a

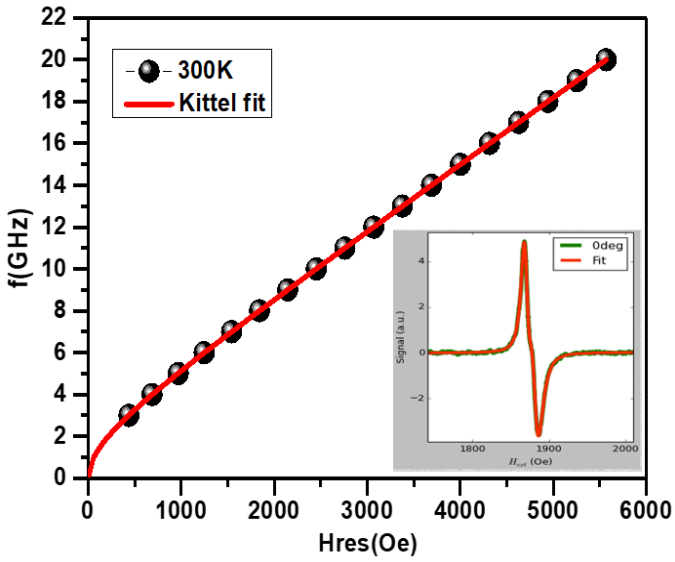

Figure 6.4: *Dependence of the ferromagnetic resonance frequency on the resonance field for a 40 nm thick YIG sample. The fitted line (red curve) is obtained by using the Kittel formula. The inset shows a typical FMR lineshape at 9 GHz thus showing the derivative of the Lorentzian absorption line.*

single absorption peak which can be attributed to the standing spin wave modes of the ultra low damping YIG layers [62]. In order to fit such a FMR profile, one needs to take the superposition of a few closely separated Lorentzian lines. Fitting of the field dependence of the FMR resonance frequencies (figure 6.4) using the Kittel equation 6.1, gives the gyromagnetic ratio, γ = 28 GHz/T. From the slope of the linear fit to the linewidth versus resonance frequencies (figure 6.5), we can extract the damping parameters (using equation 6.3) for each temperature. For a 40 nm YIG film at 300 K, the FMR linewidth is about 6 Oe at 9 GHz with a damping constant of (5.4 $\pm$ 0.2) x 10^{-4}. At 100 K, the damping is increased by a factor of 3.8. We have observed the same effect in YIG/Pt samples, when the temperature drops from 300 K to 100 K, the damping parameter increased by 2.5 times: at 300 K, α = (6.08 $\pm$ 0.1) x 10^{-3} and at 100 K, α = (15.2 $\pm$ 0.2) x 10^{-3}. Damping in our films is significantly smaller than that of metallic films of similar thickness. Our FMR linewidth is comparable to the value

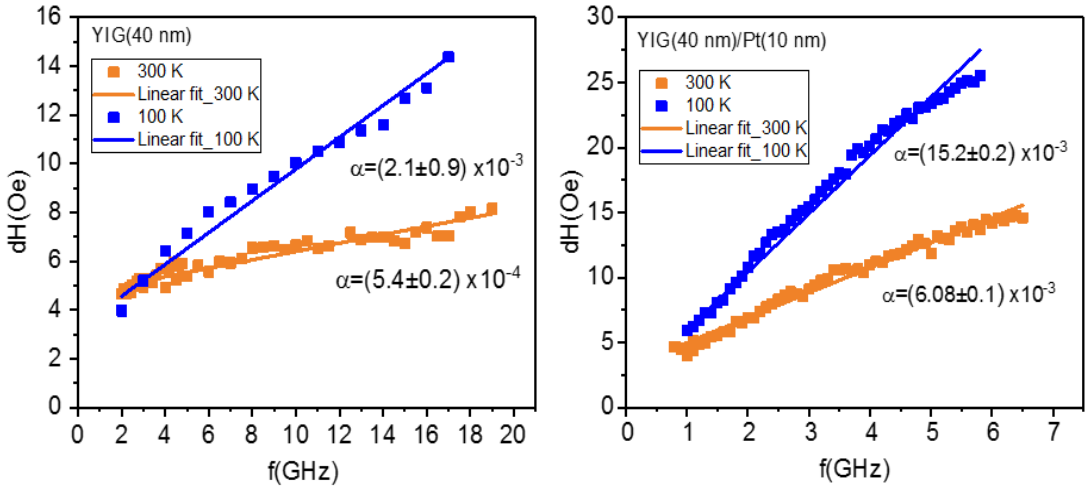

Figure 6.5: *Frequency dependence of FMR absorption linewidth for 40 nm YIG (a) and YIG (40 nm)/Pt (10 nm) (b) samples measured at 300 K and 100 K. The solid straight lines are linear fits to the data from which damping constant α is obtained. At 300 K, for bare YIG sample α_0 = (5.4 $\pm$ 0.2) x 10^{-4} and for YIG/Pt sample α_{Pt} = (6.08 $\pm$ 0.1) x 10^{-3}. This illustrates spin pumping effect in YIG/Pt.*

reported in reference [65] for two 20 nm thick films deposited by off-axis sputtering, which is about 7.4 Oe and 11.7 Oe. It has been reported that 10 nm thick film has a FMR linewidth of about 6.6 Oe at 10 GHz and a damping constant of 10.3 x 10^{-4} [63]. Magnetization dynamics in thin films is no longer a highly coherent process because it depends on the surface and interface roughness, so it was necessary to check the surface roughness of our films. For our smooth films, a linear dependence of the FMR linewidths with frequency (figure 6.5a,b) at temperatures 100 K and 300 K indicates the absence of two-magnon scattering [175, 176, 178]. Two-magnon scattering is caused by defects, contributes to the extrinsic damping and the increase linewidth in thin films. From figure 6.5, we found that the linewidth has a linear frequency dependency with an extrapolation for zero-frequency, which gives a very small non-zero linewidth dH_0 (nearly 3 Oe). This small value of dH_0 is related to the long range inhomogeneties present in YIG films as mentioned earlier. The magnitude of dH_0 also determines the film quality and for the best samples it approaches to zero.

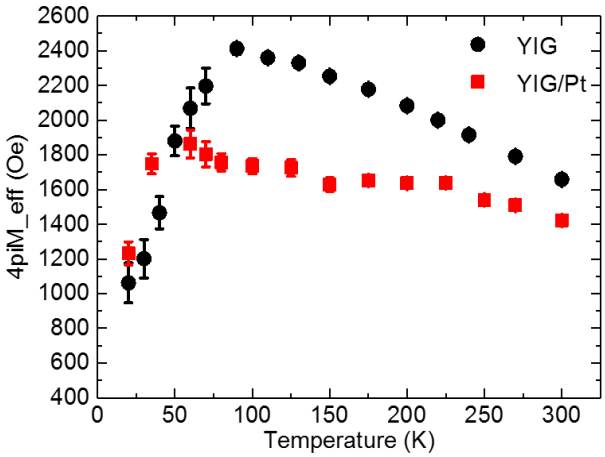

Figure 6.6: *Effective magnetization as a function of temperature for YIG (40 nm) (black dots) and YIG(40 nm)/Pt(10 nm) (red squares) samples. The value of effective magnetization is extracted from the Kittel fit of FMR data at each temperature. This also shows a downturn in effective magnetization at lower temperatures.*

We noticed that the effective magnetization in YIG shows a decrease with decrease in temperature, it started reducing after 100 K (figure 6.6), which agrees with the results of temperature dependence saturation magnetization M(T) SQUID data (figure 5.10b). These behaviour can be attributed to the anti-parallel alignment of the magnetic moment in the Gd-doped YIG layer near the YIG/GGG interface, as explained in chapter 5. For YIG/Pt, M_{eff}(T) also showed a reduction in magnetization but below 60 K. The value of M_{eff} in YIG/Pt is lower than that of YIG sample between 60 K to 300 K, which is in contrast to the M(T) data. This difference is not clearly understood, so it requires further investigation. It might be possible that there is a spin transfer by an induced eddy current which is affecting the magnetization dynamics in YIG. We should repeat the measurements on YIG/Pt samples by varying the YIG thicknesses. The temperature dependent FMR measurements is done in collaboration with University of Regensburg.

In figure 6.7, we plotted the temperature dependence of the Gilbert damping factor α for YIG (40 nm) and YIG(40 nm)/Pt(10 nm) samples. From this we observed that the

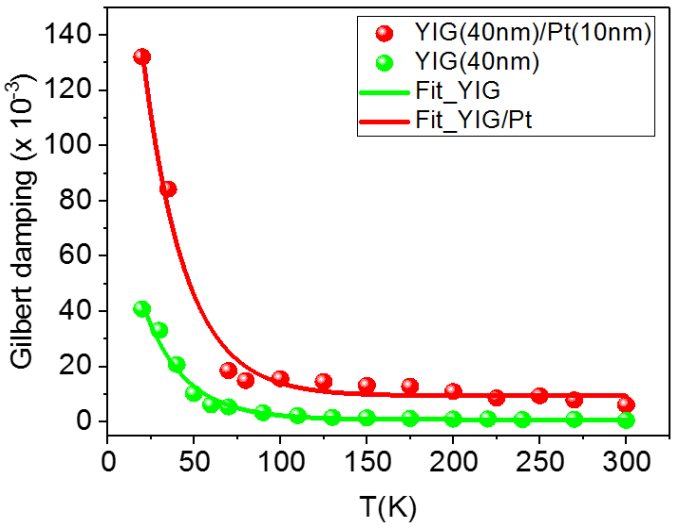

Figure 6.7: *Temperature dependence of Gilbert damping parameter in YIG (green curve) and YIG/Pt (red curve) thin films in the temperature range 20 K - 300 K. It shows an exponential decay with temperature with decaying constant of about 24 for YIG and YIG/Pt samples.*

damping shows a steep rise at low temperature and decays exponentially with increase in temperature. The $\alpha(T)$ data is fitted with an exponential decaying function given by:

$$\alpha(T) = A\exp(-T/t_1) \tag{6.4}$$

where t_1 is the decaying constant and A is the value of α at T = 0 K. For YIG and YIG/Pt, the value of t_1 is about 24. From the fitting we obtained A = 0.09 and 0.28 for YIG and YIG/Pt sample, respectively. This shows that the value of α(T = 0) in YIG/Pt is about 3 times greater than that of YIG, indicating the spin pumping in the Pt layer. The damping in YIG is increased by a factor of 75 as the temperature is decreased from 300 K to 20 K whereas it increased by a factor of 22 in YIG/Pt sample. This increase in Gilbert damping at low-temperature can be attributed to the slow relaxation mechanisms by the rare-earth impurities which may be introduced in the samples from the target during the growth. The Gd ions which have been diffused during the high temperature annealing may also affect the magnetization dynamics of bare YIG at low

temperature. There is another possibility of the presence of Fe^{2+} as impurities which might have been incorporated during the YIG growth. In 1960s, researchers reported an increase in linewidth in bulk YIG samples at low temperature due to the impurity relaxation mechanisms [71, 179–184]. Recently, the increase in linewidth at low temperature has also been observed in 15 nm YIG film deposited by off-axis sputtering [185]. But it is not universal as Haidar *et al.* have observed an increase in damping coefficient in PLD-grown YIG films (30-170 nm) that increases by approximately a factor of 2 as the temperature increases from 8 K to room temperature [58]. According to them, this temperature dependence is due to the films itself which may consist of rare-earth ions due to the target impurities. From the results in our nm-thick YIG samples, we can conclude that low temperature experiments in thin YIG films require very high purity material and so there is always a scope for the optimization of the growth and annealing conditions.

For the YIG/Pt thin film, the effective damping parameter is greater than the damping of bare YIG film. This is due to the spin pumping from the magnetisation dynamics in the YIG to the normal metal Pt. At 300 K, for the bare YIG sample, damping factor α_0 = (5.4 $\pm$ 0.2) x 10^{-4} whereas for Pt (10 nm) covered YIG sample, α_{Pt} = (6.08 $\pm$ 0.1) x 10^{-3}. The spin mixing conductance $g^{\uparrow\downarrow}$ is related to the change of the Gilbert damping, $\Delta\alpha$ = α_{Pt} - α_0 as

$$g^{\uparrow\downarrow} = \frac{4\pi M_s d \Delta\alpha}{g\mu_B} \tag{6.5}$$

Taking d = 40 nm as thickness of YIG, we obtained spin mixing conductance, $g^{\uparrow\downarrow}$ = (1.6 $\pm$ 0.3) x 10^{19} m^{-2} for this particular sample. Our spin-mixing conductance is three orders of magnitude greater than the one reported for YIG(1.3 μm)/Pt(10 nm) ($g^{\uparrow\downarrow}$ = 3 x 10^{16} m^{-2}) system in ref.[35], in which YIG was deposited by liquid phase epitaxy. It has been found that the spin mixing conductance lies in the range of 5 x 10^{18} m^{-2} to 15 x 10^{18} m^{-2} for a series of 20 nm YIG/Pt bilayer samples with varying Pt thicknesses [186]. Lustikova *et al.* has reported a value of (2.0 $\pm$ 0.2) x 10^{18} m^{-2} for RF sputtered YIG(96 nm)/Pt(14 nm) sample [64], so our value is greater by

one order of magnitude. Our $g^{\uparrow\downarrow}$ value is smaller compared to 3.43 x 10^{19} m^{-2} for YIG(2.1 μm)/Pt(10 nm) system where the YIG surface was treated with a combination of piranha etching and O^+/Ar^+ plasma [51]. This surface treatment removes the water as well as dirt, and also the organic contamination from the sample surface. In this work they have shown a strong dependence of the spin pumping efficiency on the interface condition of YIG/Pt bilayer films. The maximum value is reported in ref.[53] for YIG (8 μm)/Pt(8 nm) sample where $g^{\uparrow\downarrow}$ = 4.8 x 10^{20} m^{-2}. In future, we should consider the surface processing of YIG before Pt deposition to get better interface quality for the realization of efficient spin pumping devices.

6.4 Current induced FMR in YIG/Pt bilayer

In this section, our aim is to investigate and quantify the current induced torque in YIG/Pt bilayer structures by using current induced FMR (CI-FMR). Due to the spin Hall effect (section 2.6), an oscillating charge current applied to the metal layer can be converted to a transverse spin current, which can manipulate the magnetization dynamics in the magnetic insulator by an oscillating spin transfer torque (STT). The charge current in the metal layer generates the Oersted field which also contributes in driving the magnetization precession. We applied a microwave current in the metal attached to our YIG layer and an in plane external magnetic field. At resonance, an output DC voltage is generated simultaneously due to the spin rectification and spin pumping mechanisms. From the lineshape and symmetry of the DC voltage we understood the kind of the torque acting on the YIG. The lineshape and the symmetry of the resonance in the DC voltage depend on the driving mechanisms of magnetization precession and how the DC voltage is generated, which we discussed in section 2.5.

For CI-FMR experiment we used YIG/Pt(4.2 nm) bilayer structures with different YIG thickness. By using optical lithography and argon ion milling, we patterned our samples into 5 x 50 μm^2 bars. To make the contact electrodes a layer of 5 nm Cr/50 nm Au was evaporated. For the measurements, each bar was placed on a low-loss

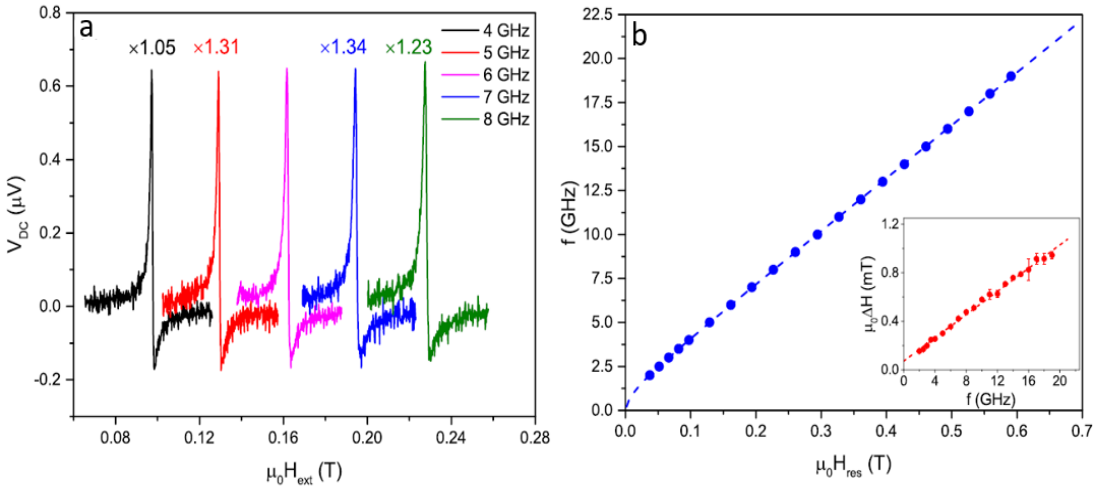

Figure 6.8: *(a) FMR spectra of CI-FMR at 4 - 8 GHz is Lorentzian consisting of symmetric and antisymmetric components. (b) Resonance frequency f as a function of the resonant field $\mu_0 H_{res}$, fitted with in-plane Kittel's formula (dashed line) from which we obtained M_{eff} = 69 ± 3 kA/m and γ_{eff} = 30.0 ± 0.1 GHz/T. Inset shows the frequency dependence of the FMR linewidth and from the slope we calculated α_{eff} = (1.41 ± 0.02) x 10^{-3} [86].*

dielectric circuit board and connected to a microstrip transmission line. An in-plane external magnetic field H_{ext} was swept at an angle θ with respect to the bar. We used a bias-tee to measure the output DC voltage across the bar at the same time as the input microwave power.

Figure 6.8a shows the spectra of current induced FMR signal for YIG (14.8 nm)/Pt (4.2 nm) sample measured at θ = 45°. The resonance signals have a Lorentzian lineshape with symmetric and anti-symmetric components. Figure 6.8b shows the frequency dependence of resonance field, which when fitted by the Kittel formula gives M_{eff} and $\gamma_{eff}/2\pi$ of 69 ± 3 kA/m and 30.0 ± 0.1 GHz/T, respectively. The inset of figure 6.8b shows the linear dependence of the linewidth as a function of resonance frequency. From the slope of the curve, we have calculated α_{eff} = (1.41 ± 0.02) x 10^{-3} for this particular sample.

Next we analysed the angle dependence of the symmetric V_{sym} and the antisymmetric V_{asy} components of the resonance signal in order to characterize the current-

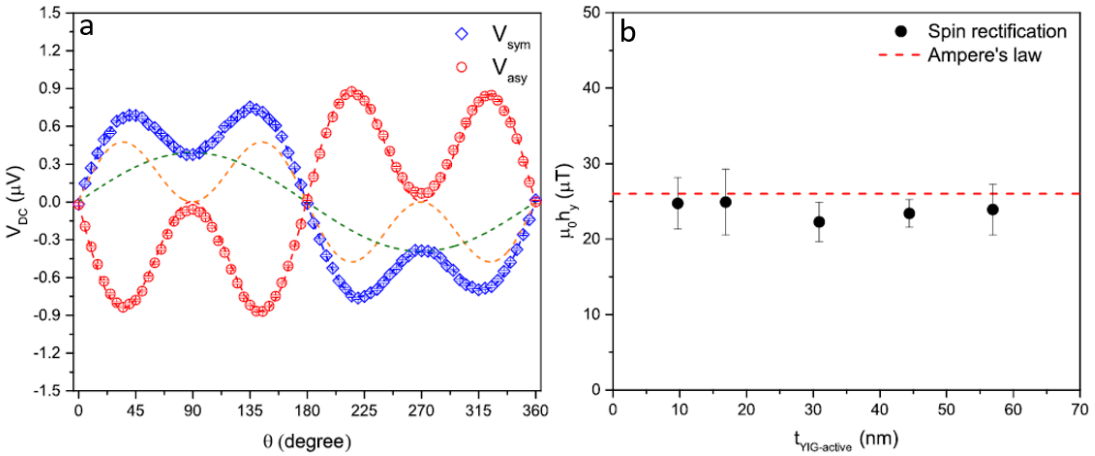

Figure 6.9: *Angular dependence of the symmetric part V_{sym} (blue) and anti-symmetric part V_{asy} (red) from YIG(14.8 nm)/Pt(4.2 nm) at 8 GHz. Dashed lines represents fitting results, where V_{asy} is fitted by sin2θcosθ, while V_{sym} is fitted by a sinθ term (green) in addition to the sin2θcosθ term (orange). (b) Oersted field $\mu_0 h_{Oe}$ (black dot) calculated from V_{asy} and Ampere's law (red dashed line) for each YIG/Pt sample, normalized to j_c=10^{10} A/m^2 [86].*

induced torque, shown in figure 6.9a. The V_{sym} curve is fitted by a function which is the sum of a sin2θcosθ term (orange dash) and a sinθ (green dash) term, represented as $V_{sym-\sin 2\theta \cos\theta}$ and $V_{sym-\sin\theta}$, respectively. The fitting of V_{asy} curve is done using a $-\sin 2\theta \cos\theta$ function (red dash) which agrees with a resonance condition driven by the Oersted field and detected by spin-rectification. We have extracted the value of effective field by analysing V_{asy} (using Eq. 2.44), responsible for generating the torque in each sample. We then compared this value of the effective field with the Oersted field determined from the Ampere's law using the relation: $\mu_0 h_{Oe} = \mu_0 j_c t_{Pt}/2 \approx 26$ μT, where $j_c = 10^{10}$ A/m^2 is the current density and t_{Pt} is the thickness of the Pt layer. We found a good agreement between the two values which allows us to confirm that the field-like torque is mainly due to the Oersted field (figure 6.9b) [86].

To find out the main driving mechanism, we compared the value of $V_{sym-\sin 2\theta \cos\theta}$ and V_{asy} and plotted the ratio $V_{sym-\sin 2\theta \cos\theta}/V_{asy}$ for each Pt/YIG sample as a function of $1/\alpha_{eff}$ (figure 6.10) which shows a linear dependence. From the summary of

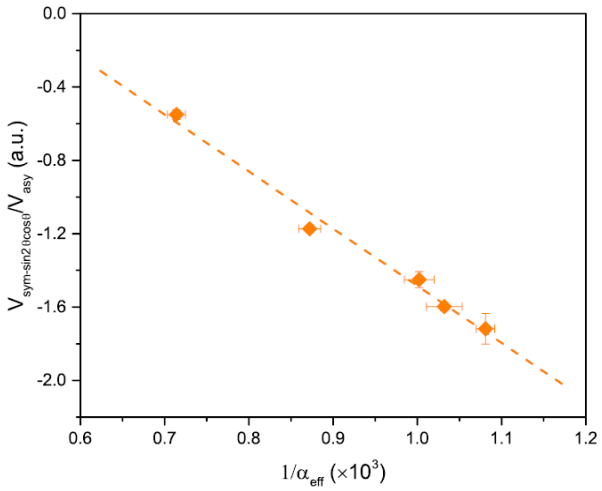

Figure 6.10: *Plot of the ratio $V_{sym-\sin 2\theta \cos\theta}/V_{asy}$ as a function of $1/\alpha_{eff}$, measured from the YIG/Pt samples at 8 GHz. The dashed line represents the linear fitting [86].*

resonance DC signal components (Table II of reference [86]), one can see that only $|V_{Oe-SP}/V_{Oe-SR}|$ is proportional to $1/\alpha_{eff}$. From this, we can say that $V_{sym-\sin 2\theta \cos\theta}$ can be mainly attributed to the spin pumping effect driven by the Oersted field. Also this result shows that V_{sym} and V_{asy} are of opposite sign which is different from the Co/Pt [187] and Py/Pt [188, 189] CI-FMR results where STT plays the dominating role to produce the rectification signal, and V_{sym} and V_{asy} are comparable with the same sign. So in our case this is an indication that $V_{sym-\sin 2\theta \cos\theta}$ is mainly dominated by the spin pumping mechanism driven by the Oersted field.

Further we carried out the angular dependence CI-FMR in YIG(80 nm)/Ta(5 nm) sample. We found that V_{sym} changes its sign compared with the YIG/Pt sample whereas the sign of V_{asy} remains unchanged. This change in the V_{sym} sign is related with the opposite sign of the spin-pumping, resulting from the opposite value of the spin-Hall angle of Ta compared with Pt [190, 191]. The sign of V_{asy} does not depend on the sign of the spin-Hall angle of the attached metal layer, which gives further confirmation that the Oersted field plays the dominating role in driving the magnetization dynamics in our YIG/Pt samples. We presented this work in detail in reference [86]. Our results confirmed that the Oersted field dominates over field-like STT in driving

the magnetization dynamics. This work is done in collaboration with the microelectronics group, University of Cambridge.

6.5 PNR-FMR experiment in YIG/Pt

We performed PNR-FMR experiment in polREF at ISIS in Rutherford Appleton laboratory in Oxford. Using polarised neutron reflectivity along with FMR measurements, we attempt to detect spin pumping in YIG/Pt bilayer structure, manifested as spin asymmetry in the reflectivity. Here we measured neutron reflectivity at on and off-resonance ferromagnetic conditions to identify whether the spin pumping in YIG/Pt has any effect on the neutron reflectivity measurement. For that we measured reflectivity spectrum of YIG(80 nm)/Pt(4 nm), first at on resonance condition which we found around 1 GHz with an in-plane applied field of 10 mT (-0.5 A). Then we set the frequency to 3 GHz to measure the reflectivity spectrum at off-resonance condition. We

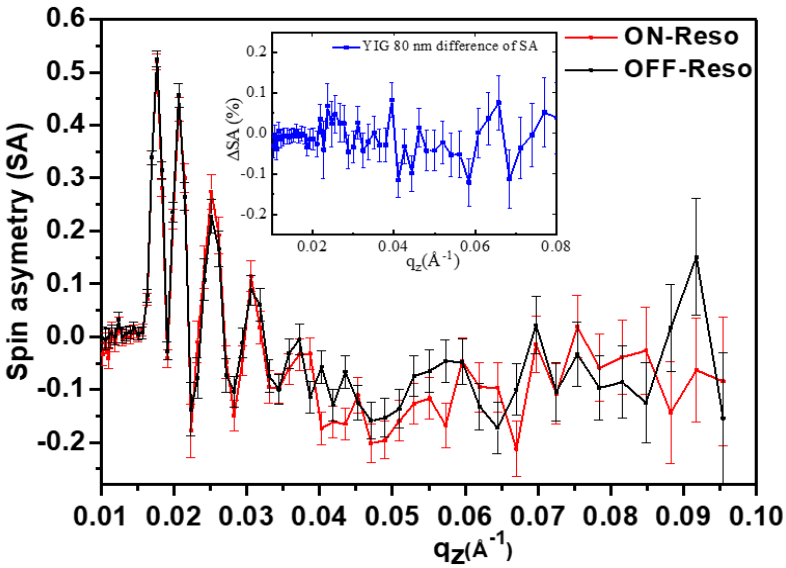

Figure 6.11: *Spin asymmetry (SA) of YIG (80 nm)/Pt (4 nm) at on-resonance (red curve) and off-resonance (black) condition. It shows a very small change in spin asymmetry between on and off-resonance condition, the difference $\Delta SA(\%)$ is plotted in the Inset.*

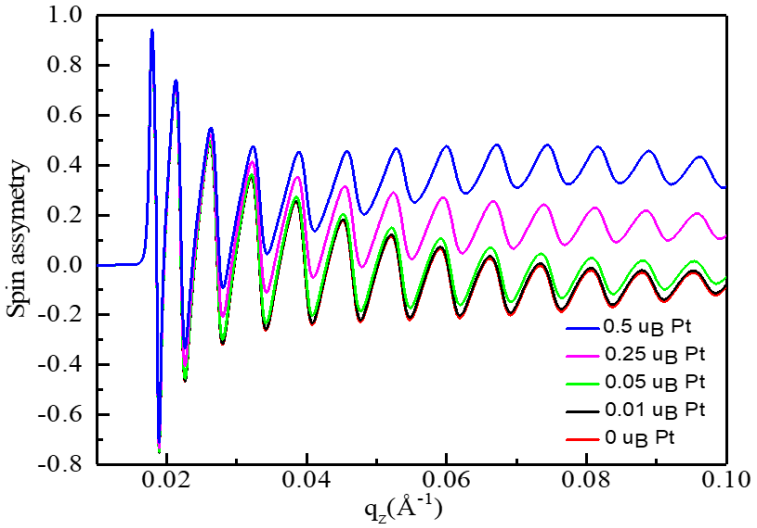

Figure 6.12: *Simulation of spin asymmetry in YIG (80 nm)/Pt (4nm) bilayer system using Gen-X. This shows that to detect any change of statistical significance in the spin asymmetry, moment induced in the Pt should be greater than 0.05 μ_B/atom. The minimum SA resolution for the instrument is 0.01 μ_B/atom.*

focussed on small wave vector range $q_z(\text{Å}^{-1})$. The experimental data were modelled and analysed by using Gen-X software.

Figure 6.11 shows the spin asymmetry data obtained at on-resonance (red curve) and off-resonance (black curve) condition. Oscillations are observed within small q_z range, 0.04 Å^{-1}. The difference in spin asymmetry, ΔSA(%), is shown in the inset of figure 6.11. We found no significant change in the spin asymmetry. Next, we carried out the simulation using Gen-X (figure 6.12) for this bilayer structure to estimate the amount of spin pumping required to get a noticeable change in spin asymmetry. This establishes an upper boundary for the change in magnetisation of 0.05 μ_B/atom, as seen in our simulation of the SA. The moment induced in the Pt layer is less than 0.05 μ_B/atom, so it was very hard to detect any change of statistical significance in the spin asymmetry between on and off-resonance condition.

6.6 Effect of C_{60} on Gilbert damping in YIG/C_{60} bilayer

In this section, our aim is to investigate the FMR properties of YIG/C_{60} hybrid structures. For this we deposited 20 nm thick C_{60} molecules by thermal sublimation on different thicknesses of YIG. We performed FMR measurements in each YIG sample before and after deposition of the C_{60} in order to study its effect on the linewidth and hence on the Gilbert damping parameter. Figure 6.13 shows an example of the absorption spectra with an in-plane magnetic field for 125 nm thick YIG film at f = 5-8 GHz with (a) and without C_{60} (c), the red solid lines are fittings to the data. It shows a single FMR peak in each case. The derivative of the Lorentzian absorption lines with their

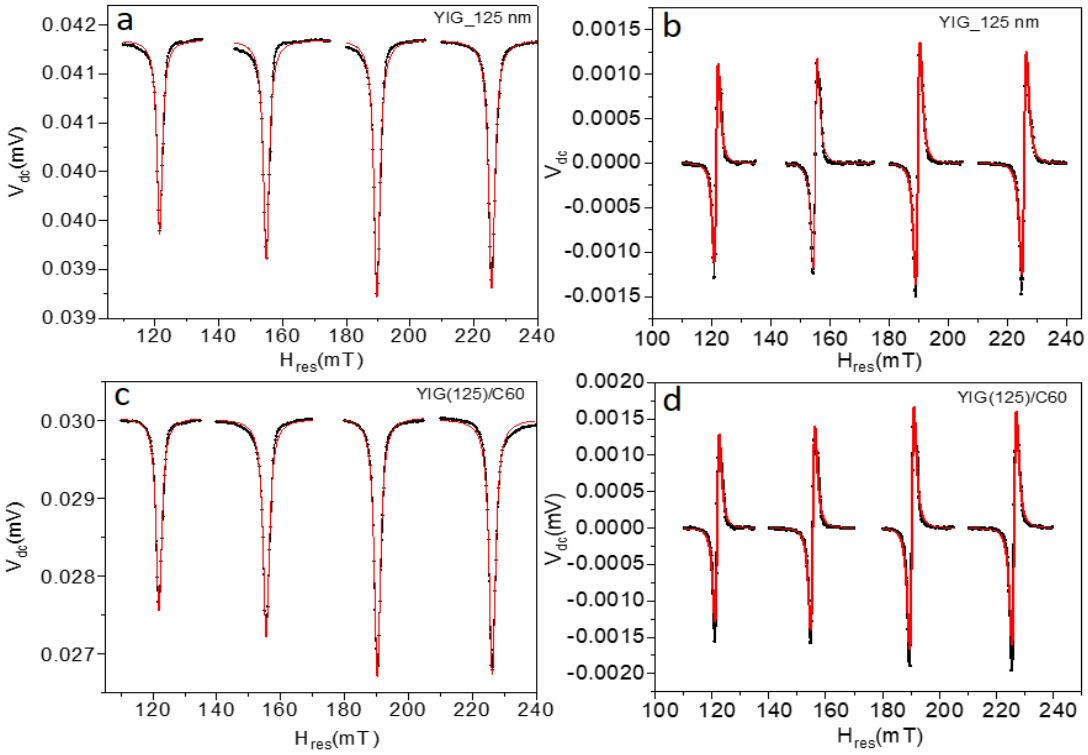

Figure 6.13: *Ferromagnetic resonance spectra with an in-plane magnetic field for 125 nm thick YIG film at f = 5-8 GHz with (a) and without C_{60} (c), the red solid lines are fits to the data. (b) and (d) shows the the derivative of the Lorentzian absorption lines with their fits (red solid lines) at f = 5-8 GHz with and without C_{60}, respectively.*

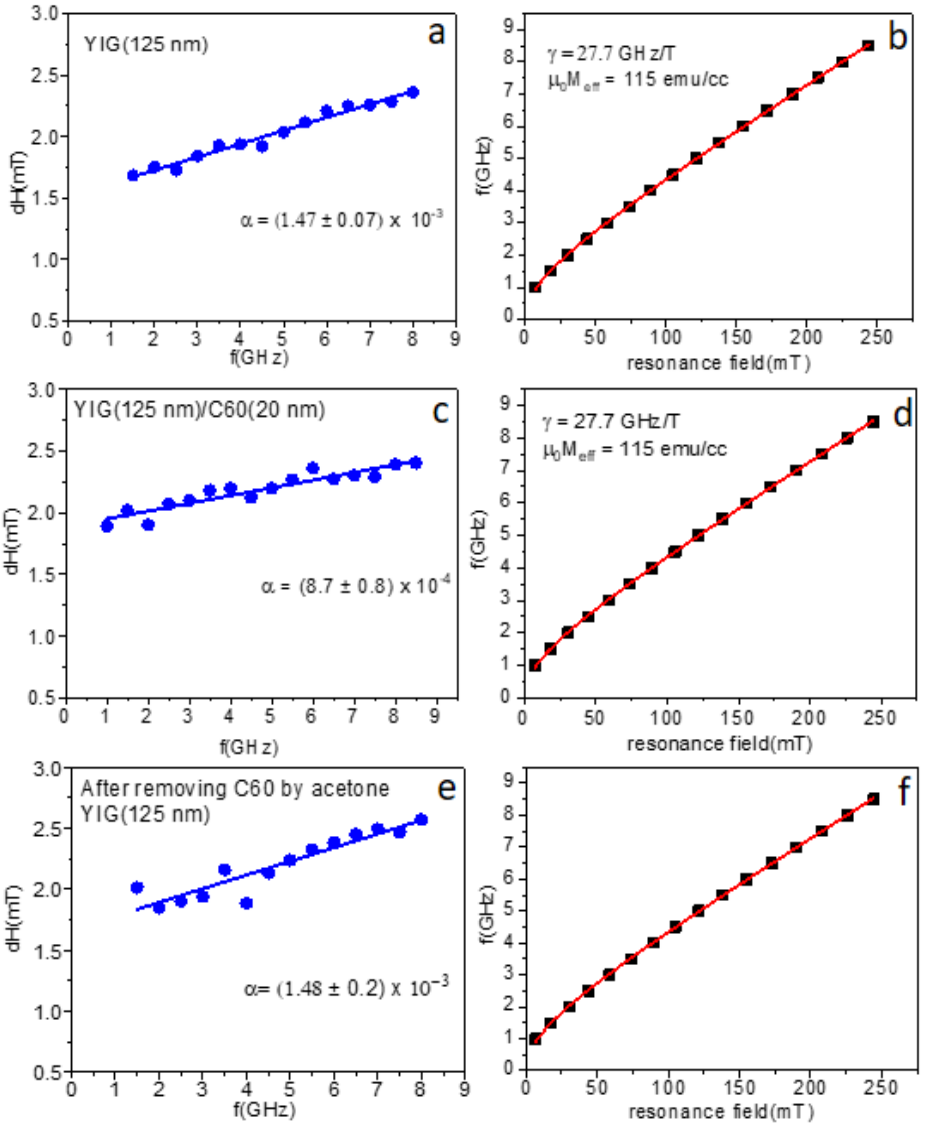

Figure 6.14: *FMR linewidth as a function of frequency for 125 nm thick YIG with (a) and without C_{60} (c), the blue solid lines are fit to the data. From the slope we extracted the damping parameter in each case, which shows that the damping decreases with C_{60}. (e) FMR linewidth as a function of frequency for the same sample measured after removing the C_{60} by using the acetone, and the damping parameter goes back to the previous value of bare YIG. In (b,d,f) we plotted the frequency dependence of resonance field with its Kittel fit (red line) which gives the gyromagnetic ratio 27.7 GHz/T. The effective magnetization does not change with C_{60}.*

fits (red solid lines) at f = 5-8 GHz with and without C_{60} are plotted in figure 6.13b and d, respectively. Figure 6.14 illustrates FMR measurements on 125 nm thick YIG with (a) and without C_{60} (b). From this one can observe that there is an appreciable amount of decrease in damping with C_{60} covered YIG: α (YIG) = (1.47 $\pm$ 0.07) x 10^{-3} and α (YIG/C_{60}) = (8.7 $\pm$ 0.8) x 10^{-4}. In order to double check the change in damping we repeated the measurement on the same sample after removing C_{60} using acetone, and we found that there is no change in α for bare YIG film, which is an evidence that the C_{60} growth process does not affect the YIG film (figure 6.14e). Also, the effective magnetization of YIG remains the same with and without C_{60}: $\mu_0 M_{eff}$ = 115 emu/cc, shown in figure 6.14b and d.

To summarise our FMR results we plotted the percentage change in damping ($d\alpha/\alpha_{yig}$) in YIG/C_{60} as a function of YIG thickness as shown in figure 6.15. For the lower thicknesses of YIG (below 80 nm), we found an increase in linewidth and damping in

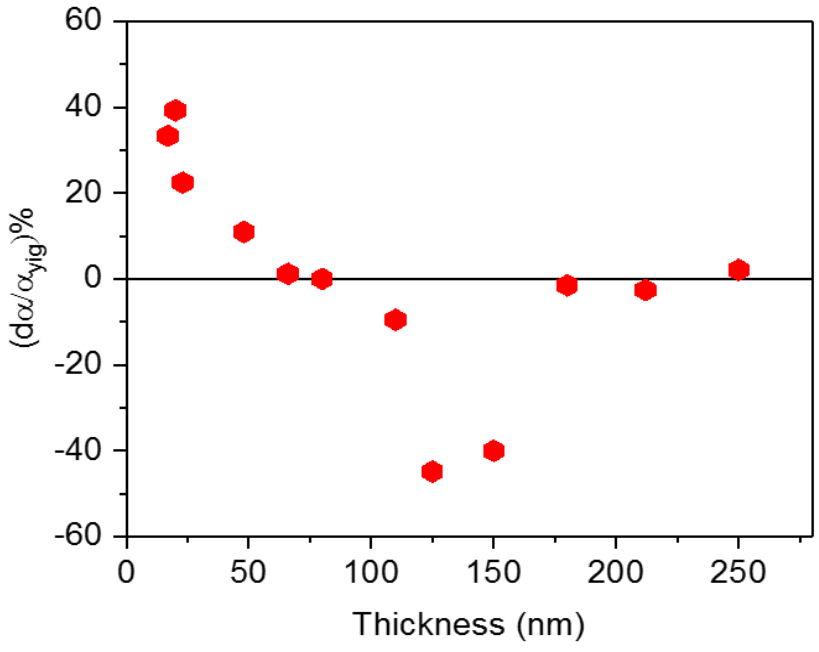

Figure 6.15: *Percentage change in damping as a function of YIG thickness in YIG/C_{60}(20 nm) bilayer structures. We observed an unexpected decrease in damping in the thickness range between 80 nm to 160 nm.*

YIG/C_{60} which gives an indication of spin pumping from YIG into C_{60} molecules. For very thick films, above 180 nm, we hardly observed any change in damping. This is because for very thick films the interface become quite rough, so probability of spin injection into the C_{60} almost disappears. But we found the result is interesting in the thickness range between 80 nm to 160 nm, where we noticed an unexpected decrease in damping, more pronounced in the case of a 125 nm thick film. This is something which may signify a phenomenon which is reverse of spin pumping effect.

In figure 6.16 we plotted separately the thickness dependence of Gilbert damping of bare YIG samples which were used for this YIG/C_{60} experiment. We observed that damping is not following a definite trend with thickness. This might be due to the presence of multiple peaks which we cannot distinguish in our Lorentzian absorption profile. In reference [62], more than one peak has also been reported for a 20 nm thick film as shown in figure 6.17a. Here they mentioned the additional peaks correspond to standing spin wave modes which are visible due to the extremely low damping in the layers. Also, all our samples were not grown in the same growth run, this may be

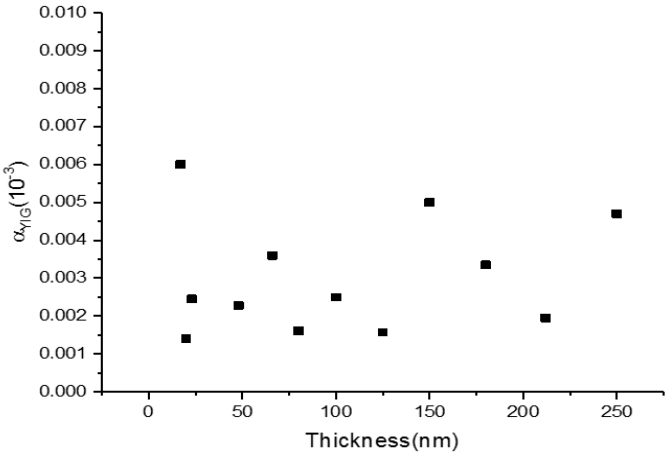

Figure 6.16: *Gilbert damping as a function of YIG thickness. We observed that damping is not following any definite trend with thickness. This might be due to the presence of mulitple peaks which we can not distinguish in our Lorentzian spectra. Also all these samples were not grown in the same growth run.*

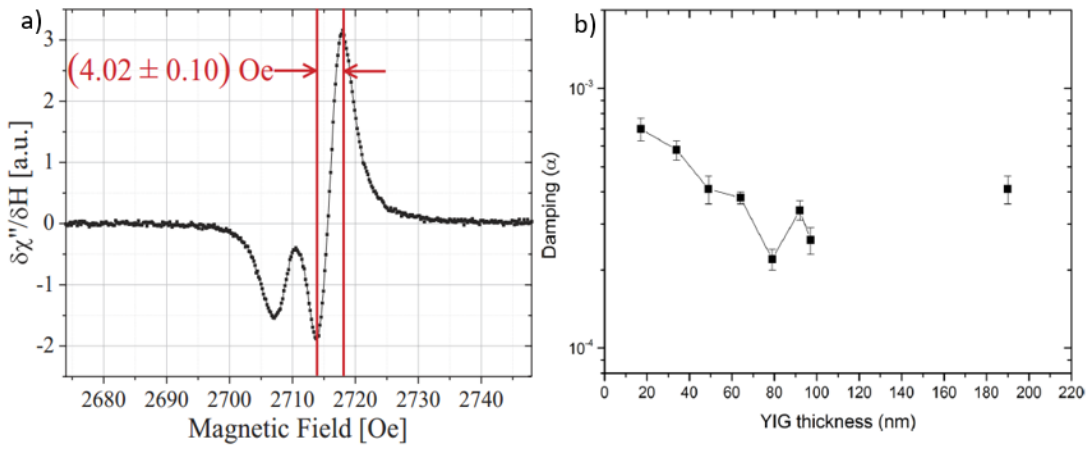

Figure 6.17: *(a) FMR data obtained at 9.6 GHz for a 20 nm thick YIG after annealing [62]. This work also shows the presence of double peak in the absorption spectra. The main resonance lines have a peak-to-peak linewidth of* 4.02 ± 0.10 *Oe. (b) Damping parameter of YIG films as a function of film thickness [156], from which one can see that there is a sudden increase in damping in very thick YIG films.*

another reason for the random variations of damping parameter. Figure 6.17b shows some similar behaviour for thicker films and it also reported higher damping suddenly around 190 nm thick YIG [156].

We are not able to draw conclusion about our results on the unexpected decrease in damping in YIG/C_{60} as we are lacking proper explanation. So we need more detail investigations of the dynamic properties of YIG/C_{60} hybrid structures to find out the physics behind the magnetization dynamics or the interfacial effect that leads to the reduction of damping parameter.

6.7 Conclusion

In this chapter, we performed a comprehensive study on the dynamic properties of YIG films on their own and with Pt overlayer. For our nm-thick YIG films, Gilbert damping has a thickness dependence. The value of the gyromagnetic ratio remains

nearly constant and is close to the theoretical value. The FMR profile has a narrow linewidth of several Oersteds. FMR measurements on our smooth films shows linear increase of linewidth with frequency, indicating the absence of two-magnon scattering. Samples made from the Target-A (2.6 $\pm$ 0.3 x 10^{-4} for 38 nm [174]) showed lower damping compared to the samples deposited from the Target-B (1.92 $\pm$ 0.1 x 10^{-3} for 38 nm). This indicates a possibility of having inhomogeneties which may result in non-uniformity in magnetization over a long range or may be due to some deficit in the right stoichiometry. This work also demonstrates the temperature dependence of Gilbert damping factor in nm-thick YIG film in the temperature range 20 K to 300 K which decays exponentially with increase in temperature. We observed a downturn in effective magnetization at low temperatures. A large value of spin mixing conductance, (1.6 $\pm$ 0.3) x 10^{19} m^{-2} for YIG/Pt sample is an indication of a good interface which is necessary for efficient spin transfer. In continuation of this work, we should investigate the temperature dependence of damping in YIG on YAG substrate for future studies.

From PNR-FMR results, we get an idea on the amount of moment required to detect significant spin pumping in terms of spin asymmetry in YIG/Pt bilayer structure. We carried out CI-FMR measurements in a series of YIG/HM samples with different YIG thickness between 14.8 nm and 80 nm to quantify the current-induce torque. Our conclusion is, the Oersted field dominates over STT in driving the magnetisation precession and should therefore be taken into account for CI-FMR studies in YIG/HM systems. In future, we need to figure out the ways to improve the YIG/metal interface so that we can realize spin-transfer torque in this system and hence STT devices using YIG. At last, we investigated the effect of C_{60} on the damping parameter in YIG/C_{60} hybrid structures which has not been studied before. For thin samples, we observed that the damping increases with C_{60}, which is an encouraging result. For certain range of thicknesses (thicker films), we noticed an unexpected decrease in the damping for C_{60} covered YIG samples. This is quite interesting but we are not yet able to predict the actual physics to explain the magnetization dynamics in this structure. For this we need further investigations which is currently in progress in our group.

CHAPTER 7

Conclusion

7.1 Summary

This research demonstrates the growth of high quality nanometre thick YIG films by on-axis RF magnetron sputtering, which are reproducible and consistently exhibit the required properties of YIG. The results of structural, magnetic and FMR measurements demonstrated a good matching with the ones grown by pulse laser deposition (PLD), on and off-axis sputtering. These nanometre thick YIG films can be used for a wider range of research which includes spin pumping, spin transfer torque, spin hall magnetoresistance (SHMR) and the magnonics community.

A comprehensive study of the crystallinity and morphology of the YIG films shows a (111) crystalline orientation with RMS surface roughness of about 1-3 Å. The lattice constant of the YIG is close to the bulk value (12.376 Å). In collaboration with the SuperSTEM Laboratory in Daresbury, we analysed the chemical nature of the YIG/GGG interface using atomic resolution STEM, indicating an interdiffusion at the YIG/GGG interface, with 4 - 6 nm Gd-doped region in which Y and Gd diffuse in pairs. A good fitting (GOF = 0.04) of x-ray reflectivity curve of annealed YIG sample is obtained by introducing a Gd-mixed YIG layer at the interface. The XRR data fitting returns the densities for the YIG and GGG which are within 1% of the bulk values. The formation of interdiffusion layer takes place during the high temperature annealing (850°C). The good agreement between the x-ray data fitting and STEM results allowed us to propose a two layer model to represent the YIG sample: a Gd-rich YIG layer with a highly disordered structure near the interface and the upper layer is almost a perfect YIG. This Gd-mixed YIG interlayer influences the magnetic properties and may also contribute to the FMR linewidth broadening in YIG, particularly at low temperatures.

The magnetic properties of YIG on (111) oriented GGG substrate are studied extensively using magnetometry and polarised neutron reflectivity. Due to the paramagnetism induced by the Gd^{3+} ions from the GGG and increased saturation field at room temperature, measurement of the magnetic moment of YIG at low temperatures is challenging. The YIG films have very low coercivity 0.30 ± 0.05 Oe and a saturation magnetisation 144 emu/cc at 295 K. Our result on the thickness dependence of the

saturation magnetic moment confirms the existence of 6 nm dead layer at the interface. The temperature dependent magnetisation data M(T) reveals the magnetisation suppression at low temperature, below $\sim$100 K. The temperature dependent PNR results of 80 nm and 10 nm thick YIG shows an excellent agreement with their M(T) results, obtained by magnetometry. For 10 nm YIG, the compensation temperature is 100 K (corresponds to 40% Gd-diffusion) where the magnetization reaches minimum. At low temperature, Gd spins dominate the magnetic behaviour with its ordering temperature around 65-85 K and will align antiparallel to the net magnetic moment of YIG. Hence, the role of Gd-diffused layer in the reduction of magnetisation in YIG films is clearly understood. The proposed two-layer model fits all the M(T) data consistently for different thicknesses of YIG with a 6 nm thick Gd-diffused YIG layer at the interface. In phenomena that requires thin YIG films, the magnetic behaviour of the Gd-layer, which will be paramagnetic at room temperature and gradually align antiparallel as the sample is cooled, will have to be considered. The M(T) data of YIG on YAG shows no downturn of magnetisation at low temperatures. This again supports the influence of Gd-diffusion from GGG on the magnetisation of YIG. The magnetic properties of YIG on YAG showed low saturation magnetisation (98 emu/cc for 40 nm YIG) and high coercivity (70 Oe). This is possibly due to the large lattice mismatch between YIG and YAG.

For our nm-thick YIG films, the FMR profile has a narrow linewidth with extremely small damping (eg. (2.6 $\pm$ 0.3) x 10^{-4} for 38 nm YIG). The value of the gyromagnetic ratio, 27.7 GHz/T is close to the theoretical value. The Gilbert damping parameter shows a thickness dependence, such that it is inversely proportional to the thickness of YIG. This work demonstrates the temperature dependence of Gilbert damping factor in YIG nano films in the temperature range 20 K to 300 K, decaying exponentially with increase in temperature. It could be possible that the Gd-layer and slow relaxation mechanisms of rare-earth impurities affecting the magnetization dynamics of pure YIG, which results in low temperature increase in the FMR linewidth. A large value of the spin mixing conductance 1.6 x 10^{19} m^{-2} is found in YIG/Pt sample, indicating

a good interface necessary for efficient spin injection in YIG-based heterostructures. With PNR-FMR experiments, we get an idea of the amount of moment required to detect significant spin pumping in terms of spin asymmetry in the YIG/Pt bilayer structures. The FMR results of YIG/C_{60} hybrid structures shows spin pumping but with rich underlying physics in the dissipation and uniformity of the FMR signal, which is an encouraging result for future study. Our collaborative work on the spin wave propagation in nm-thick YIG films [174] with the University of Regensburg made an important contribution to the YIG community. We are able to observe spin wave (SW) excitations at distances up to 150 μm away from the exciting CPW. The spin wave decay length is about 2.7 μm and 3.6 μm for the 38 nm and 49 nm thick YIG films, respectively. The CI-FMR measurements in collaboration with the University of Cambridge, shows that the Oersted field dominates over the spin transfer torque in driving the magnetization dynamics in YIG/metal bilayer structures [86]. Our research on YIG using the FMR technique covered a broad area which is important to study the spin pumping and STT effect in YIG/Pt and other YIG based multilayer structures.

In conclusion, this work demonstrates the growth and complete study of the properties of epitaxial nm-thick sputtered YIG. We have revealed the nature of this promising material to the spintronics community. This work discovered the interfacial diffusion and its effect on the magnetisation of thin YIG. The demand for thin YIG films is set to increase as the field of magnonics and insulator-based spintronics develops. In particular, the prospect of being able to use high-quality sputtered YIG, which is the industrial method for deposition makes YIG films an excellent choice for the spintronics community.

7.2 Future work

The research work covered in this thesis paves the way for the growth optimization and more advanced experiments with RF sputtered YIG films and YIG-based bilayer structures. This section is devoted to the possible future experiments using these films.

For future studies, it would be good to examine the stoichiometry of the annealed YIG of different thicknesses. This could be done by X-ray photoelectron spectroscopy (XPS). For chemical analysis of the top surface of YIG, we can use AFM [192]. The in-situ annealing can be done to improve the sample quality. The deposition can also be done with a high substrate temperature that may produce as-deposited epitaxial films. Piranha etching is the uncontrolled part of YIG surface processing. Alternative cleaning steps such as plasma oxidation and ion milling should be consider to get better interface quality. We identified a 4-6 nm interdiffusion region at the YIG/GGG interface. It can be possible to limit the diffusion by lowering the annealing temperature and increasing the annealing time to crystallise the structure. There is the possibility of further improving the quality of the films by optimising the annealing temperature or using annealed GGG for the growth or introducing a diffusion barrier between YIG and GGG. We must consider the deposition of YIG films by off-axis sputtering in varying substrates (GGG and YAG) in the future. We performed intensive research on the magnetic properties of YIG using magnetometry. In the future, microanalysis of magnetic structure using magnetic force microscopy (MFM) should be done to get detail information about the inhomogeneous distribution of magnetization of the sample, which may be related to the multiple peaks observed in FMR results.

Within the scope of this thesis, the first step towards the utilization of sputtered nm-thick YIG films in spin pumping and current induced FMR have been made. Following our results on the temperature dependence of the Gilbert damping, we should measure the temperature dependent FMR properties for YIG deposited on YAG. We are currently undertaking this work in collaboration with the University of Regensburg. A comparison of α(T) for YIG on GGG and YAG substrate will give us a better understanding of the physics and the parameters that are dominating at low temperatures. From this we can also develop an idea about the behaviour of the spin mixing conductance and the propagation/injection of spin currents as a function of temperature. We should consider surface cleaning of YIG by plasma etching before Pt deposition to improve the YIG-Pt interface. This will increase the spin pumping efficiency and pos-

sibility of realising the spin transfer torque in nanoscale YIG. The results obtained from YIG/C_{60} structures open a new area to work with molecules on YIG, which can lead to an exciting research area in the field of molecular spintronics. For better understanding of the effect of C_{60} on the damping parameter of YIG, we must perform the FMR measurements of YIG/C_{60} bilayers films by varying the thickness of the C_{60} layer. It will be also interesting to investigate the spin pumping effect in YIG/C_{60}/Pt trilayer structures by varying the thickness of C_{60}. This work is in progress in our group. Parallely, our YIG samples for spin injection experiments in YIG/PBTTT bilayers has also showed promising results, which give a further opportunity to try different materials on YIG for spin injection experiments. This work is now in progress in collaboration with the Optoelectronics group in University of Cambridge. Another aspect of future work could be the optical spin pumping in YIG/molecular structure. We should also think about the microfabrication of YIG as it already proved to be a potential material for insulator based spintronics devices.

REFERENCES

[1] N. Mott and B. N. F. Mott, "The electrical conductivity of transition metals," *Proceedings of the Royal Society of London. Series A, ...*, vol. 153, no. 880, pp. 699–717, 1936.

[2] N. Mott, F.R.S., and H. Wills, "The Resistance and Thermoelectric Properties of the Transition Metals," *Proceedings of the Royal Society of London A*, vol. 156, no. 188, pp. 368–382, 1936.

[3] M. N. Baibich, J. M. Broto, A. Fert, F. N. Van Dau, F. Petroff, P. Eitenne, G. Creuzet, A. Friederich, and J. Chazelas, "Giant magnetoresistance of (001)Fe/(001)Cr magnetic superlattices," *Physical Review Letters*, vol. 61, no. 21, pp. 2472–2475, 1988.

[4] G. Binasch, P. Grünberg, F. Saurenbach, and W. Zinn, "Enhanced magnetoresistance in layered magnetic structures with antiferromagnetic interlayer exchange," *Physical Review B*, vol. 39, no. 7, pp. 4828–4830, 1989.

[5] U. Hartmann, ed., *Magnetic Multilayers and Giant Magnetoresistance*, vol. 37. Springer-Verlag Berlin Heidelberg, 2000.

[6] H. S. E. Hirota and K. Inomata, eds., *Giant Magneto-Resistance Devices*, vol. 40. Springer-Verlag Berlin Heidelberg, 2002.

[7] J. Daughton, J. Brown, E. Chen, R. Beech, A. Pohm, and W. Kude, "Magnetic

field sensors using GMR multilayer," *Magnetics, IEEE Transactions on*, vol. 30, no. 6, pp. 4608–4610, 1994.

[8] G. A. Prinz, "Magnetoelectronics," *Science*, vol. 282, no. November, pp. 1660–1663, 1998.

[9] M. Julliere, "Tunneling between ferromagnetic films," *Physics Letters A*, vol. 54, no. 3, pp. 225–226, 1975.

[10] T. Miyazaki and N. Tezuka, "Giant magnetic tunneling effect in Fe/Al_2O_3/Fe junction," *Journal of Magnetism and Magnetic Materials*, vol. 139, no. 3, pp. 94–97, 1995.

[11] J. Slonczewski, "Current-driven excitation of magnetic multilayers," *Journal of Magnetism and Magnetic Materials*, vol. 159, no. 1-2, pp. L1–L7, 1996.

[12] L. Berger, "Emission of spin waves by a magnetic multilayer traversed by a current," *PhysRevB*, vol. 54, no. 13, pp. 9353–9358, 1996.

[13] J. M. Slaughter, R. W. Dave, M. Deherrera, M. Durlam, B. N. Engel, J. Janesky, N. D. Rizzo, and S. Tehrani, "Fundamentals of MRAM technology," *Journal of Superconductivity*, vol. 15, no. 1, pp. 19–25, 2002.

[14] T. M. Maffitt, J. K. DeBrosse, J. a. Gabric, E. T. Gow, M. C. Lamorey, J. S. Parenteau, D. R. Willmott, M. A. Wood, and W. J. Gallagher, "Design considerations for MRAM," *IBM Journal of Research and Development*, vol. 50, no. 1, pp. 25–39, 2006.

[15] J. Katine, F. Albert, R. Buhrman, E. Myers, and D. Ralph, "Current-Driven Magnetization Reversal and Spin-Wave Excitations in Co /Cu /Co Pillars," *Physical Review Letters*, vol. 84, no. 14, pp. 3149–3152, 2000.

[16] S. S. P. Parkin, M. Hayashi, and L. Thomas, "Magnetic Domain-Wall Racetrack Memory," *Science*, vol. 320, no. 5873, pp. 190–194, 2008.

[17] S. Datta and B. Das, "Electronic analog of the electro-optic modulator," *Applied Physics Letters*, vol. 56, no. 7, pp. 665–667, 1990.

[18] H. C. Koo, J. H. Kwon, J. Eom, J. Chang, S. H. Han, and M. Johnson, "Control of Spin Precession in a Spin-Injected Field Effect Transistor," *Science*, vol. 325, no. 5947, pp. 1515–1518, 2009.

[19] C. Betthausen, T. Dollinger, H. Saarikoski, V. Kolkovsky, G. Karczewski, T. Wojtowicz, K. Richter, and D. Weiss, "Spin-Transistor Action via Tunable Landau-Zener Transitions," *Science*, vol. 337, no. 6092, pp. 324–327, 2012.

[20] M. P. Kostylev, A. A. Serga, T. Schneider, B. Leven, and B. Hillebrands, "Spin-wave logical gates," *Applied Physics Letters*, vol. 87, no. 15, pp. 1–3, 2005.

[21] A. A. Serga, A. V. Chumak, and B. Hillebrands, "YIG magnonics," *J. Phys. D: Appl. Phys.*, vol. 43, no. 43, pp. 264002–264002, 2010.

[22] V. V. Kruglyak, S. O. Demokritov, and D. Grundler, "Magnonics," *Journal of Physics D: Applied Physics*, vol. 43, no. 26, p. 264001, 2010.

[23] T. Schneider, A. A. Serga, B. Leven, B. Hillebrands, R. L. Stamps, and M. P. Kostylev, "Realization of spin-wave logic gates," *Applied Physics Letters*, vol. 92, no. 2, 2008.

[24] A. Khitun, M. Bao, and K. L. Wang, "Magnonic logic circuits," *Journal of Physics D: Applied Physics*, vol. 43, no. 26, p. 264005, 2010.

[25] B. Lenk, H. Ulrichs, F. Garbs, and M. Münzenberg, "The building blocks of magnonics," *Physics Reports*, vol. 507, no. 4-5, pp. 107–136, 2011.

[26] T. Brächer, F. Heussner, P. Pirro, T. Fischer, M. Geilen, B. Heinz, B. Lägel, A. A. Serga, and B. Hillebrands, "Time- and power-dependent operation of a parametric spin-wave amplifier," *Applied Physics Letters*, vol. 105, no. 23, 2014.

[27] V. E. Demidov, S. Urazhdin, and S. O. Demokritov, "Direct observation and mapping of spin waves emitted by spin-torque nano-oscillators.," *Nature materials*, vol. 9, no. 12, pp. 984–988, 2010.

[28] M. Madami, S. Bonetti, G. Consolo, S. Tacchi, G. Carlotti, G. Gubbiotti, F. B. Mancoff, M. a. Yar, and J. Åkerman, "Direct observation of a propagating spin wave induced by spin-transfer torque," *Nature Nanotechnology*, vol. 6, no. 10, pp. 635–638, 2011.

[29] V. E. Demidov, S. Urazhdin, H. Ulrichs, V. Tiberkevich, A. Slavin, D. Baither, G. Schmitz, and S. O. Demokritov, "Magnetic nano-oscillator driven by pure spin current," *Nature Materials*, vol. 11, no. 12, pp. 1028–1031, 2012.

[30] Y. Tserkovnyak, A. Brataas, and G. E. W. Bauer, "Enhanced gilbert damping in thin ferromagnetic films.," *Physical review letters*, vol. 88, no. 11, p. 117601, 2002.

[31] M. V. Costache, M. Sladkov, S. M. Watts, C. H. Van Der Wal, and B. J. Van Wees, "Electrical detection of spin pumping due to the precessing magnetization of a single ferromagnet," *Physical Review Letters*, vol. 97, no. 21, pp. 1–4, 2006.

[32] J. E. Hirsch, "Spin Hall Effect," *Physical Review Letters*, vol. 83, no. 9, pp. 1834–1837, 1999.

[33] E. Saitoh, M. Ueda, H. Miyajima, and G. Tatara, "Conversion of spin current into charge current at room temperature: Inverse spin-Hall effect," *Applied Physics Letters*, vol. 88, no. 18, pp. 1–4, 2006.

[34] S. Zhang, "Spin Hall effect in the presence of spin diffusion," *Physical Review Letters*, vol. 85, no. 2, pp. 393–396, 2000.

[35] Y. Kajiwara, K. Harii, S. Takahashi, J. Ohe, K. Uchida, M. Mizuguchi, H. Umezawa, H. Kawai, K. Ando, K. Takanashi, S. Maekawa, and E. Saitoh,

"Transmission of electrical signals by spin-wave interconversion in a magnetic insulator.," *Nature*, vol. 464, no. 7286, pp. 262–266, 2010.

[36] J. C. Slonczewski, "Initiation of spin-transfer torque by thermal transport from magnons," *Physical Review B - Condensed Matter and Materials Physics*, vol. 82, no. 5, pp. 1–11, 2010.

[37] K. Uchida, S. Takahashi, K. Harii, J. Ieda, W. Koshibae, K. Ando, S. Maekawa, and E. Saitoh, "Observation of the spin Seebeck effect.," *Nature*, vol. 455, no. 7214, pp. 778–81, 2008.

[38] K. Uchida, J. Xiao, H. Adachi, J. Ohe, S. Takahashi, J. Ieda, T. Ota, Y. Kajiwara, H. Umezawa, H. Kawai, G. E. W. Bauer, S. Maekawa, and E. Saitoh, "Spin Seebeck insulator," *Nature Materials*, vol. 9, no. 11, pp. 894–897, 2010.

[39] G. A. M. Alexander G. Gurevich, *Magnetization Oscillations and Waves*. CRC Press, 1996.

[40] K. ichi Uchida, T. Kikkawa, A. Miura, J. Shiomi, and E. Saitoh, "Quantitative temperature dependence of longitudinal spin seebeck effect at high temperatures," *Physical Review X*, vol. 4, no. 4, pp. 1–9, 2014.

[41] X. Jia, K. Liu, K. Xia, and G. E. W. Bauer, "Spin transfer torque on magnetic insulators," *EPL (Europhysics Letters)*, vol. 96, no. 1, p. 4, 2011.

[42] C. Du, H. Wang, F. Yang, and P. C. Hammel, "Systematic variation of spin-orbit coupling with d -orbital filling: Large inverse spin Hall effect in 3d transition metals," *Physical Review B - Condensed Matter and Materials Physics*, vol. 90, no. 14, pp. 1–5, 2014.

[43] H. Jin, S. R. Boona, Z. Yang, R. C. Myers, and J. P. Heremans, "Effect of the magnon dispersion on the longitudinal spin Seebeck effect in yttrium iron garnets," *Physical Review B - Condensed Matter and Materials Physics*, vol. 92, no. 5, 2015.

[44] D. J. Sanders and D. Walton, "Effect of magnon-phonon thermal relaxation on heat transport by magnons," *Physical Review B*, vol. 15, no. 3, pp. 1489–1494, 1977.

[45] T. Kikkawa, K. I. Uchida, S. Daimon, Z. Qiu, Y. Shiomi, and E. Saitoh, "Critical suppression of spin Seebeck effect by magnetic fields," *Physical Review B - Condensed Matter and Materials Physics*, vol. 92, no. 6, pp. 1–9, 2015.

[46] H. L. Wang, C. H. Du, Y. Pu, R. Adur, P. C. Hammel, and F. Y. Yang, "Scaling of spin hall angle in 3d, 4d, and 5d metals from $Y_3Fe_5O_{12}$ /metal spin pumping," *Physical Review Letters*, vol. 112, no. 19, pp. 1–5, 2014.

[47] C. H. Du, H. L. Wang, Y. Pu, T. L. Meyer, P. M. Woodward, F. Y. Yang, and P. C. Hammel, "Probing the spin pumping mechanism: Exchange coupling with exponential decay in $Y_3Fe_5O_{12}$/barrier/Pt heterostructures," *Physical Review Letters*, vol. 111, no. 24, pp. 1–5, 2013.

[48] C. Du, H. Wang, F. Yang, and P. C. Hammel, "Enhancement of Pure Spin Currents in Spin Pumping $Y_3Fe_5O_{12}$/Cu/Metal Trilayers through Spin Conductance Matching," *Physical Review Applied*, vol. 1, no. 4, 2014.

[49] H. Wang, C. Du, P. Chris Hammel, and F. Yang, "Spin current and inverse spin Hall effect in ferromagnetic metals probed by $Y_3Fe_5O_{12}$-based spin pumping," *Applied Physics Letters*, vol. 104, no. 20, 2014.

[50] T. Chiba, G. E. W. Bauer, and S. Takahashi, "Spin torque transistor revisited," *Applied Physics Letters*, vol. 102, no. 19, 2013.

[51] M. B. Jungfleisch, V. Lauer, R. Neb, a. V. Chumak, and B. Hillebrands, "Improvement of the yttrium iron garnet/platinum interface for spin pumping-based applications," *Applied Physics Letters*, vol. 103, no. 2, pp. 2011–2015, 2013.

[52] Y. Sun, H. Chang, M. Kabatek, Y. Y. Song, Z. Wang, M. Jantz, W. Schneider, M. Wu, E. Montoya, B. Kardasz, B. Heinrich, S. G. E. Te Velthuis, H. Schulthe-

iss, and A. Hoffmann, "Damping in yttrium iron garnet nanoscale films capped by platinum," *Physical Review Letters*, vol. 111, no. 10, 2013.

[53] S. M. Rezende, R. L. Rodríguez-Suárez, M. M. Soares, L. H. Vilela-Leão, D. Ley Domínguez, and a. Azevedo, "Enhanced spin pumping damping in Yttrium Iron Garnet/Pt bilayers," *Applied Physics Letters*, vol. 102, no. 1, pp. 1–4, 2013.

[54] Y. Sun, Y. Y. Song, H. Chang, M. Kabatek, M. Jantz, W. Schneider, M. Wu, H. Schultheiss, and A. Hoffmann, "Growth and ferromagnetic resonance properties of nanometer-thick yttrium iron garnet films," *Applied Physics Letters*, vol. 101, no. 15, p. 082405, 2012.

[55] N. Kumar, D. S. Misra, N. Venkataramani, S. Prasad, and R. Krishnan, "Magnetic properties of pulsed laser ablated YIG thin films on different substrates," in *Journal of Magnetism and Magnetic Materials*, vol. 272-276, 2004.

[56] E. Popova, N. Keller, F. Gendron, M. Guyot, M. C. Brianso, Y. Dumond, and M. Tessier, "Structure and magnetic properties of yttrium-iron-garnet thin films prepared by laser deposition," *Journal of Applied Physics*, vol. 90, no. 3, pp. 1422–1428, 2001.

[57] N. S. Sokolov, V. V. Fedorov, A. M. Korovin, S. M. Suturin, D. A. Baranov, S. V. Gastev, B. B. Krichevtsov, K. Y. Maksimova, A. I. Grunin, V. E. Bursian, L. V. Lutsev, and M. Tabuchi, "Thin yttrium iron garnet films grown by pulsed laser deposition: Crystal structure, static, and dynamic magnetic properties," *Journal of Applied Physics*, vol. 119, no. 2, 2016.

[58] M. Haidar, M. Ranjbar, M. Balinsky, R. K. Dumas, S. Khartsev, and J. Åkerman, "Thickness- and temperature-dependent magnetodynamic properties of yttrium iron garnet thin films," *Journal of Applied Physics*, vol. 117, no. 17, 2015.

[59] O. D'Allivy Kelly, A. Anane, R. Bernard, J. Ben Youssef, C. Hahn, A. H. Molpeceres, C. Carrétéro, E. Jacquet, C. Deranlot, P. Bortolotti, R. Lebourgeois, J. C. Mage, G. De Loubens, O. Klein, V. Cros, and A. Fert, "Inverse spin Hall effect in nanometer-thick yttrium iron garnet/Pt system," *Applied Physics Letters*, vol. 103, no. 8, 2013.

[60] L. V. Lutsev, A. M. Korovin, V. E. Bursian, S. V. Gastev, V. V. Fedorov, S. M. Suturin, and N. S. Sokolov, "Low-relaxation spin waves in laser-molecular-beam epitaxy grown nanosized yttrium iron garnet films," *Applied Physics Letters*, vol. 108, no. 18, 2016.

[61] A. Kaveev, V. Bursian, S. Gastev, B. Krichevtsov, S. Suturin, M. Volkov, and N. Sokolov, "Laser MBE-grown yttrium iron garnet films on GaN: Characterization of the crystal structure and magnetic properties," *Materials Research Express*, vol. 3, no. 7, 2016.

[62] C. Hauser, T. Richter, N. Homonnay, C. Eisenschmidt, H. Deniz, D. Hesse, S. Ebbinghaus, G. Schmidt, and N. Weinberg, "Yttrium Iron Garnet Thin Films with Very Low Damping Obtained by Recrystallization of Amorphous Material," *arXiv:1502.06724v2*, no. February, pp. 1–13, 2016.

[63] T. Liu, H. Chang, V. Vlaminck, Y. Sun, M. Kabatek, A. Hoffmann, L. Deng, and M. Wu, "Ferromagnetic resonance of sputtered yttrium iron garnet nanometer films," *Journal of Applied Physics*, vol. 115, no. 17, pp. 2014–2017, 2014.

[64] J. Lustikova, Y. Shiomi, Z. Qiu, T. Kikkawa, R. Iguchi, K. Uchida, and E. Saitoh, "Spin current generation from sputtered $Y_3Fe_5O_{12}$ films," *Journal of Applied Physics*, vol. 116, no. 15, p. 153902, 2014.

[65] H. L. Wang, C. H. Du, Y. Pu, R. Adur, P. C. Hammel, and F. Y. Yang, "Large spin pumping from epitaxial $Y_3Fe_5O_{12}$ thin films to Pt and W layers," *Physical Review B - Condensed Matter and Materials Physics*, vol. 88, no. 10, pp. 1–5, 2013.

[66] Y.-M. Kang, S.-H. Wee, S.-I. Baik, S.-G. Min, S.-C. Yu, S.-H. Moon, Y.-W. Kim, and S.-I. Yoo, "Magnetic properties of YIG ($Y_3Fe_5O_{12}$) thin films prepared by the post annealing of amorphous films deposited by rf-magnetron sputtering," *Journal of Applied Physics*, vol. 97, no. 10, p. 10A319, 2005.

[67] F. Bertaut and F. Forrat, "The structure of the ferrimagnetic rare earth ferrites," *Compt. rend. (1956), 242, 382-4.*, 1956.

[68] S. Geller and M. A. Gilleo, "Structure and ferrimagnetism of yttrium and rare-earth-iron garnets," *Acta Crystallographica*, vol. 10, no. 3, p. 239, 1957.

[69] P. E. Wigen, R. D. McMichael, and C. Jayaprakash, "Route to chaos in the magnetic garnets," *Journal of Magnetism and Magnetic Materials*, vol. 84, no. 3, pp. 237–246, 1990.

[70] D. D. Stancil and A. Prabhakar, *Spin Waves*. Springer US, 2009.

[71] M. Sparks, *Ferromagnetic-relaxation theory*. McGraw-Hill advanced physics monograph series, McGraw-Hill, 1964.

[72] M. Jungfleisch, "Wellenvektoraufgeloste Brillouin-Lichtstreuspektroskopie an nichtlinearen Spinwellen," 2009.

[73] M. A. Gilleo and S. Geller, "Magnetic and Crystallographic Properties of Substituted Yttrium-Iron Garnet, 3Y2O3.xM2O3.(5-x)Fe2O3," *Physical Review*, vol. 110, no. 1, pp. 73–78, 1958.

[74] Z. Celinski and B. Heinrich, "Ferromagnetic resonance linewidth of Fe ultrathin films grown on a bcc Cu substrate," *Journal of Applied Physics*, vol. 70, no. 10, pp. 5935–5937, 1991.

[75] L. Landau and E. Lifshits, "On the Theory of the Dispersion of Magnetic Permeability in Ferromagnetic Bodies," *Phys. Zeitsch. der Sow.*, vol. 169, no. 14, pp. 14–22, 1935.

[76] T. Gilbert, "Classics in Magnetics A Phenomenological Theory of Damping in Ferromagnetic Materials," *IEEE Transactions on Magnetics*, vol. 40, no. 6, pp. 3443–3449, 2004.

[77] H. Suhl, "Theory of the magnetic damping constant," *IEEE Transactions on Magnetics*, vol. 34, no. 4 PART 1, pp. 1834–1838, 1998.

[78] M. Jungfleisch, *Spin pumping and inverse spin Hall effect in yttrium iron garnet/ platinum heterostructures*. PhD thesis, Fachbereich Physik, TU Kaiserslautern, 2013.

[79] Griffiths J. H. E., "Anomalous High-frequency Resistance of Ferromagnetic Metals," *Nature*, vol. 158, no. 4019, pp. 670–671, 1946.

[80] C. Kittel, "Interpretation of anomalous larmor frequencies in ferromagnetic resonance experiment [5]," *Physical Review*, vol. 71, no. 4, pp. 270–271, 1947.

[81] C. Kittel, "On the theory of ferromagnetic resonance absorption," *Physical Review*, vol. 73, no. 2, pp. 155–161, 1948.

[82] E. B. Myers, D. C. Ralph, J. A. Katine, R. N. Louie, and R. A. Buhrman, "Current-Induced Switching of Domains in Magnetic Multilayer Devices," *Science*, vol. 285, no. 5429, pp. 867–870, 1999.

[83] A. Brataas, Y. V. Nazarov, and G. E. W. Bauer, "Finite-Element Theory of Transport in Ferromagnet-Normal Metal Systems," *Physical Review Letters*, vol. 84, no. 11, pp. 2481–2484, 2000.

[84] G. Woltersdorf, *SPIN-PUMPING AND TWO-MAGNON SCATTERING IN MAGNETIC MULTILAYERS*. PhD thesis, 2004.

[85] M. B. Jungfleisch, A. V. Chumak, A. Kehlberger, V. Lauer, D. H. Kim, M. C. Onbasli, C. A. Ross, M. Klaui, and B. Hillebrands, "Thickness and power dependence of the spin-pumping effect in $Y_3Fe_5O_{12}$ /Pt heterostructures measured

by the inverse spin Hall effect," *Physical Review B - Condensed Matter and Materials Physics*, vol. 91, no. 13, 2015.

[86] Z. Fang, A. Mitra, A. L. Westerman, M. Ali, C. Ciccarelli, O. Cespedes, B. J. Hickey, and A. J. Ferguson, "Thickness dependence study of current-driven ferromagnetic resonance in Y3Fe5O12/heavy metal bilayers," *Applied Physics Letters*, vol. 110, no. 9, 2017.

[87] M. Schreier, T. Chiba, A. Niedermayr, J. Lotze, H. Huebl, S. Geprägs, S. Takahashi, G. E. W. Bauer, R. Gross, and S. T. B. Goennenwein, "Current-induced spin torque resonance of a magnetic insulator," *Physical Review B - Condensed Matter and Materials Physics*, vol. 92, no. 14, pp. 1–6, 2015.

[88] M. B. Jungfleisch, W. Zhang, J. Sklenar, J. Ding, W. Jiang, H. Chang, F. Y. Fradin, J. E. Pearson, J. B. Ketterson, V. Novosad, M. Wu, and A. Hoffmann, "Large Spin-Wave Bullet in a Ferrimagnetic Insulator Driven by the Spin Hall Effect," *Physical Review Letters*, vol. 116, no. 5, pp. 1–6, 2016.

[89] J. D. Jackson, *Classical Electrodynamics, 3rd Edition*. John Wiley & Sons, 1998.

[90] E. S. Katsuaki Sato, ed., *Spintronics for Next Generation Innovative Devices*. JohnWiley & Sons Ltd, 2015.

[91] I. Žutić, J. Fabian, and S. D. Sarma, "Spintronics: Fundamentals and applications," *Reviews of Modern Physics*, vol. 76, no. 2, pp. 323–410, 2004.

[92] S. P. Helmut Kronmuller, ed., *Handbook of Magnetism and Advanced Magnetic Materials*. Wiley-Blackwell, 2007.

[93] M. I. D'yakonov and V. I. Perel', "Possibility of orienting electron spins with current," *JETP Letters*, vol. 13, no. 11, pp. 467–469, 1971.

[94] M. I. Dyakonov and V. I. Perel, "Current-induced spin orientation of electrons in semiconductors," *Physics Letters A*, vol. 35, no. 6, pp. 459–460, 1971.

[95] N. P. Stern, S. Ghosh, G. Xiang, M. Zhu, N. Samarth, and D. D. Awschalom, "Current-induced polarization and the spin hall effect at room temperature," *Physical Review Letters*, vol. 97, no. 12, pp. 1–4, 2006.

[96] Y. K. Kato, R. C. Myers, A. C. Gossard, and D. D. Awschalom, "Observation of the Spin Hall Effect in Semiconductors," *Science (New York, N.Y.)*, vol. 306, no. 2004, pp. 1910–1913, 2004.

[97] J. Wunderlich, B. Kaestner, J. Sinova, and T. Jungwirth, "Experimental observation of the spin-hall effect in a two-dimensional spin-orbit coupled semiconductor system," *Physical Review Letters*, vol. 94, no. 4, pp. 1–4, 2005.

[98] V. Sih, R. C. Myers, Y. K. Kato, W. H. Lau, A. C. Gossard, and D. D. Awschalom, "Spatial imaging of the spin Hall effect and current-induced polarization in two-dimensional electron gases," *Nature Physics*, vol. 1, no. 1, pp. 31–35, 2005.

[99] S. O. Valenzuela and M. Tinkham, "Direct electronic measurement of the spin Hall effect.," *Nature*, vol. 442, no. 7099, pp. 176–9, 2006.

[100] T. Kimura, Y. Otani, T. Sato, S. Takahashi, and S. Maekawa, "Room-temperature reversible spin hall effect," *Physical Review Letters*, vol. 98, no. 15, pp. 1–4, 2007.

[101] T. Tanaka, H. Kontani, M. Naito, T. Naito, D. S. Hirashima, K. Yamada, and J. Inoue, "Intrinsic spin Hall effect and orbital Hall effect in 4d and 5d transition metals," *Physical Review B - Condensed Matter and Materials Physics*, vol. 77, no. 16, pp. 1–16, 2008.

[102] R. Winkler, *Spin Orbit Coupling Effects in Two-Dimensional Electron and Hole Systems*. Springer Berlin Heidelberg, 2003.

[103] G. Vignale, "Ten years of spin hall effect," *Journal of Superconductivity and Novel Magnetism*, vol. 23, no. 1, pp. 3–10, 2010.

[104] L. Berger, "Side-jump mechanism for the hall effect of ferromagnets," *Physical Review B*, vol. 2, no. 11, pp. 4559–4566, 1970.

[105] R. Karplus and J. M. Luttinger, "Hall effect in ferromagnetics," *Physical Review*, vol. 95, no. 5, pp. 1154–1160, 1954.

[106] N. Mott and H. Massey, *The theory of atomic collisions*. International series of monographs on physics. International series of monographs on physics (Oxford, England), Oxford; 3rd edition (November 1965), 1965.

[107] L.D.Landau and E.M.Lifshitz, *Landau-Lifschitz_Quantum-Mechanics_Non-relativistic_theory*, vol. 3. WILEY-VCH, 1964.

[108] S. K. Lyo and T. Holstein, "Side-Jump Mechanism for Ferromagnetic Hall Effect," *Physical Review Letters*, vol. 29, no. 7, pp. 423–425, 1972.

[109] S. Takahashi and S. Maekawa, "Spin current, spin accumulation and spin Hall effect," *Science and Technology of Advanced Materials*, vol. 9, no. 1, p. 014105, 2008.

[110] K. Ando, S. Takahashi, J. Ieda, Y. Kajiwara, H. Nakayama, T. Yoshino, K. Harii, Y. Fujikawa, M. Matsuo, S. Maekawa, and E. Saitoh, "Inverse spin-Hall effect induced by spin pumping in metallic system," *Journal of Applied Physics*, vol. 109, no. 10, 2011.

[111] H. A. Kiyotaka Wasa, Makoto Kitabatake, *Thin Film Materials Technology: Sputtering of Compound Materials*. William Andrew, 2004, 2004.

[112] C. J. D. Windover E. Barnat J. Y. Kim M. Nielsen T.M. Lu A. Kumar H. Bakhru and S. L. Lee, "Thin film density determination by multiple radiation energy

dispersive x-ray reflectivity," *JCPDS-International Centre for Diffraction Data 2000, Advances in X-ray Analysis*, vol. 42, pp. 590–600, 2000.

[113] J. Als-Nielsen and D. McMorrow, *Elements of Modern X-Ray Physics*. John Wiley and Sons Ltd, 2001.

[114] H. Kiessig, "Untersuchungen zur totalreflexion von röntgenstrahlen," *Annalen der Physik*, vol. 402, no. 6, pp. 715–768, 1931.

[115] U. Pietsch, V. Holy, and T. Baumbach, *High-resolution X-Ray scattering: from thin films to lateral nanostructures*. Advanced Texts in Physics, Springer New York, 2004.

[116] N. Porter, *Magnetoresistance in n-type Silicon*. PhD thesis, School of Physics and Astronomy, University of Leeds, September 2010.

[117] G. Aviv, "SQUIDs-Superconducting Quantum Interference Devices," *Experimental physics course*, 2008.

[118] C. Graham, "High-sensitivity magnetization measurements," *Journal of Materials Sciences and Technology*, vol. 16, no. 02, pp. 97–101, 2000.

[119] J. Clarke and A. I. Braginski, *The SQUID Handbook*. Wiley VCH, 2005.

[120] G. Binnig and C. F. Quate, "Atomic Force Microscope," *Physical Review Letters*, vol. 56, no. 9, pp. 930–933, 1986.

[121] Á. S. Paulo and R. García, "Unifying theory of tapping-mode atomic-force microscopy," *Physical Review B*, vol. 66, no. 4, p. 041406, 2002.

[122] R. Garcia and R. Perez, "Dynamic atomic force microscopy methods," *Surface Science Reports*, vol. 47, pp. 197–301, 2002.

[123] N. Jalili and K. Laxminarayana, "A review of atomic force microscopy imaging systems: Application to molecular metrology and biological sciences," *Mechatronics*, vol. 14, no. 8, pp. 907–945, 2004.

[124] B. H. J. Anthony C. Bland, ed., *Ultrathin Magnetic Structures III*. Springer Berlin Heidelberg, 2005.

[125] S. V.F., *NEUTRON OPTICS. An Introduction to the Theory of Neutron Optical Phenomena and their Applications.* Oxford University Press, 1989.

[126] b. H. Fritzsche, Z. Yamani, R. Cowley, R. Ward, and H. Fritzsche, "Polarised neutron reflectometry as a unique tool in magnetization reversal studies of thin films and multilayers.," *La Physique Au Canada*, 2006.

[127] J. F. Ankner and G. P. Felcher, "Polarized-neutron reflectometry," *Journal of Magnetism and Magnetic Materials, Volume 200, Issue 1-3, p. 741-754*, 1999.

[128] C. Kinane, *The interplay of magnetism and structure in patterned multilayer thin films*. PhD thesis, School of Physics and Astronomy, University of Leeds, 2008.

[129] V. G. Gavriljuk, A. Dobrinsky, B. D. Shanina, and S. P. Kolesnik, "A study of the magnetic resonance in a single-crystal Ni 50.47 Mn 28.17 Ga 21.36 alloy," *Journal of Physics: Condensed Matter*, vol. 18, no. 32, pp. 7613–7627, 2006.

[130] M. Díaz de Sihues, C. Durante-Rincón, and J. Fermin, "A ferromagnetic resonance study of NiFe alloy thin films," *Journal of Magnetism and Magnetic Materials*, vol. 316, no. 2, pp. e462–e465, 2007.

[131] Z. Zhang, L. Zhou, P. E. Wigen, and K. Ounadjela, "Angular dependence of ferromagnetic resonance in exchange-coupled Co/Ru/Co trilayer structures," *Physical Review B*, vol. 50, no. 9, pp. 6094–6112, 1994.

[132] B. Heinrich, Y. Tserkovnyak, G. Woltersdorf, A. Brataas, R. Urban, and G. E. W. Bauer, "Dynamic exchange coupling in magnetic bilayers.," *Physical Review Letters*, vol. 90, no. May, p. 187601, 2003.

[133] V. P. Nascimento, E. Baggio Saitovitch, F. Pelegrini, L. C. Figueiredo, A. Biondo, and E. C. Passamani, "Ferromagnetic resonance study of the exchange bias field in NiFeFeMnNiFe trilayers," *Journal of Applied Physics*, vol. 99, no. 8, pp. 8–10, 2006.

[134] M. Oogane, T. Wakitani, S. Yakata, R. Yilgin, Y. Ando, A. Sakuma, and T. Miyazaki, "Magnetic damping in ferromagnetic thin films," *Japanese Journal of Applied Physics, Part 1: Regular Papers and Short Notes and Review Papers*, vol. 45, no. 5 A, pp. 3889–3891, 2006.

[135] R. Urban, G. Woltersdorf, and B. Heinrich, "Gilbert damping in single and multilayer ultrathin films: role of interfaces in nonlocal spin dynamics.," *Physical review letters*, vol. 87, no. 21, p. 217204, 2001.

[136] R. Komiya, T. Kato, N. Nishizawa, S. Tsunashima, and S. Iwata, "Compositional dependence of g -factor and damping constant of (Gd 100- x RE x)FeCo alloy films (RE = Yb, Tm, Er)," *Journal of Physics: Conference Series*, vol. 200, no. 4, p. 042010, 2010.

[137] National Instruments, "Introduction to Network Analyzer Measurements," *National Instruments RF Academy*, pp. 1–44, 2012.

[138] D. P. B. Gareth R. Eaton, Sandra S. Eaton and R. T. Weber, *Quantitative EPR*. Springer-Verlag Wien, 2010.

[139] J. P. Castera, "State of the art in design and technology of MSW devices (invited)," *Journal of Applied Physics*, vol. 55, no. 6, pp. 2506–2511, 1984.

[140] A. A. S. A. V. Chumak, V. I. Vasyuchka and B. Hillebrands, "Magnon spintronics," *nature physics*, vol. 11, no. June, 2015.

[141] M. Collet, M. Evelt, V. E. Demidov, J. L. Prieto, M. Muñoz, and J. B. Youssef, "Nano-patterned magnonic crystals based on ultrathin YIG films," *arXiv:1705.02267*, pp. 1–13, 2017.

[142] A. V. Chumak, A. a. Serga, and B. Hillebrands, "Magnon transistor for all-magnon data processing," *Nature Communications*, vol. 5, no. May 2013, p. 4700, 2014.

[143] T. Kikkawa, K. Uchida, Y. Shiomi, Z. Qiu, D. Hou, D. Tian, H. Nakayama, X. F. Jin, and E. Saitoh, "Longitudinal spin seebeck effect free from the proximity nernst effect," *Physical Review Letters*, vol. 110, no. 6, pp. 1–5, 2013.

[144] C. W. Sandweg, Y. Kajiwara, K. Ando, E. Saitoh, and B. Hillebrands, "Enhancement of the spin pumping efficiency by spin wave mode selection," *Applied Physics Letters*, vol. 97, no. 25, pp. 2012–2015, 2010.

[145] J. Xiao, G. E. W. Bauer, K. C. Uchida, E. Saitoh, and S. Maekawa, "Theory of magnon-driven spin Seebeck effect," *Physical Review B - Condensed Matter and Materials Physics*, vol. 81, no. 21, pp. 1–8, 2010.

[146] E. Padron-Hernandez, A. Azevedo, and S. M. Rezende, "Amplification of spin waves by thermal spin-transfer torque," *Physical Review Letters*, vol. 107, no. 19, pp. 1–5, 2011.

[147] H. Kurebayashi, O. Dzyapko, V. E. Demidov, D. Fang, A. J. Ferguson, and S. O. Demokritov, "Controlled enhancement of spin-current emission by three-magnon splitting.," *Nature materials*, vol. 10, no. 9, pp. 660–4, 2011.

[148] S. A. Manuilov, R. Fors, S. I. Khartsev, and A. M. Grishin, "Submicron $Y_3Fe_5O_{12}$ film magnetostatic wave band pass filters," *Journal of Applied Physics*, vol. 105, no. 3, 2009.

[149] J. C. Gallagher, A. S. Yang, J. T. Brangham, B. D. Esser, S. P. White, M. R. Page, K. Y. Meng, S. Yu, R. Adur, W. Ruane, S. R. Dunsiger, D. W. McComb, F. Yang, and P. C. Hammel, "Exceptionally high magnetization of stoichiometric $Y_3Fe_5O_{12}$ epitaxial films grown on $Gd3Ga_5O_{12}$," *Applied Physics Letters*, vol. 109, no. 7, 2016.

[150] M. Paul, "Piranha clean procedure," pp. 1–3, 2010.

[151] P. Hartel, H. Rose, and C. Dinges, "Conditions and reasons for incoherent imaging in STEM," *Ultramicriscopy*, vol. 63, no. 96, pp. 93–114, 1996.

[152] V. V. Pan'Kov and L. A. Bashkirov, "Cationic interdiffusion in some garnets," *Journal of Solid State Chemistry*, vol. 60, no. 1, pp. 123–127, 1985.

[153] D. J. Cherniak, "Rare earth element and gallium diffusion in yttrium aluminum garnet," *Physics and Chemistry of Minerals*, vol. 26, no. 2, pp. 156–163, 1998.

[154] C. Pascual-Izarra, M. A. Reis, and N. P. Barradas, "Simultaneous PIXE and RBS data analysis using Bayesian inference with the DataFurnace code," *Nuclear Instruments and Methods in Physics Research, Section B: Beam Interactions with Materials and Atoms*, vol. 249, no. 1-2 SPEC. ISS., pp. 780–783, 2006.

[155] C. Du, H. Wang, P. C. Hammel, and F. Yang, "$Y_3Fe_5O_{12}$ spin pumping for quantitative understanding of pure spin transport and spin Hall effect in a broad range of materials (invited)," *Journal of Applied Physics*, vol. 117, no. 17, 2015.

[156] M. C. Onbasli, A. Kehlberger, D. H. Kim, G. Jakob, M. Kläui, A. V. Chumak, B. Hillebrands, and C. A. Ross, "Pulsed laser deposition of epitaxial yttrium iron garnet films with low Gilbert damping and bulk-like magnetization," *APL Materials*, vol. 2, no. 10, 2014.

[157] M. Aldosary, J. Li, C. Tang, Y. Xu, J.-g. Zheng, and N. Krassimir, "Platinum / Yttrium Iron Garnet Inverted Structures for Spin Current Transport," *Applied Physics Letters*, vol. 108, no. 242401, pp. 1–5, 2016.

[158] T. Yamagishi, J. Awaka, Y. Kawashima, M. Uemura, S. Ebisu, S. Chikazawa, and S. Nagata, "Ferrimagnetic order in the mixed garnet (Y_{1-X} Gd_X)," *Philosophical Magazine*, vol. 6435, no. July, 2005.

[159] L. Benjamin and K. J. Button, *Microwave ferrites and ferrimagnetics*. McGraw-Hill Book Company, 1962.

[160] C. Kittel, *Introduction to solid state physics*, vol. 8. Wiley New York, 1996.

[161] K. P. Belov, E. V. Talalaeva, and G. A. Yarkho, "Magnetic Properties of Rare-earth Iron Garnets in the Curie-point Region," *Soviet Journal of Experimental and Theoretical Physics*, vol. 25, no. 6, p. 989, 1967.

[162] S. Geprägs, A. Kehlberger, T. Schulz, C. Mix, F. Della Coletta, S. Meyer, A. Kamra, M. Althammer, G. Jakob, H. Huebl, R. Gross, S. T. B. Goennenwein, and M. Kläui, "Origin of the spin Seebeck effect probed by temperature dependent measurements in$Gd_3Fe_5O_{12}$," *arXiv:1405.4971*, pp. 1–6, 2014.

[163] G. F. Dionne, *Magnetic Oxides*. Springer US, 2009.

[164] R. Pauthenet, "Spontaneous magnetization of some garnet ferrites and the aluminum substituted garnet ferrites," *Journal of Applied Physics*, vol. 29, no. 3, pp. 253–255, 1958.

[165] D. Rodić, Z. Tomkowicz, L. Novaković, A. Szytula, and M. L. Napijalo, "The initial magnetic susceptibilities of $Gd_3Fe_5O_{12}$ and $Tb_3Fe_5O_{12}$ in the compensation point region," *Solid State Communications*, vol. 73, no. 3, pp. 243–246, 1990.

[166] G. Vértesy and I. Tomáš, "Survey of the dependence on temperature of the coercivity of garnet films," *Journal of Applied Physics*, vol. 77, no. 12, pp. 6426–6431, 1995.

[167] B. Keszei, "Modifying the temperature dependence of magnetic garnet film coercivity by etching," *Journal of Applied Physics*, vol. 86, no. 11, 1999.

[168] M. Björck and G. Andersson, "GenX: An extensible X-ray reflectivity refinement program utilizing differential evolution," *Journal of Applied Crystallography*, vol. 40, no. 6, pp. 1174–1178, 2007.

[169] M. R. Fitzsimmons and C. F. Majkzak, *Application of polarized neutron reflectometry to studies of artificially structured magnetic materials*. Springer US, 2005.

[170] B. Knorr and W. Tolksdorf, "Lattice parameters and misfits of gallium garnets and iron garnet epitaxial layers at temperatures between 294 and 1300 k," *Materials Research Bulletin*, vol. 19, pp. 1507–1513, 1984.

[171] E. Schlömann, J. J. Green, and U. Milano, "Recent developments in ferromagnetic resonance at high power levels," *Journal of Applied Physics*, vol. 386, no. 5, 1960.

[172] M. Zwierzycki, Y. Tserkovnyak, P. J. Kelly, A. Brataas, and G. E. W. Bauer, "First-principles study of magnetization relaxation enhancement and spin transfer in thin magnetic films," *Physical Review B - Condensed Matter and Materials Physics*, vol. 71, no. 6, pp. 1–11, 2005.

[173] D. Huertas-Hernando, F. Guinea, and A. Brataas, "Spin-orbit coupling in curved graphene, fullerenes, nanotubes, and nanotube caps," *Physical Review B - Condensed Matter and Materials Physics*, vol. 74, no. 15, 2006.

[174] A. Talalaevskij, M. Decker, J. Stigloher, A. Mitra, H. S. Körner, O. Cespedes, C. H. Back, and B. J. Hickey, "Magnetic properties of spin waves in thin yttrium iron garnet films," *Physical Review B*, vol. 95, no. 6, p. 064409, 2017.

[175] R. Arias and D. Mills, "Extrinsic contributions to the ferromagnetic resonance response of ultrathin films," *Physical Review B*, vol. 60, no. 10, pp. 7395–7409, 1999.

[176] S. M. R. Douglas L. Mills, *Spin Dynamics in Confined Magnetic Structures II*. Springer, Berlin, Heidelberg, 2003.

[177] T. Jungwirth, J. Wunderlich, and K. Olejnik, "Spin Hall effect devices," *Nature Materials*, vol. 11, no. May, pp. 382–390, 2012.

[178] C. L. Jermain, H. Paik, S. V. Aradhya, R. A. Buhrman, D. G. Schlom, and D. C. Ralph, "Low-damping sub-10-nm thin films of lutetium iron garnet grown by molecular-beam epitaxy," *Applied Physics Letters*, vol. 109, no. 19, 2016.

[179] C. Kittel, "Microwave resonance in rare earth iron garnets," *Journal of Applied Physics*, vol. 11, no. 5, pp. 10–13, 1960.

[180] P. E. Seiden, "Ferrimagnetic resonance relaxation in rare-earth iron garnets," *Journal of Applied Physics*, vol. 35, no. 3, p. 891, 1964.

[181] G. P. Rodrigue, H. Meyer, and R. V. Jones, "Resonance measurements in magnetic garnets," *Journal of Applied Physics*, no. 5, 1960.

[182] E. G. Spencer, R. C. Lecraw, and R. C. Linares, "Low-temperature ferromagnetic relaxation in yttrium iron garnet," *Physical Review*, vol. 123, no. 6, pp. 1937–1938, 1961.

[183] R. C. L. E. G. Spencer and A. M. Clogston, "Low-temperature line-width maximum in yttrium iron garnet," *Phys. Rev. Lett.*, vol. 3, no. 1, pp. 10–13, 1959.

[184] J. F. Dillon and J. W. Nielsen, "Effects of rare earth impurities on ferrimagnetic resonance in yttrium iron garnet," *Physical Review Letters*, vol. 3, no. 1, pp. 30–31, 1959.

[185] C. L. Jermain, S. V. Aradhya, J. T. Brangham, M. R. Page, N. D. Reynolds, P. C. Hammel, R. A. Buhrman, F. Y. Yang, and D. C. Ralph, "Increased low-temperature damping in yttrium iron garnet thin films," *Phys. Rev. B 95, 174411*, vol. 174411, pp. 1–5, 2017.

[186] M. Weiler, M. Althammer, M. Schreier, J. Lotze, M. Pernpeintner, S. Meyer, H. Huebl, R. Gross, A. Kamra, J. Xiao, Y. T. Chen, H. Jiao, G. E. W. Bauer, and S. T. B. Goennenwein, "Experimental test of the spin mixing interface conductivity concept," *Physical Review Letters*, vol. 111, no. 17, 2013.

[187] T. D. Skinner, M. Wang, a. T. Hindmarch, a. W. Rushforth, a. C. Irvine, D. Heiss, H. Kurebayashi, and a. J. Ferguson, "Spin-orbit torque opposing the Oersted torque in ultrathin Co/Pt bilayers," *Applied Physics Letters*, vol. 104, no. 6, p. 062401, 2014.

[188] W. Zhang, W. Han, X. Jiang, S.-H. Yang, and S. S. P. Parkin, "Role of transparency of platinum-ferromagnet interfaces in determining the intrinsic magnitude of the spin Hall effect," *Nature Physics*, vol. 11, no. 6, pp. 496–502, 2015.

[189] S. Langenfeld, V. Tshitoyan, Z. Fang, A. Wells, T. A. Moore, and A. J. Ferguson, "Exchange magnon induced resistance asymmetry in permalloy spin-Hall oscillators," *Applied Physics Letters*, vol. 108, no. 19, 2016.

[190] L. Liu, T. Moriyama, D. C. Ralph, and R. A. Buhrman, "Spin-torque ferromagnetic resonance induced by the spin Hall effect," *Physical Review Letters*, vol. 106, no. 3, pp. 1–4, 2011.

[191] L. Liu, C.-F. Pai, Y. Li, H. W. Tseng, D. C. Ralph, and R. A. Buhrman, "Spin-Torque Switching with the Giant Spin Hall Effect of Tantalum," *Science*, vol. 336, no. 6081, pp. 555–558, 2012.

[192] Y. Sugimoto, P. Pou, M. Abe, P. Jelinek, R. Pérez, S. Morita, and O. Custance, "Chemical identification of individual surface atoms by atomic force microscopy.," *Nature*, vol. 446, no. 7131, p. 64, 2007.